



POLITECNICO DI TORINO  
Repository ISTITUZIONALE

Computational Thermal Fluid Dynamic Analysis of Cooling Systems for Fusion Reactor Components

*Original*

Computational Thermal Fluid Dynamic Analysis of Cooling Systems for Fusion Reactor Components / Domalapally, PHANI KUMAR. - (2013).

*Availability:*

This version is available at: 11583/2514474 since:

*Publisher:*

Politecnico di Torino

*Published*

DOI:10.6092/polito/porto/2514474

*Terms of use:*

Altro tipo di accesso

This article is made available under terms and conditions as specified in the corresponding bibliographic description in the repository

*Publisher copyright*

(Article begins on next page)

**POLITECNICO DI TORINO**

**Energy Department**

**Computational Thermal Fluid Dynamic Analysis  
of Cooling Systems for Fusion Reactor  
Components**

**Phani Kumar Domalapally**

**Supervisors:**

**Roberto Zanino**

**Fabio Subba**

**Laura Savoldi**

**This thesis is submitted for the partial fulfillment of requirements for the  
Ph.D in Nuclear Engineering**

**May 2013**

# Abstract

In a fusion reactor during plasma operation, the heat loads on plasma facing components can be as high as  $5 \text{ MW/m}^2$  [1], which should be removed by a proper mechanism to prevent the damage of reactor components. In order to handle such high heat fluxes a suitable heat sink with proper thermal hydraulics is required. In the recent past several heat sinks have been proposed; among which the Hypervapotron heat sink, operating in the highly subcooled boiling regime, is considered as one of the potential candidates. In order to accurately predict the performance of the system, a thermal hydraulic analysis is required.

This thesis employs a Computational Fluid Dynamic (CFD) approach to do the thermal hydraulic analysis of the subcooled flow boiling inside the Hypervapotron channel. For this purpose four boiling models are tested using two commercial CFD codes. The four boiling models tested are Rensselaer Polytechnic Institute (RPI) boiling model [2] available in ANSYS-FLUENT 13, Bergles-Rohsenow (BR) model [3] implemented as an external User Defined Function (UDF) in the FLUENT code, the Rohsenow boiling model [4] extended with the capability of transition to film boiling for high heat fluxes available in STAR-CCM+ 7.02, and finally Transition boiling model [4] available in STAR-CCM+ 7.02. These models are used to test the thermal performance of Hypervapotron using the experimental data (showing the variation of temperature with heat flux) obtained from the experiments conducted at Efremov Institute Russia and Joint European Torus United Kingdom.

Simulations were conducted using the above mentioned boiling models, the obtained results were compared against the experimental data and also different boiling models are compared with each other whenever possible to test their applicability. From the simulations conducted on the Hypervapotron geometries it is found that the Transition boiling model can capture the thermal performance (in terms of tracing the experimental data) better than any other model both quantitatively and qualitatively, covering the different boiling regimes shown by the experiments ( that is no boiling, nucleate boiling and hard boiling regimes), than the other models.

# Acknowledgement

First and foremost I would like to thank my principal advisor Prof. Roberto Zanino, for giving me an opportunity to work with him, and for his guidance throughout my PhD. I would like to thank Dr. Laura Savoldi for helping me to start my research and giving valuable advices whenever needed. I would like to especially thank Dr. Fabio Subba for giving his valuable guidance and advices since 2011, and clearing my doubts with much patience all these years both academically and personally.

I would like to thank my colleagues for their support during my work and especially Roberto Bonifetto for his help in both academic and administrative work, keeping always a welcoming smile on his face, Antonio Buffo and Enrico Rizzo for helping me to understand the commercial Computational tools. I would like to thank all the university academic and administrative staff for their support and the Janitors for keeping my work place clean.

I would like to thank Dr. D. L. Youchison for discussing several topics during my PhD with our group, Dr. E. Baglietto for advice on the STAR-CCM+ boiling models and Dr. D. Marchisio for providing access to the computational facilities (during 2011). I would also like to thank STAR-CCM+ support in Turin for clearing my queries without delay when ever asked.

Last but not least I would like to thank my family for their support, ever since I was born for which I am indebted to them forever.

# Nomenclature

$A_w$	Interfacial area density at the wall surface
$c$	Speed of light
$C_{pl}$	Specific heat of liquid
$C_{qw}$	Constant dependent on the liquid/surface combination
$C_{ew}$	Heat flux fraction used to create vapor bubbles
$C_{HTC \times Area}$	HTC between a bubble and the surrounding liquid times the contact area per unit volume
$C_l$	Lift coefficient
$D_b$	Bubble diameter.
$E$	Total energy
$\bar{F}_q$	Body force
$\bar{F}_{lift,q}$	Lift force
$\bar{F}_{vm,q}$	Virtual mass force
$f$	Bubble departure frequency
$\bar{g}$	Gravitational vector
$h_0$	Total enthalpy
$h_{pq}$	Interphase enthalpy exchange
$h_{ls}$	Liquid side interfacial heat transfer coefficient
$h_{lat}$	Latent heat
$k_l$	Thermal conductivity of liquid

$k$	Turbulent kinetic energy
$L$	Latent heat per unit mass,
$\Delta m$	Change of total mass
$\dot{m}_{pq}$	Mass transfer from phase $p$ to phase $q$
$n$	Nucleation site density
$n_p$	Prandtl number exponent
$Nu$	Nusselt number
$p$	Static pressure
$Pr$	Prandtl number
$\vec{q}$	Heat flux
$q_w''$	Wall heat flux
$q_L''$	Heat flux due to liquid convection
$q_Q''$	Heat flux due to quenching
$q_E''$	Heat flux due to evaporation
$q_{FC}$	Forced convection heat flux
$q_{FDB}$	Fully developed boiling heat flux
$q_0$	Flux at the onset of nucleate boiling
$Q_{pq}$	Intensity of heat exchange
$R_{pq}$	Interfacial drag force
$Re$	Reynolds number
$Re_b$	Bubble Reynolds number and

$Re_v$	Bubble shear Reynolds number
$S_\alpha$	Mass source term
$S_h$	Source of enthalpy
$S_{ct}$	Schmidt number
$T$	Temperature
$\vec{V}$	Velocity vector
$\bar{V}_{pq}$	Interphase velocity
$\bar{\tau}$	Stress tensor
$\alpha$	Volume fraction
$\varepsilon$	Turbulent dissipation rate
$\eta$	Thermal diffusivity
$\kappa$	Von Karman constant
$\mu_l$	Liquid viscosity
$\rho$	Density
$\sigma$	Surface tension

### **Subscripts**

$l$	Liquid state
$p$	Vapor phase
$q$	Liquid phase
$Sat$	Saturation
$v$	Vapor state
$w$	Wall

# List of figures

Fig 1: ITER [9]	3
Fig 2: Divertor [9]	3
Fig 3: Neutral beam injection system	4
Fig 4: Boiling curve	5
Fig 5: The cross (a) and lateral (b) sections of Hypervapotron	7
Fig 6: Cattadori's visualization of the Hypervapotron effect occurrence [20]	8
Fig 7: Boiling curve for fully developed flow boiling in Hypervapotron [22]	9
Fig 8: Different Hypervapotron configurations considered by Z.wang etal [35]	11
Fig 9: 3D sketch of the experimental test section geometry (the dark region on the top marks the heated surface, all dimensions are in mm).	13
Fig 10: (a) Flat channel cross section (b) Cross (top) and longitudinal (bottom) sections of the Hypervapotron channel.	14
Fig 11: The temperature evolution as a function of time at different thermocouple locations (inlet velocity 1 m/s and heat flux 2 MW/m <sup>2</sup> )	15
Fig 12: The temperature evolution as a function of time at different thermocouple locations , showing the instability in the surface temperature due to occurrence of CHF (inlet velocity 1 m/s and heat flux 4 MW/m <sup>2</sup> )	16
Fig 13: Flat channel data, for (a) 1m/s inlet velocity, (b) 2 m/s inlet velocity, (c) 4 m/s inlet velocity at different heat fluxes.	18
Fig 14: Temperature evolution as a function of time at different thermocouple locations (inlet velocity 1 m/s and heat flux 3 MW/m <sup>2</sup> )	19
Fig 15: Temperature evolution as a function of time at different thermocouple locations , showing the instability in the surface temperature due to occurrence of CHF (inlet velocity 1 m/s and heat flux 6 MW/m <sup>2</sup> )	19
Fig 16: Hypervapotron data for (a) 1m/s inlet velocity (b) 2 m/s inlet velocity	20
Fig 17: Hypervapotron cross-sections for a) Boxscrapper, b) Div 4×3, c) Div6×6 and d) MkI respectively [19].	22
Fig 18 : Cross-sections of tested elements: a) standard JET Hypervapotron, b) new Boxscrapper Hypervapotron und c) Boxscrapper element prototype [41].	22
Fig 19: Boxscrapper data showing the variation of the surface temperature with respect to the applied surface power density [19, 41]	23
Fig 20: The modified MKI Hypervapotron with central slot [39]	24
Fig 21: Variation of temperature with power density for the modified MkI Hypervapotron [39]	24
Fig 22: Hypervapotron designs tested by Falter et al [39]	25



Fig 23: Div 6×6mm experimental data used in this thesis [19]	25
Fig 24: Div 4×3mm experimental used in this thesis [19]	26
Fig 25: Experimental data of Div 4×3 mm showing different boiling regimes (the transition between different regimes is located for the case $V_{in} = 7.89$ m/s).	27
Fig 26: Forced convection (dashed), onset of nucleate boiling (dotted), fully developed boiling (dash-dotted) heat fluxes, together with the BR merging (solid). Data are for the operating pressure of 20 bar.	36
Fig 27: Heat flux vs Excess temperature [4]	39
Fig 28: Mesh used for most of the computations for Flat channel	44
Fig 29: Comparison of temperatures simulated (solid), experimental (symbol) for input power of 1 MW/m <sup>2</sup> and inlet velocity 2m/s.	46
Fig 30: Comparison of temperatures computed with the BR model (solid line) with the experimental data (symbols) for different heat fluxes.(a) $V_{in} = 1$ m/s, (b) $V_{in} = 2$ m/s and (c) $V_{in} = 4$ m/s.	50
Fig 31: Comparison of temperatures computed with Rohsenow model (solid line) with the experimental data (symbols) for different heat fluxes and (a) $V_{in} = 1$ m/s, (b) $V_{in} = 2$ m/s and (c) $V_{in} = 4$ m/s.	54
Fig 32: Flat channel-Rohsenow model. Vapor volume fraction, averaged over the fluid-solid interface on the heated side of the flat-channel, as a function of the input heat flux. $V_{in} = 1, 2,$ and 4 m/s are considered.	54
Fig 33: Flat channel, surface temperature profile (CuCrZr face), for inlet velocity of 2 m/s and heat flux of 4 MW/m <sup>2</sup> .	55
Fig 34: vapor volume fraction profile at mid section, for inlet velocity of 2 m/s and heat flux of 4 MW/m <sup>2</sup> (a) over entire channel (b) Zoom at near the heated section	55
Fig 35: Flat channel. Comparison of temperatures computed with the Rohsenow (solid line) and the BR (dash-dot line) models, with the thermocouple data (symbols) for inlet velocity = 2 m/s and different heat flux levels.	56
Fig 36: Mesh used for most of the computations for Hypervapotron.	57
Fig 37: Variation of surface temperature with decreasing grid size at different thermocouple locations for 1 m/s inlet velocity and heat flux 4 MW/m <sup>2</sup> .	59
Fig 38: Variation of solver elapsed time with grid size for 1 m/s inlet velocity and heat flux 4 MW/m <sup>2</sup> .	60
Fig 39: Hypervapotron cross-sections for a) Boxscraper, b) Div 4×3, c) Div6×6 and d) MkI respectively [19].	61
Fig 40: Div 4×3- Mesh used for most of the computations, non uniform unstructured polyhedral mesh.	62
Fig 41 : Grid convergence analysis on Div 4×3 for inlet velocity 11 m/s case (a) variation of temperature at thermocouple location with number of cells in fluid, (b) variation of relative error with number of cells in fluid	63
Fig 42: Div 4×3mm experimental data used in the CFD validation exercise [19]	67
Fig 43: Div 4×3, comparison of temperatures computed with Rohsenow model (solid line) with the experimental data (symbols) for different heat fluxes and inlet	68

velocities.	
Fig 44: Div 4×3 (a) Temperature contours in the solid and fluid domain, (b) vapor volume fraction, for inlet velocity of 11 m/s and surface heat flux of 18.7 MW/m <sup>2</sup> .	69
Fig 45: Boxscraper experimental data [19]	70
Fig 46: Boxscraper- Mesh used for most of the computations, non uniform unstructured polyhedral mesh.	70
Fig 47: Boxscraper, comparison of temperatures computed with Rohsenow model (solid line) with the experimental data (symbols) for different heat fluxes and inlet velocities.	71
Fig 48: Div 6×6 experimental data [19]	72
Fig 49: Div 6×6 - mesh used for most of the computations, non uniform unstructured polyhedral mesh.	72
Fig 50: Div 6×6, comparison of temperatures computed with Rohsenow model (solid line) with the experimental data (symbols) for different heat fluxes and inlet velocities.	73
Fig 51: Mk1 experimental data [19]	74
Fig 52: Mk1- mesh used for most of the computations, non uniform unstructured polyhedral mesh.	74
Fig 53: Mk1, comparison of temperatures computed with Rohsenow model (solid line) with the experimental data (symbols) for different heat fluxes and inlet velocities.	75
Fig 54: Div 4×3, comparison of temperatures computed with Transition boiling model (solid line) with the experimental data (symbols) for different heat fluxes and inlet velocities.	78
Fig 55: Div 4×3 (a) Temperature contours in the solid and fluid domain, (b) vapor volume fraction, for inlet velocity of 11 m/s and surface heat flux of 18.7 MW/m <sup>2</sup> .	79
Fig 56: Boxscraper, comparison of temperatures computed with Transition boiling model (solid line) with the experimental data (symbols) for different heat fluxes and inlet velocities.	80
Fig 57: Div 6×6, comparison of temperatures computed with Transition boiling model (solid line) with the experimental data (symbols) for different heat fluxes and inlet velocities.	80
Fig 58: Mk1, comparison of temperatures computed with Transition boiling model (solid line) with the experimental data (symbols) for different heat fluxes and inlet velocities.	81
Fig 59: Comparison of results between Rohsenow model, Transition boiling model with experimental data, for Div 4×3 geometry and 11 m/s inlet velocity.	82
Fig 60: Performance of boiling model against Div 4×3mm HV [19]	82

# List of Tables

Table 1: Summary of Hypervapotron validation cases [19]	21
Table 2: Settings used to perform simulations using RPI model	45
Table 3. Parameters in the FLUENT / BR model.	48
Table 4: Settings used to perform simulations using BR model	48
Table 5: Free parameters in the Rohsenow model, as determined by Youchison [29].	51
Table 6: Settings used to perform simulations using Rohsenow model	52
Table 7: Settings used to perform simulations using Rohsenow model for Hypervapotron geometry	58
Table 8: Summary of Hypervapotron validation cases [19]	61
Table 9. Free parameters used in the Rohsenow model for Hypervapotron.	65
Table 10: Settings used to perform simulations using Rohsenow model for Hypervapotron geometry	66
Table 11: Free parameters used in the Transition boiling model for Hypervapotron.	76
Table 12: Settings used to perform simulations using Transition boiling model	76

# Contents

<b>Abstract</b>	<b>I</b>
<b>Acknowledgements</b>	<b>II</b>
<b>Nomenclature</b>	<b>III</b>
<b>List of figures</b>	<b>VI</b>
<b>List of tables</b>	<b>IX</b>
<b>1. Introduction</b>	<b>1</b>
1.1. Nuclear fusion and ITER	1
1.1.1. Nuclear fusion	1
1.1.2. ITER	2
1.2. Cooling schemes and heat sinks	2
1.2.1. Heat sinks	6
1.3. Hypervapotron cooling	6
1.4. Previous works related to this thesis	10
1.5. Objectives of the work	12
<b>2. Experimental database</b>	<b>13</b>
2.1. Efremov institute dataset	13
2.1.1. Mockup geometry	13
2.1.2. Flat channel	15
2.1.3. Hypervapotron	18
2.2. JET data	21
2.2.1. Boxscraper	22
2.2.2. Mki	23
2.2.3. Div 4x3 and Div 6x6	25
<b>3. Models description</b>	<b>28</b>
3.1. Introduction	28
3.2. Governing equations	29
3.2.1. Single phase flow	29
3.2.2. Multiphase flow	30
3.2.2.1. The Eulerian model	30
3.2.2.2. Volume of fluid model	33
3.3. Boiling models	34
3.3.1. RPI model	34

3.3.2. BR model	35
3.3.3. Rohsenow model	37
3.3.4. Transition boiling model	38
3.4. Turbulence model	39
<b>4. Computational results and comparison with experiment</b>	<b>43</b>
4.1. Flat channel	43
4.1.1. Grid generation and selection	43
4.1.2. RPI model	44
4.1.3. BR model	47
4.1.4. Rohsenow model	51
4.1.5. Comparison of results	56
4.2. Hypervapotron	57
4.2.1. Efremov institute data	57
4.2.1.1. Rohsenow model	58
4.2.2. JET data	60
4.2.2.1. Rohsenow model	62
4.2.2.1.1. Grid selection	62
4.2.2.1.2. Calibration of model parameters	64
4.2.2.1.3. Div 4x3	65
4.2.2.1.4. Boxscraper	69
4.2.2.1.5. Div 6x6	71
4.2.2.1.6. MkI	73
4.2.2.2. Transition boiling model	75
4.2.2.2.1. Div 4x3	77
4.2.2.2.2. Boxscraper, Div 6x6, MkI	79
4.2.2.2.3. Comparison of results	81
<b>5. Conclusions and future work</b>	<b>84</b>
5.1. Summary and conclusions	84
5.2. Future work	86
<b>References</b>	<b>87</b>
<b>Appendix A</b>	
<b>Appendix B</b>	

# 1. Introduction

This thesis is about the Computational Thermal Fluid Dynamic (CtFD) analysis of Cooling Systems for Fusion Reactor Components. The work is concerned with components related to High Heat Flux (HHF) devices and the Superconducting Magnets, which are essential to build a reactor.

The major part of the work is carried out to predict the thermal hydraulic performance of a heat sink device known as Hypervapotron, which is one of the potential candidates considered for cooling the High heat flux components, e.g. the First Wall (FW), Divertor Vertical Target, Dump Target and Neutral Beam Injection (NBI) system (figure 1-3), [1, 5-8] in the International Thermo Nuclear Experimental Reactor (ITER) [9].

The minor part is related to the computation of the JT-60SA TF coil temperature margin using the 4C code (Appendix A).

## 1.1. Nuclear Fusion and ITER

The increase in demand for energy and limited availability of fossil fuels led the research towards new ways of energy production. Among all the available choices nuclear fusion energy has several advantages such as

1. No production of greenhouse gases.
2. No long-lived radioactive waste.
3. Inherent safety features; and almost unlimited fuel supplies.
4. Fusion power would provide much more energy for a given weight of fuel than any technology currently in use.
5. Fusion could provide very high power-generation density and uninterrupted power delivery [10].

In the following sections a brief introduction is presented about the nuclear fusion and ITER.

### 1.1.1. Nuclear Fusion

When light elements are fused together or heavy elements are split apart they release energy, as the resulting intermediate elements are lighter in mass per nucleon. According to Einstein's mass-energy relationship the excess mass is released in the form of energy according to the following formula 1.1.

$$E = (\Delta m)c^2 \tag{1.1}$$

Where  $E$  represents energy,  $\Delta m$  is the change of total mass and  $c$  is speed of light.

The nuclear fusion process occurs when the light nuclei fuse together and form heavier nuclei. This process naturally occurs in the stars including our sun where the gravitational forces create the necessary conditions for the fusion of hydrogen (which is fuel) atoms to produce helium. In order to produce fusion reactions on earth and to extract the energy released we need to build a proper reactor. Ideally a reactor should keep the fuel at a sufficient high pressure (product of density times the temperature) for a sufficiently long time, while providing a barrier between the fuel-filled region and the external environment. Large temperatures are required to achieve sufficiently high velocities, allowing to overcome the repulsive force between the positive nuclei and the occurrence of the fusion reactions. The required temperatures are of the order of few hundred million Kelvin, at these high temperatures the fuel is “plasma”, i.e. a fully ionized gas containing positive ions and negative electrons.

Plasma confinement can be done in different ways: magnetic, inertial, electrostatic etc. Among these magnetic confinement of plasma is more promising for energy production. Several magnetic fusion experiments exist, such as the Joint European Torus (JET) [10], Toresupra [11]. However, it has been possible to obtain only marginal net energy so far, largely insufficient for economical purpose. In the next generation of experiments, ITER aims at achieving a substantial net energy production [9].

### **1.1.2. ITER**

ITER is based on the 'Tokamak' concept of magnetic confinement, in which the plasma is contained in a toroidal shaped vacuum vessel, uses a mixture of deuterium and tritium as fuel. Without the benefit of the very high pressures generated by gravity in stars, ITER requires very high temperatures to achieve fusion conditions, of the order of 150 million K [9]. Strong magnetic fields are used to confine the plasma; these are produced by a mixture of the so-called plasma current flowing in the plasma and external superconducting coil systems.

During the operation of ITER, some components such as FW, Divertor vertical target, dump target and NBI system (figure 1-3) are subjected to operating conditions characterized by extremely high thermal loads which can be as high as  $5 \text{ MW/m}^2$  [1]. In order to prevent damaging the machine it is required to design actively cooled heat sinks for the plasma facing and all the high heat flux components.

## **1.2. Cooling schemes and heat sinks**

Subcooled flow boiling devices (usually using water) can accommodate high heat fluxes due to the large Heat transfer Coefficient (HTC) associated with the subcooled flow boiling regime.

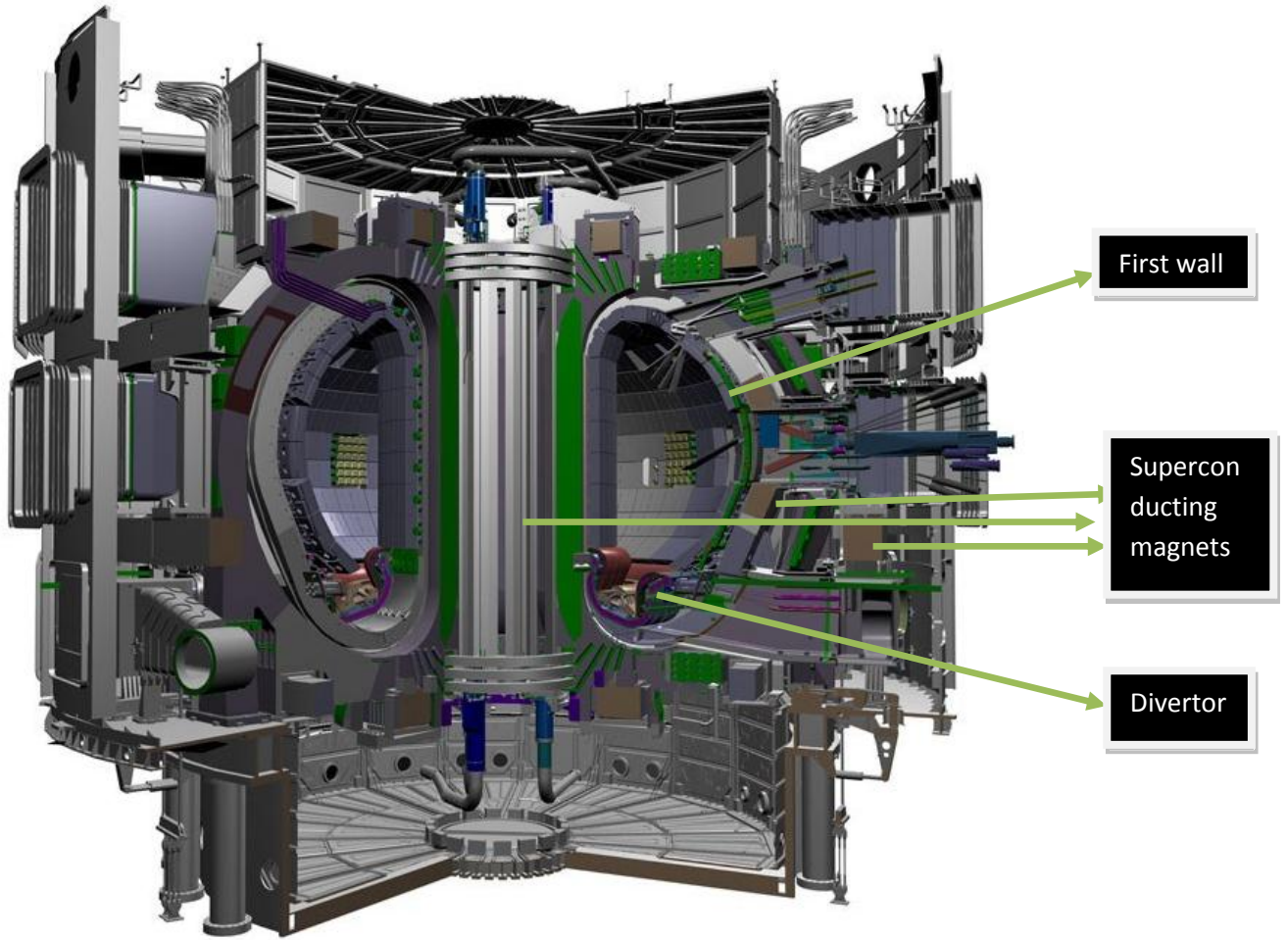


Fig 1: ITER [9]

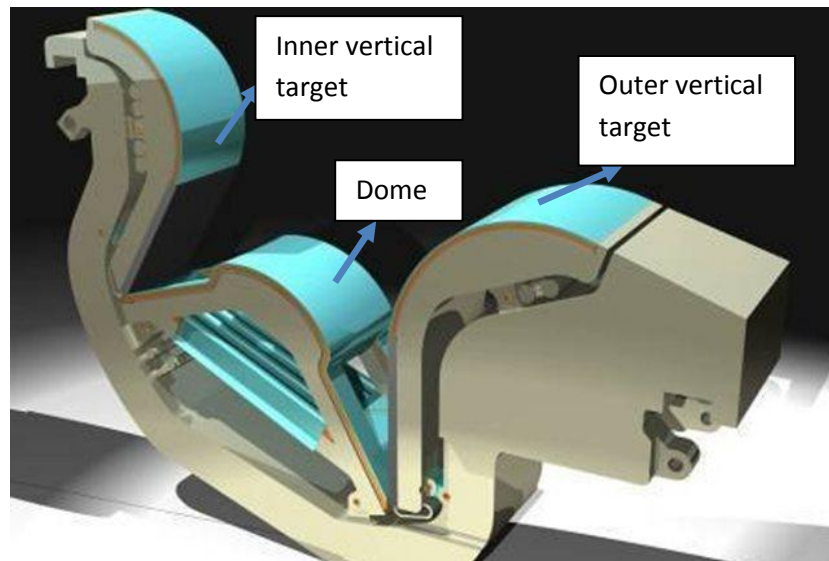


Fig 2: Divertor [9]



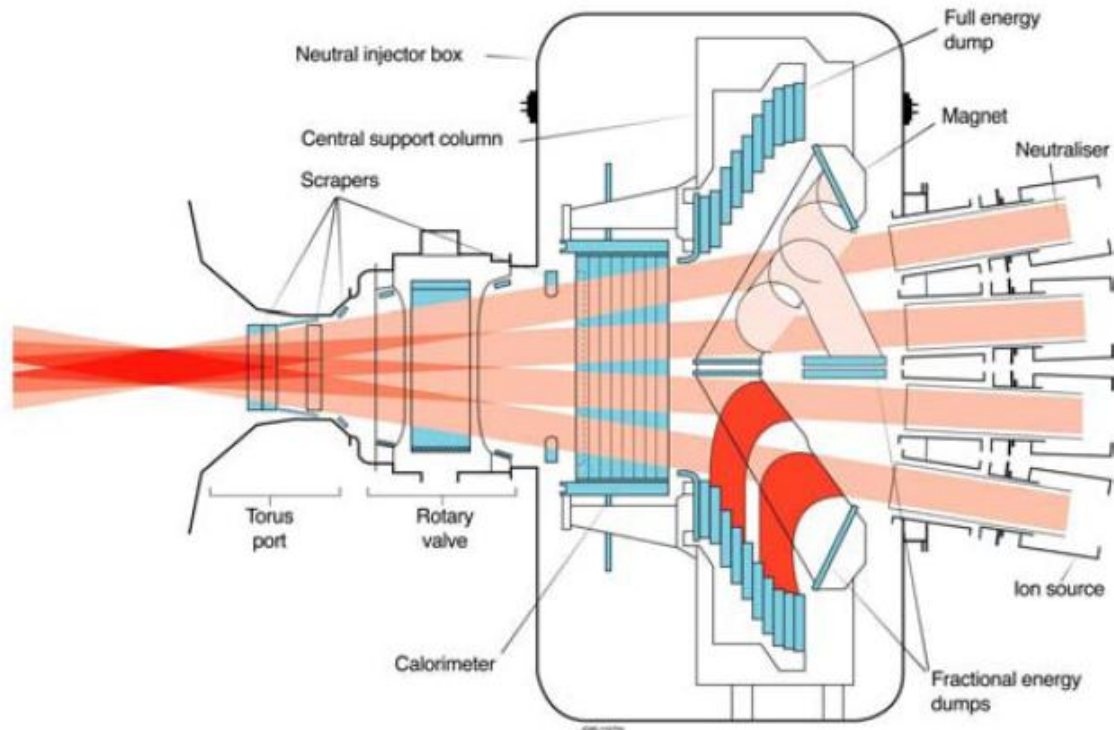


Fig 3: Neutral beam injection system

## Boiling

Boiling is a phenomenon where the fluid changes its phase from liquid to vapor while absorbing enormous amount of energy as latent heat. So the heat transfer coefficients associated with boiling are very high. In general there are two types of boiling: pool boiling and flow (or forced convection) boiling. Pool boiling occurs on a submerged heating surface, in a pool of liquid at rest. Flow boiling occurs in a flowing stream of liquid; here the heating surface may be the channel wall through which the flow occurs. Once the boiling has started the flow is composed of a mixture of liquid and vapor and this type of flow is called as two-phase flow. Figure 4 shows an example boiling curve where the plot shows variation of heat flux with the wall superheat depicting different boiling regions.

Initially the cooling is done by forced convection, using the mechanism of single phase heat transfer (from A-B). In the range B-C, the liquid near the wall is superheated and tends to evaporate, forming bubbles in the vicinity of nucleation sites on the surface. The bubbles transport the latent heat and also increase the convective heat transfer by agitating the liquid near the heating surface. The mechanism in this range is called nucleate boiling and is characterized by a very high heat transfer rate for only a small temperature difference. There are two sub regimes in nucleate boiling: the first one is called local boiling or sub cooled nucleate boiling and the second one is called bulk boiling or saturated nucleate boiling. Local boiling is nucleate

boiling in a sub-cooled liquid, where the bubbles formed at the heating surface condense locally. Bulk boiling is nucleate boiling in a saturated liquid; in this case, the bubbles do not collapse.

When the population of bubbles due to heating becomes too high at some heat flux value such as point C, the outgoing bubbles may obstruct the path of the incoming liquid. The vapor thus forms an insulating blanket covering the heating surface, and thereby raises the surface temperature. This is called the boiling crisis, and the maximum heat flux just before reaching the crisis is called the critical heat flux (CHF).

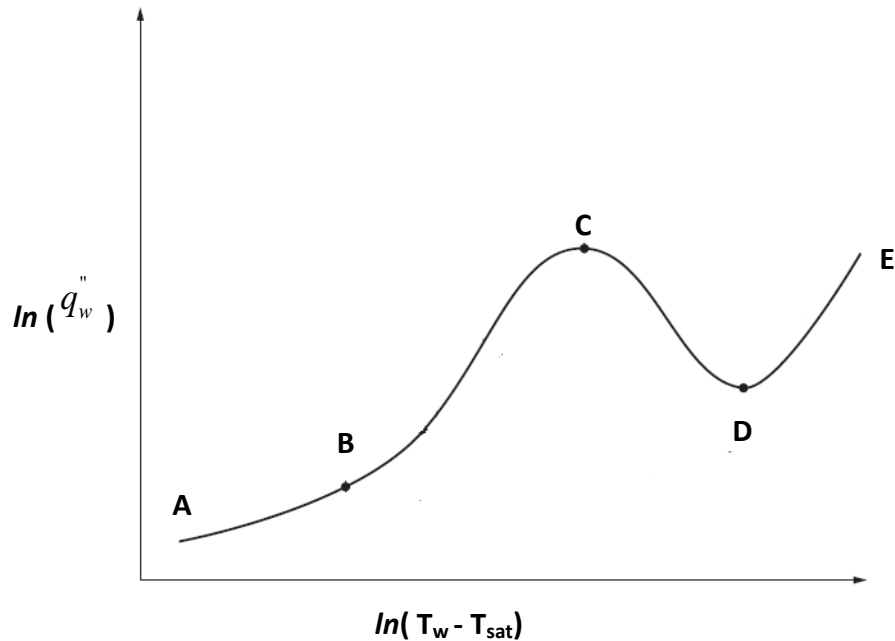


Fig 4: Boiling curve

In the range C-D, immediately after the CHF has been reached, boiling becomes unstable and the mechanism is then called partial film boiling or transition boiling. The surface is alternately covered with a vapor blanket and a liquid layer, resulting in oscillating surface temperatures. If the power input to the heater is maintained, the surface temperature increases rapidly to point D while the heat flux steadily decreases. In the range D-E, a stable vapor film is formed on the heating surface and the heat transfer rate reaches a minimum. This is called stable film boiling. By further increasing the wall temperature, the heat transfer rate also is increased by thermal radiation. However, too high a temperature would damage the wall. So for practical purpose, the temperature is limited by the material properties.

It is very important to maintain the temperatures of the surface below a particular point where we may have restrictions from the point of view of either thermal expansion of the materials if we have more than one material used for the construction of the heat sink, or thermal and structural integrity.

### **1.2.1. Heat Sinks**

For a given flow conditions (which have to be designed for lower pumping speed and lower pressures to reduce the overall cost) one would never want to exceed the CHF limit, and if possible to delay it somehow by increasing the heat transfer.

In the recent past lot of research has undergone in designing and selecting a particular heat sink among the many solutions proposed. The R&D programmes conducted in the past suggested circular channels with swirl tapes, annular channels with swirl tapes, Hypervapotrons, channels with porous coating and screw tubes [12].

Each of the above mentioned heat sinks have certain advantages and disadvantages but among these, considering the availability of experimental data on mockups, lifetime of the particular heat sink and complexity of manifolding, the preferred heat sinks are 1. Tubes with swirl insert armored with monoblocks or Swirl Tube (ST), 2. Hypervapotron concept with Flat tiles (HV) [12- 14].

Study done by author's [12- 14] shows that HV and ST are comparable for CHF and pumping power with respect to the uncertainties in the experimental data, so the choice between the two concepts should be based on other considerations such as: (1) cost and ease of fabrication, (2) ease of brazing and (3) volume and reliability of available experimental data. These considerations lead to the conclusion that the choice of concept will depend on the particular application. A study done [14- 16] based on above concepts reveals that bonding of flat tiles is easier, volume of armour material attached to the heat sink is lower and the flat tile concept is expected to be cheaper than ST.

### **1.3. Hypervapotron cooling**

Historically, the so called Hypervapotron concept with enhanced cooling capabilities implying boiling/condensation effects due to a fin design was developed by Thomson CSF tube Company [17] and later designed for neutral beam heating systems [18]. Falter et al in 1983 [19] described the first test results of a rectangular HV design destined for a fusion application. Figure 5 shows cross and lateral sections of a typical Hypervapotron geometry. As explained by Cattadori et.al [20], the Hypervapotron operation is characterized by the following succession of events,

When sufficient heat flux is applied to the wall which is in contact with the Hypervapotron fins, the liquid in between two adjacent fins starts boiling, while the bulk of the fluid in forced convective flow is still in subcooled conditions. When steam has filled-up a slot, it undergoes quick condensation in the bulk subcooled liquid, thus the emptying the slot which is replenished with fresh cold liquid. The heated wall is rewetted as long as the wall temperature during the uncovered wall phase does not exceed the value of the Leidenfrost

temperature (at which film boiling becomes unstable). This phenomenon of continuous boiling and condensation between the slots increases the critical heat flux, as the boiling and condensation process draws and gives the latent heat to the coolant outside the fins. Cattadori has done detailed experiments on Hypervapotron and figure 6 shows the above process of condensation and boiling inside Hypervapotron.

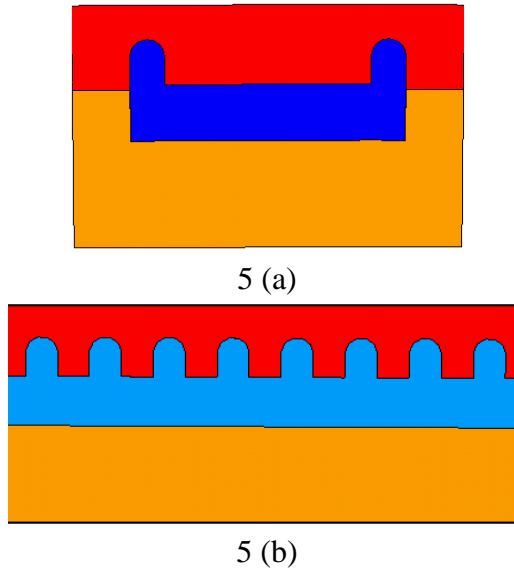


Fig 5: The cross (a) and lateral (b) sections of Hypervapotron

From his experiments Cattadori concluded that

1. The presence of three different heat transfer zones (in the first zone there is a linear relationship between the heat flux and temperature, with no steam inside the slots, the second zone is characterized by the presence of subcooled boiling and a third zone, which ends with the physical burnout and is characterized by a steep increase in the wall temperature) characterized by three different average values of heat transfer coefficient. The transition from one zone to the other as well as the heat transfer rate in the zones is dependent on fin geometry and fluid thermal hydraulic conditions.
2. The occurrence of Hypervapotron effect as explained in the above section is linked to low values [20] of liquid velocity and subcooling.

From the experiments conducted by Frédéric Escourbiac et al. [21] it is found that CHF of Hypervapotron decreases as the width of the channel is increased, and he says ‘one can assume that water enters better the slots from the lateral groove if the mock-up is narrow’.

Some more detailed experiments were also conducted by Peipei Chen [22] using R-134a in compact Hypervapotron structures, and he also compared the results with Flat channel (channel with rectangular cross-section) and gave some interesting results, which are summarized below.

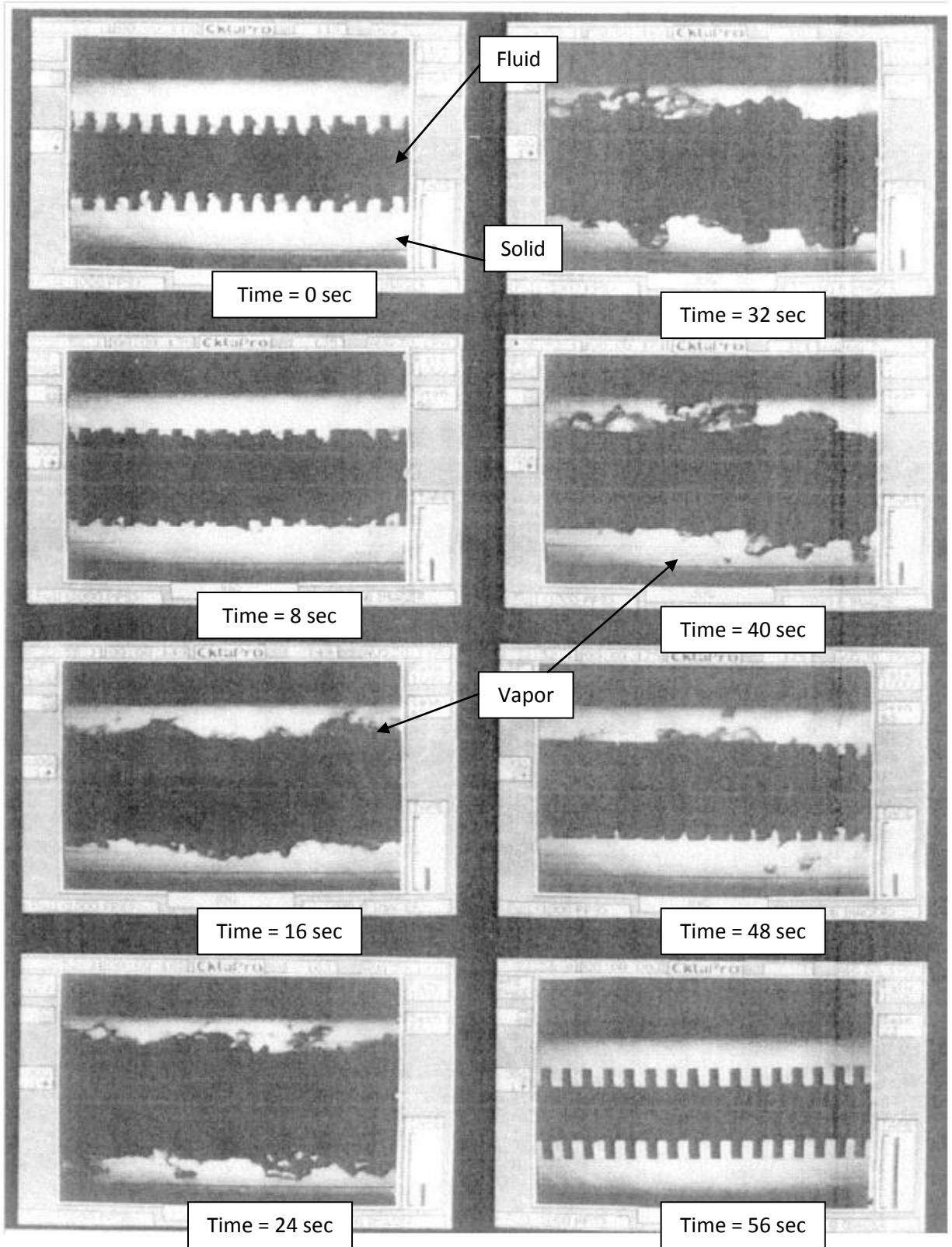


Fig 6: Cattadori's visualization of the Hypervapotron effect occurrence [20]

Two distinctive zones were identified in the boiling process of the Hypervapotron. In the first zone the nucleate boiling regions show a power law relation between wall super heat and wall heat flux as shown in the figure 7 (where different data i.e. HV 5-9 represents Hypervapotrons with different operating conditions), here the Hypervapotron exhibits similar behavior to flat channels, where the heat flux is mainly controlled by development of the boiling process. The second zone departs from the power law in the first zone, where the nucleation density in the Hypervapotron cavity reaches maximum which he called as the nucleation “saturation” will reduce the heat transfer compared to the first zone. From the experiments conducted on Flat channel and Hypervapotron he concludes that the Hypervapotron structure provides approximately 40–50% higher values of CHF.

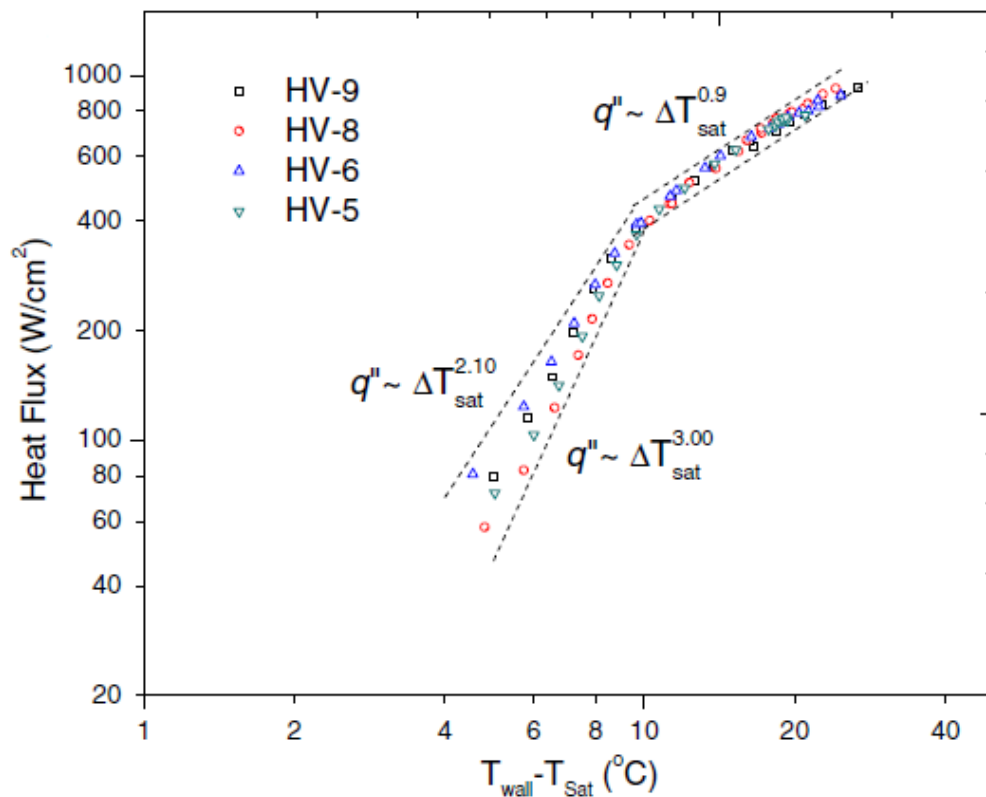


Fig 7: Boiling curve for fully developed flow boiling in Hypervapotron [22]

Apart from these experiments, several other experimental campaigns were conducted, e.g. at JET, Efremov institute (Russia) and Toresupra., for different reactor high heat flux components, some of these experimental campaigns will be illustrated in chapter 2.

It is very important to carry out the analysis of Hypervapotron using computational fluid dynamics (CFD), as CFD allows the analysis of fluid flow problems in detail, faster and earlier in the design cycle than possible with experiments, costing less money and lowering the risks involved in the design process.

## 1.4. Previous works related to this thesis

In the recent past several authors tried to do the analysis of Hypervapotron using CFD with different computer codes, boiling models and methodologies.

The first attempts to do the analysis of Hypervapotron was conducted by Baxi et al [23] where he developed an analytical method to predict the performance of Hypervapotron which uses 3 different correlations for the different boiling regions (Forced convection: Dittus-Boelter Correlation, Nucleate boiling: Thorn's correlation, Critical Heat Flux Macbeth correlation for high mass flux water flow, to all these correlations some modifications were done). They used the TOPAZ2D code for doing the finite element analysis, aiming mainly at calculating the temperature distribution in the Hypervapotron.

Recently Pascal-Ribot et al [24] have done a complete 3D analysis of Hypervapotron using two codes *Syrthes* (code for heat conduction calculations in solids) and *Neptune* (code for two phase thermal hydraulics simulation). They used a boiling model based on the work from Seiler et al [25], which itself is based on the Podowski's approach [26]. In this work he compared the effect of 3D vs 2D simulations and commented that 3D simulations give better description of the general behavior of the heat sink temperature evolution than the 2D axial simulations, thanks to the possibility to include the side channel in the computational domain.

In 2009 Youchison et al [27] have done CFD analysis of Hypervapotron using the commercial CFD code ANSYS-FLUENT, for a first wall Hypervapotron finger, with the RPI boiling model [26]. They concluded from these simulations that the Fluent RPI boiling model can be unstable under certain flow conditions; this may be due to the applicability of the boiling model up to the region of nucleate boiling regime. Later in 2010 [28] Youchison compared two CFD codes STAR-CCM++ and ANSYS-FLUENT using the same geometry and found that Fluent simulations did not reach equilibrium conditions before the solver encountered numerical instabilities, whereas STAR-CCM+ did reach equilibrium conditions without any problem. In 2011 Youchison [29] used STAR-CCM+, which contains the Rohsenow boiling model for the nucleate boiling regime and has a capability of transition to the film boiling regime for very high heat fluxes. To validate the model he started benchmarking the code on flat channel geometry, and calibrated the model free parameters. Later he used the parameters previously determined for the Hypervapotron geometry getting results in good agreement with experimental data with errors in the range of  $\pm 10$  C. Later he also did analysis of different Hypervapotron geometries varying the ratio of teeth to channel size [30].

In 2010 Ling Tao et al [31] have done the analysis on Hypervapotron by developing a numerical simulation model, the boiling model was similar to of the one used by Pascal Ribot [24], the simulated results were in good agreement with the experimental data.

In 2011 A. Ying et al [32] used a commercial CFD code Sc/Tetra and addressed the applicability of Bergles and Rosnow nucleate boiling model, the analysis was performed on Flat channel and Hypervapotron water flow configurations, though the BR model applicability is only limited to low to moderate heat fluxes.

In 2010 Joseph Milnes have completed his thesis [19], where he had done extensive work on understanding the origin, design philosophy and development of the Hypervapotron. He used ANSYS CFX with the RPI boiling model for his work. He also tried to obtain a qualitative assessment of RANS models for Hypervapotron flow and heat transfer and concluded that the SST k-omega turbulence model as in ANSYS CFX, applied to a sufficiently fine grid, gives most accurate predictions of single phase cavity flow and heat transfer [33]. He also compared the results obtained his simulations with experimental data available from different sources. From his results it can be concluded that this method is applicable only for single phase and nucleate boiling regimes [34]. He also tried to modify the geometry of the Hypervapotron to improve the thermal performance, finally stating that square-bottomed cavity performs better than any other simple shape.

In 2012 Zhongwei Wang et al have done optimization of Hypervapotron geometry using six different fin designs [35] as shown in the figure 8.

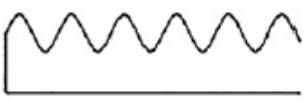
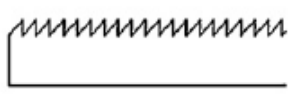
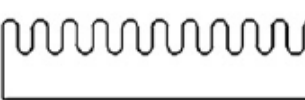
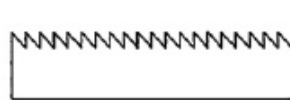
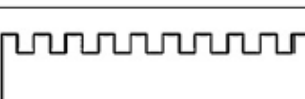
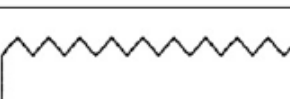
Number	Fin shape	Configuration	Number	Fin shape	Configuration
1	Sin curve		4	Triangle to the flow direction	
2	Rectangle with fillet		5	Triangle against the flow direction	
3	Rectangle		6	Right-angle triangle	

Fig 8: Different Hypervapotron configurations considered by Z.wang et al [35]

For their analysis they used ANSYS-FLUENT, writing their own UDF for the boiling model to define the mass transfer between liquid and vapor phase, and he concluded his paper saying that best fin design is the triangle against the flow direction design.



Though many authors have tried to see the Hypervapotron effect using different computational tools and boiling models, the final results are mostly confined to the single phase and nucleate boiling regime, none of them try to elaborate the applicability of model beyond the nucleate boiling regime using their simulations.

## **1.5. Objectives of the work**

The objectives of the present work are, to test the suitability and accuracy of various boiling models available in commercial CFD codes for predicting the Hypervapotron thermal performance, and compare the results obtained by running the simulations (with the boiling models) whenever possible.

So far authors have tried to cover the boiling regimes up to nucleate boiling, here we have also tried to validate our results both qualitatively (in terms of following the characteristic nature of the experimental data) and quantitatively (in terms of getting simulated results closer to the experimental data) extending on to hard boiling region (it refers to the violent, noisy boiling that occurs at high heat fluxes, often corresponding to a drop in heat transfer efficiency [20, 36]).

Apart from the work which is done on Hypervapotron, I have also worked on the Computation of JT60SA temperature margin using 4C code (Cryogenic Circuit Conductor and Coil code); the details of this work can be found in appendix A. During this project I tried to understand the physics of superconducting magnets, the thermal hydraulic aspects that are relevant to the coils and physics behind calculating the temperature margin. The main objective of this work was to estimate the temperature margin of the coil for a given heat load on the coil as well as structures, magnetic field maps on coils and inlet conditions for the coil.

# 2. Experimental data

In this section, the experimental data used for testing the boiling models for estimating the thermal performance of Hypervapotron are discussed. The data were acquired from experiments conducted at two different places.

The first data set comes from Efremov institute (Russia), which hosts the Tsefey e-beam testing facility [37, 38], the experiments were conducted on two different configurations, Flat channel and Hypervapotron respectively. The experiments were conducted to define the critical heat fluxes for a range of possible flow parameters.

The second data set is acquired from experiments conducted at JET [10] involving Hypervapotrons with different cavity shapes, range of heat fluxes and inlet conditions.

## 2.1. Efremov Institute data set

### 2.1.1. Mockup geometry

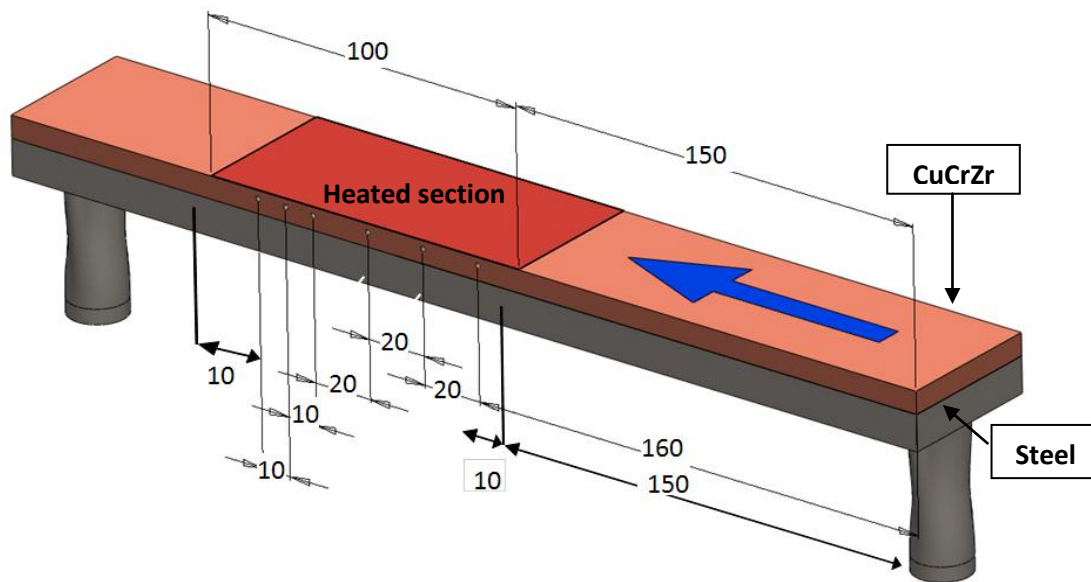


Fig 9: 3D sketch of the experimental test section geometry (the dark region on the top marks the heated surface, all dimensions are in mm).

The mockup used for conducting the experiments on both Flat channel and Hypervapotron is shown in figure 9. In the experimental apparatus the entrance and exit ducts are orthogonal to the fluid flow in the main channel. This provides a sharp change in direction of the

flow field which helps increasing turbulence. The length of the heated section spans over 100 mm, which is shown as the dark region in figure 9, along with the direction of the fluid flow (blue arrow). To measure the temperature in the mockup, a set of thermocouples is inserted 1.5 mm below the heated surface and 10, 70, 80 and 90 mm from the starting of heated surface (in the mockup actually 6 thermocouples were inserted but among them only 4 are reliable/available). Surface heat loading was provided by scanned e-beam and a mask [38]. The heat flux was measured calorimetrically by taking into account fixed loading area, measured water flow rate and water inlet/outlet thermocouples difference. The mock up is a composite of CuCrZr and steel [38].

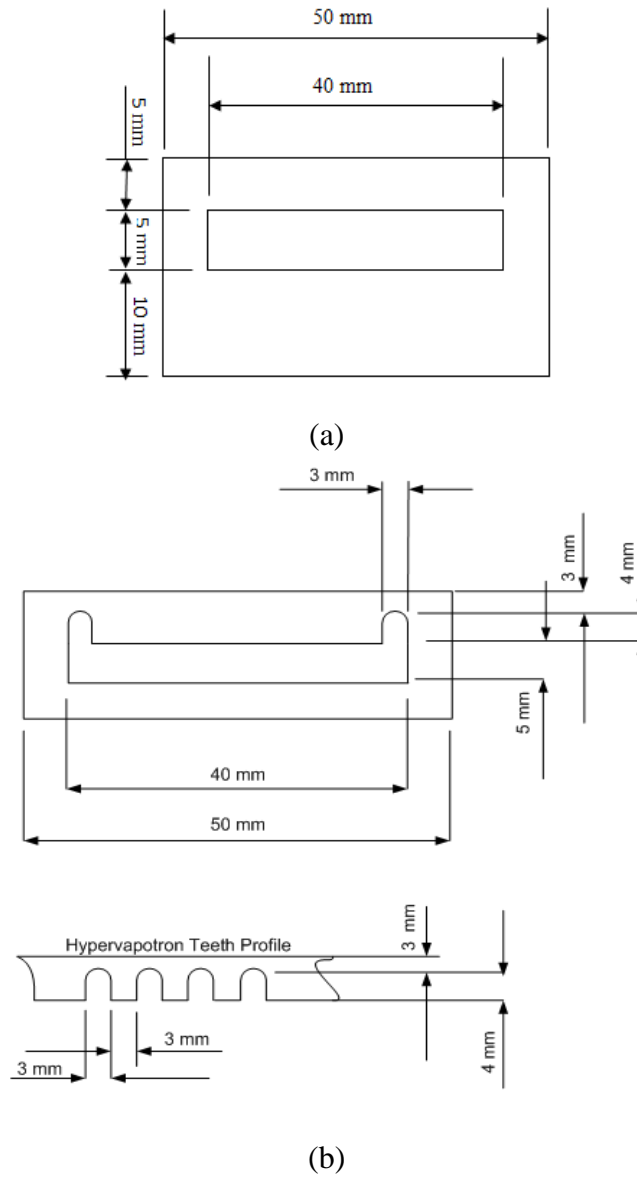


Fig 10: (a) Flat channel cross section (b) Cross (top) and longitudinal (bottom) sections of the Hypervapotron channel.

Two different cross-sections are used to do the experiments conducted at Efremov, the first is a Flat channel and the second is Hypervapotron. Figure 10 shows the cross-section of the Flat channel, cross and lateral sections of the Hypervapotron, along with their dimensions. The inlet temperature is maintained about  $125 \pm 5$  C, and the pressure is maintained about 2 Mpa, corresponding to a sub cooling of the order of  $\sim 90$  C.

### 2.1.2. Flat Channel

An example of the experimental data given for Flat channel is shown in figure 11, for 1 m/s inlet velocity and  $2 \text{ MW/m}^2$  heat flux. On y-axis to the left we have temperature at the location of thermocouples, on the right we have temperature measured at inlet and outlet and on the x-axis the time duration is shown for which the experiment was undergone. So the plot shows the temperature time evolution at the thermocouple and inlet/outlet locations.

Figure 12 shows the variation of temperature at thermocouple locations, inlet and outlet with time for 1 m/s inlet velocity and  $4 \text{ MW/m}^2$  heat flux, which is described as CHF limit for this case.

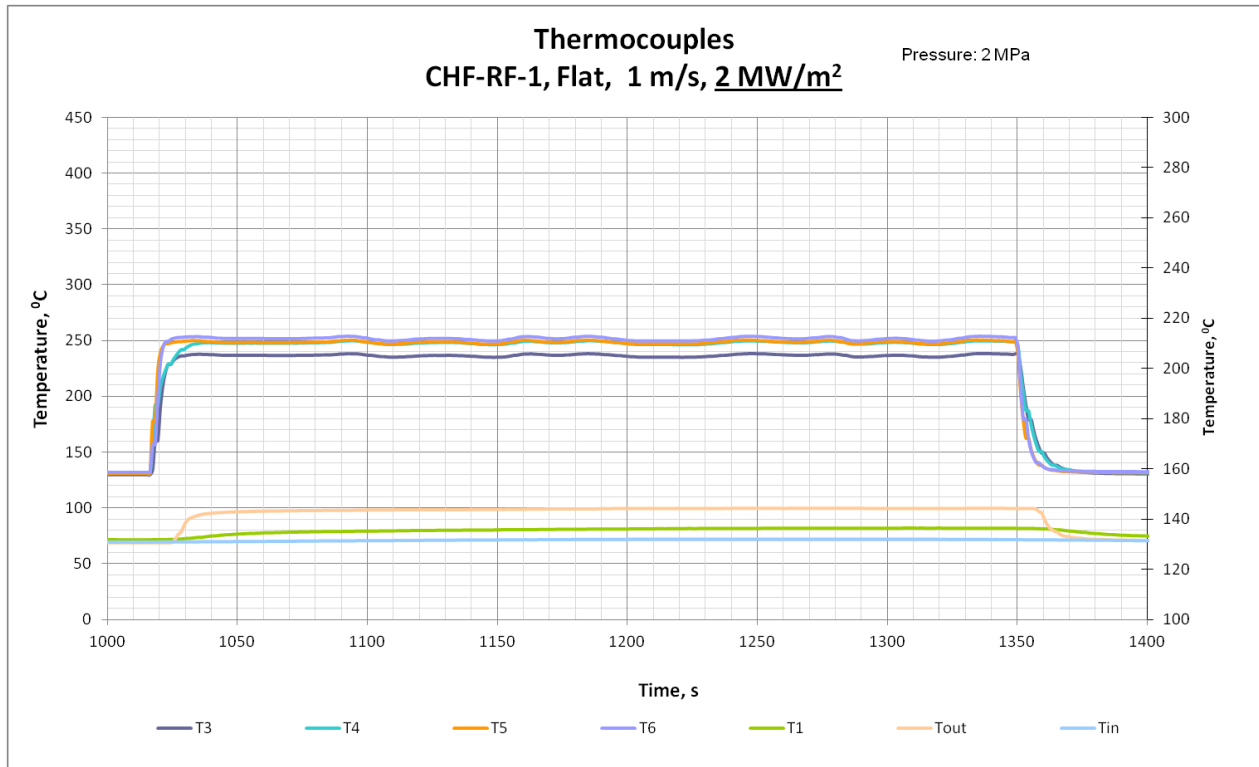


Fig 11: The temperature evolution as a function of time at different thermocouple locations (inlet velocity 1 m/s and heat flux  $2 \text{ MW/m}^2$ )

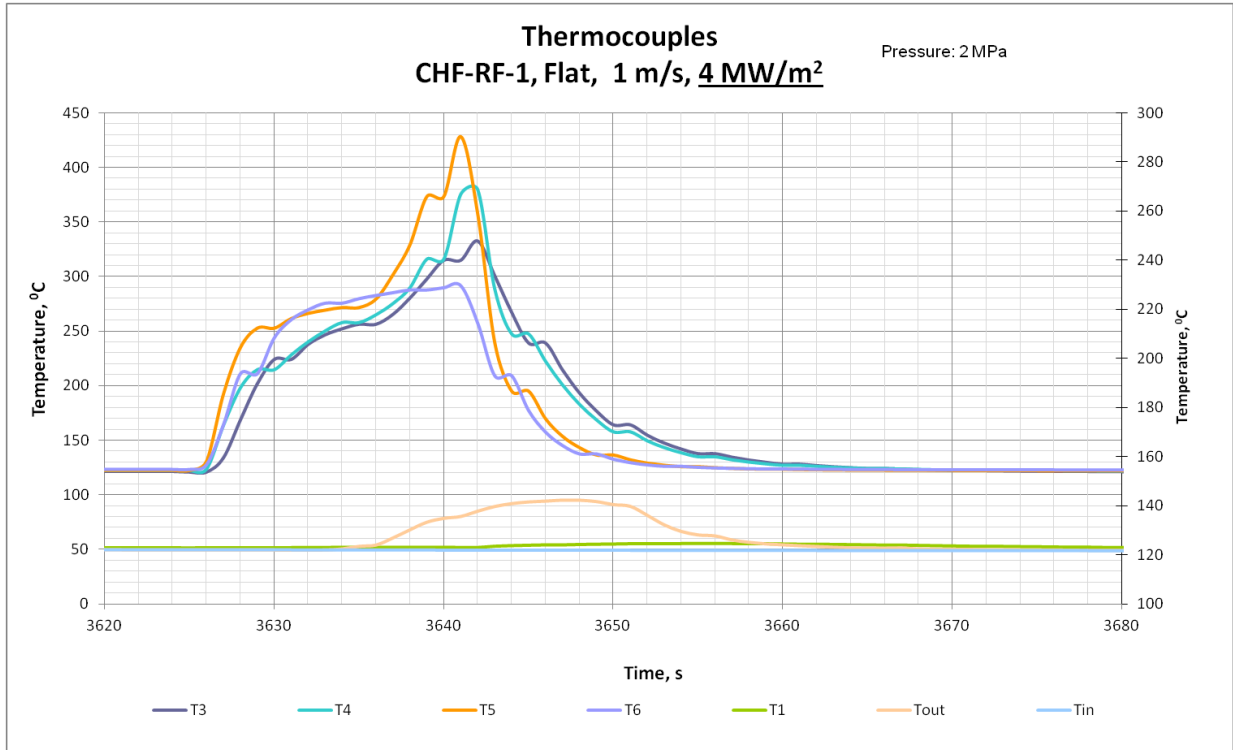
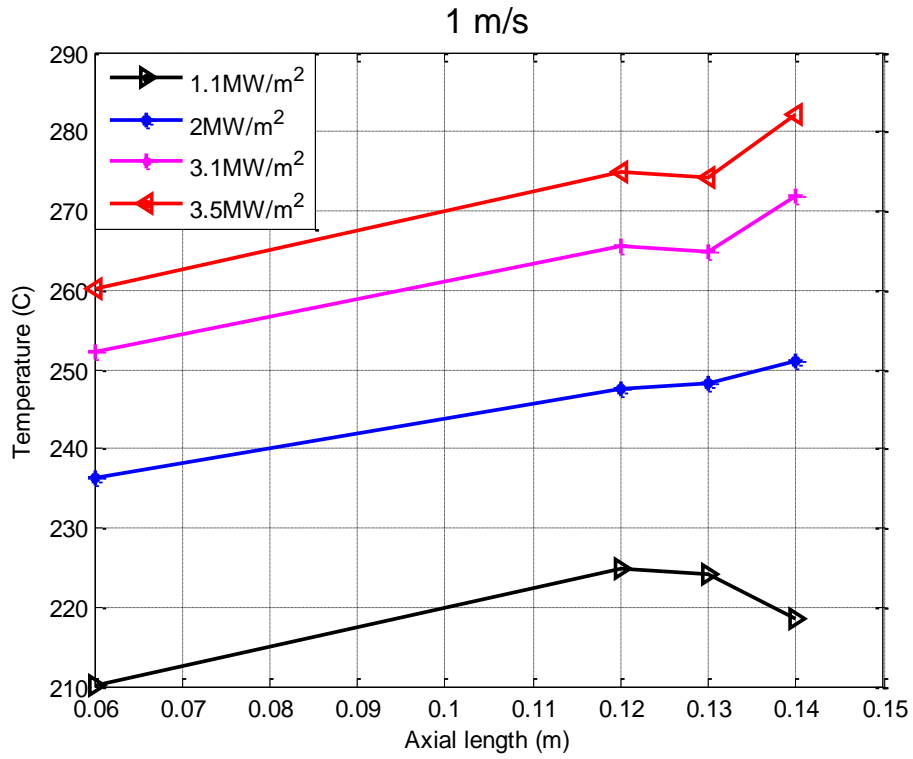


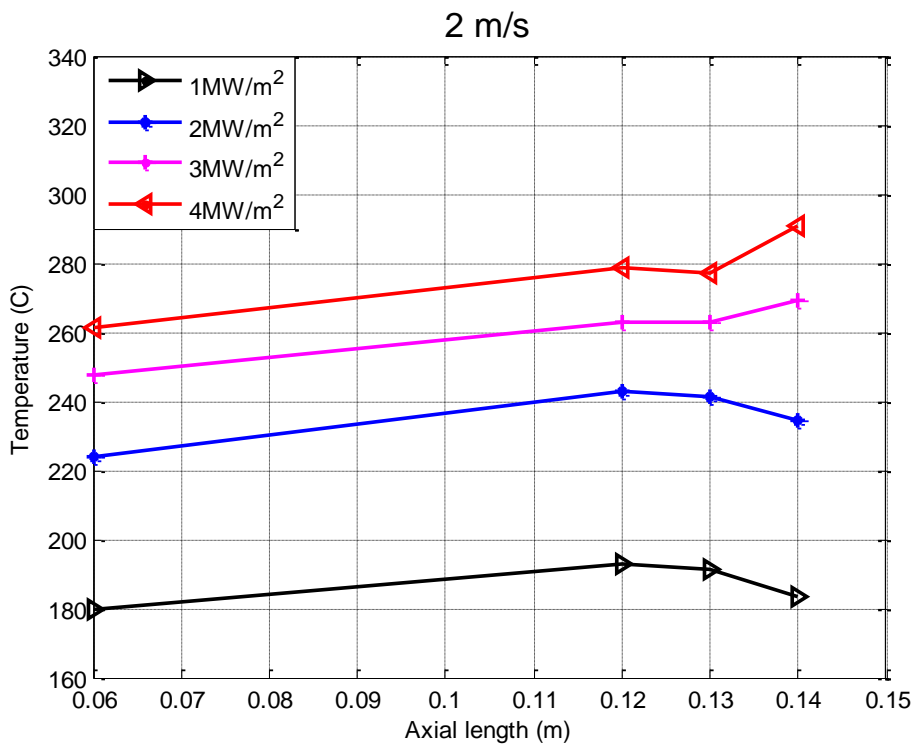
Fig 12: The temperature evolution as a function of time at different thermocouple locations , showing the instability in the surface temperature due to occurrence of CHF (inlet velocity 1 m/s and heat flux 4 MW/m<sup>2</sup>)

From figure 11 it can be observed that for this particular inlet conditions and heat flux the experiment was conducted for 400 sec. Once the initial ramp-up period is over it can be observed from figure 11 that, for the remaining period of time before the ramp-down the device is almost in a steady state condition, so it is decided to take a single value for each thermocouple. This is achieved by averaging the data of each thermocouple measurement with respect to time, for example in figure 11 the data are averaged from 1050 sec to 1140 sec so that a single value can be used to characterize the record of each thermocouple during that period. Figure 13 shows the data obtained by following the similar strategy for all the available heat fluxes and inlet conditions. This data is used for comparison with the simulations performed in this thesis.

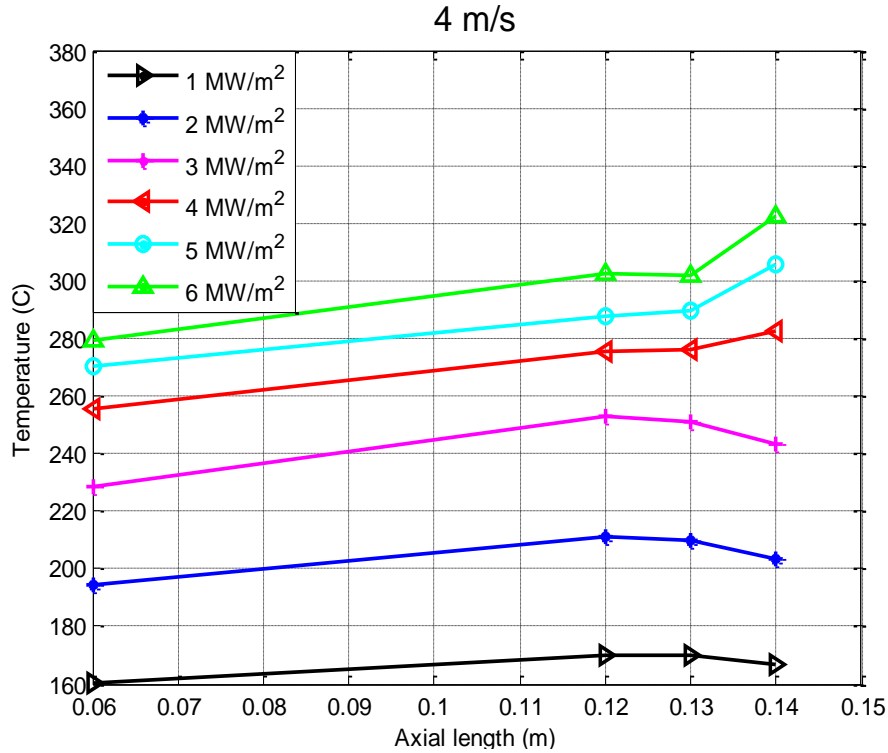
The data from the experiments also show the stochastic nature of the CHF as shown in figure 12. Where for 4 MW/m<sup>2</sup> heat flux, the instability is obtained due to the quickly growing vapor film causing a rapid increase in the temperature of the surface (which is shown in the figure 12 by the recorded thermocouple response), within few seconds from the start of the heating phase, without going to steady state. A similar behavior of temperature excursion for CHF conditions is observed for all inlet velocities.



13 (a)



13 (b)



13 (c)

Fig 13: Flat channel data, for (a) 1m/s inlet velocity, (b) 2 m/s inlet velocity, (c) 4 m/s inlet velocity at different heat fluxes.

It can be observed from figure 13 that, for higher heat fluxes, temperature at the end of the heated section (heated section goes from 0.05 m to 0.15 m) increases. This behavior is observed in all the cases with different inlet velocities and high heat fluxes.

### 2.1.3. Hypervapotron

An example of the experimental data given for Hypervapotron is shown in figure 14, for 1 m/s inlet velocity and 3 MW/m<sup>2</sup> heat flux, where the plot shows the variation of temperature at thermocouple locations (on the left of y-axis) and inlet and outlet (on the right of y-axis) with respect to time. Figure 15 shows the variation of temperatures at thermocouple locations, inlet and outlet with time for 1 m/s inlet velocity and 6 MW/m<sup>2</sup> heat flux, which is described as CHF limit for this case. The same method used for the Flat channel to average the thermocouple temperature over time is also applied to these data. The final temperatures used to compare with the simulated data are shown in figure 16.

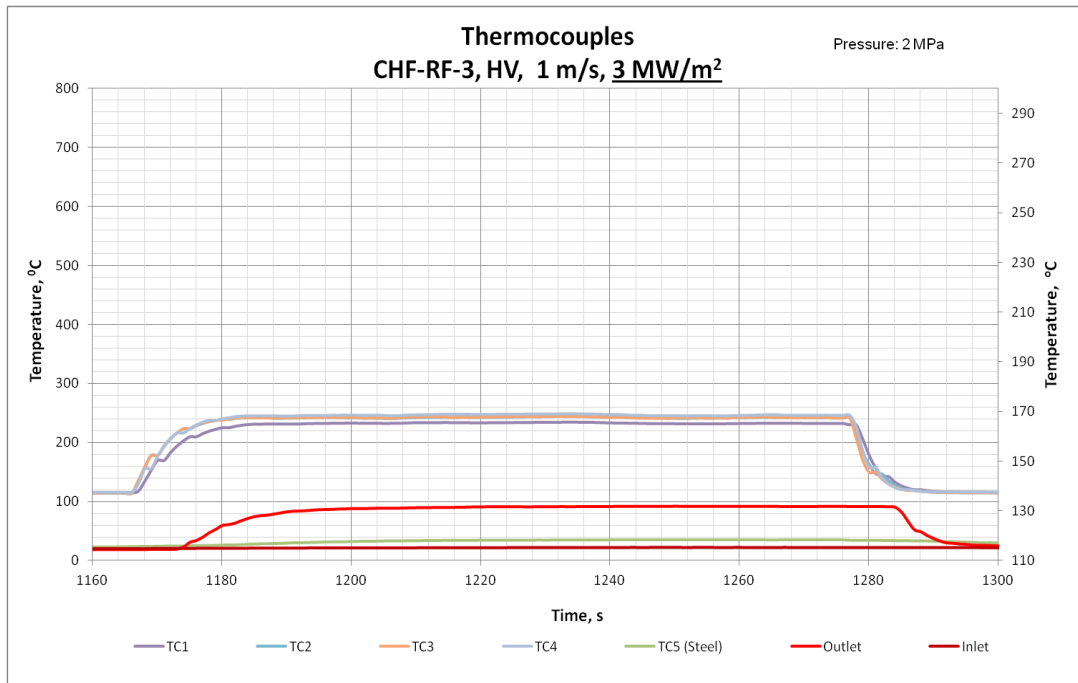


Fig 14: Temperature evolution as a function of time at different thermocouple locations (inlet velocity 1 m/s and heat flux 3 MW/m<sup>2</sup>)

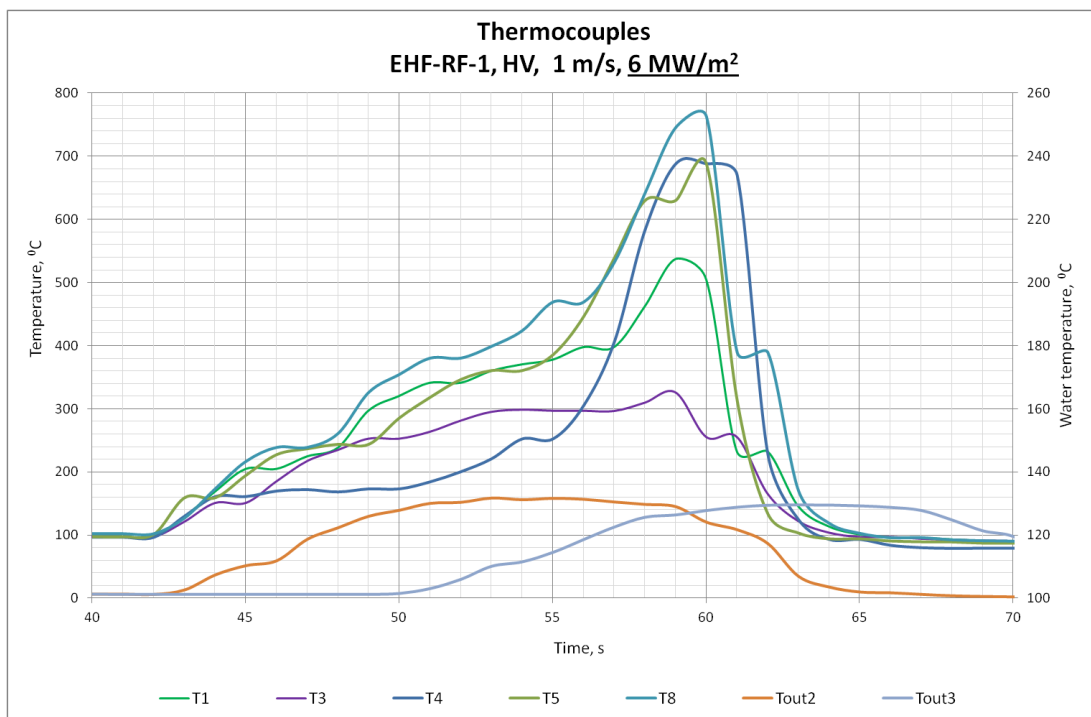
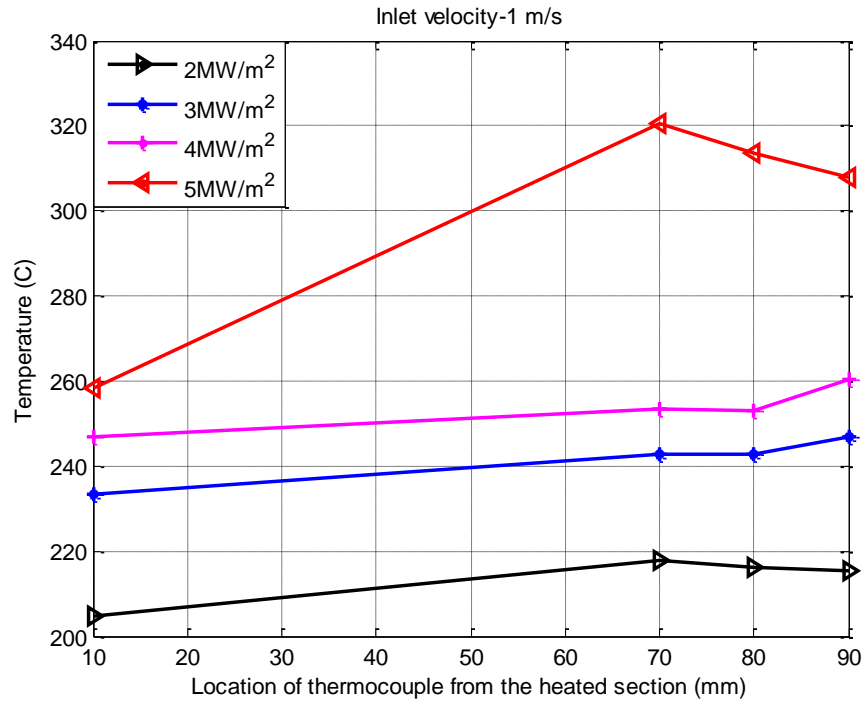
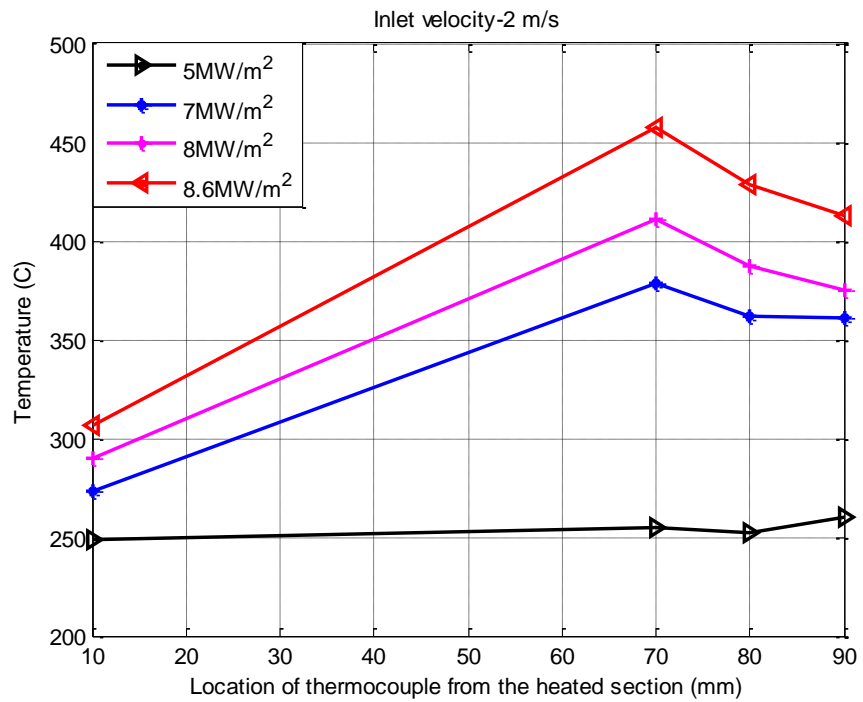


Fig 15: Temperature evolution as a function of time at different thermocouple locations , showing the instability in the surface temperature due to occurrence of CHF (inlet velocity 1 m/s and heat flux 6 MW/m<sup>2</sup>)





16 (a)



16 (b)

Fig 16: Hypervapotron data for (a) 1m/s inlet velocity (b) 2 m/s inlet velocity

From figure 16 it can be observed that the experimental data for Hypervapotron show a behavior different from that of the Flat channel. This behavior of Hypervapotron data (the temperature at second thermocouple to be higher than that of the other thermocouples), might be caused due to the positioning of the thermocouples relative to the teeth groove/tip pattern.

## 2.2. JET data

In the recent past several experiments were conducted at JET, where Hypervapotron was used to cool the Neutral Beam Injectors (NBI) and the Divertor. In this section the experimental data used by Joseph Milnes [19] for his thesis are briefly described. Since the data used in this thesis obtained from JET are similar to what was used by J.Milnes, the outcome of the simulated results can be directly compared with his work [Chapter 4 section 4.2.2.2.3]. The experimental data used by J.Milnes are described in detail in [36, 39- 41], in addition to Milnes PhD thesis itself [19].

Table 1 lists the different cavity shape and cavity sizes, together with the location of the thermocouples used in the experiments. The different shapes mentioned are shown in figure 17.

Table 1: Summary of Hypervapotron validation cases [19]

<b>Hypervapotron design</b>	Boxscraper	Div 4×3mm	Div 6×6mm	MkI JET
<b>Channel height</b>	8mm	3mm	6mm	10mm
<b>Channel width (z direction)</b>	48mm	21mm	21mm	48mm
<b>Cavity depth</b>	4mm	4mm	6mm	8mm
<b>Cavity width (x direction)</b>	3mm	3mm	3mm	3mm
<b>Front wall thickness</b>	4mm	3mm	3mm	6mm
<b>Cavity profile</b>	Rounded	Square	Square	Rounded
<b>Thermocouple position</b>	Between twin channels, 3mm below from front surface	In the side wall, 2mm from the front surface	In the side wall, 2mm from the front surface	Between twin channels, 3mm below from front surface

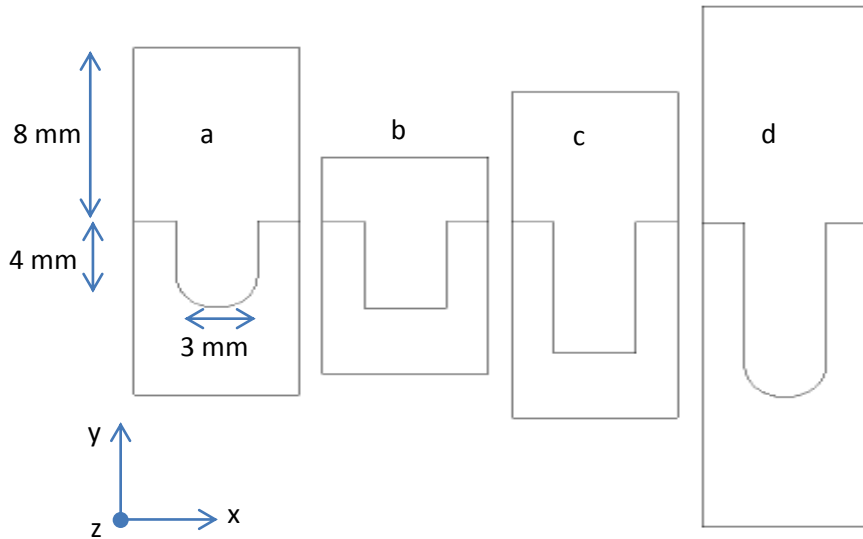


Fig 17: Hypervapotron cross-sections for a) Boxscraper, b) Div 4×3, c) Div6×6 and d) MkI respectively [19].

### 2.2.1. Boxscraper

Boxscraper is the most loaded component among all beam line elements used in JET Neutral Injector Boxes [41]. Ciric in his experiments tried to test 3 Hypervapotron elements, the first one, figure 18 (a), has standard JET Hypervapotron geometry. The second element as shown in figure 18 (b), has reduced front face thickness and reduced fin height, the third element, figure 18(c), is a full size prototype for the new Boxscraper. An additional, 1.5 mm wide, slot was machined on one half of the prototype Hypervapotron as an attempt to improve cooling of the central web [41].

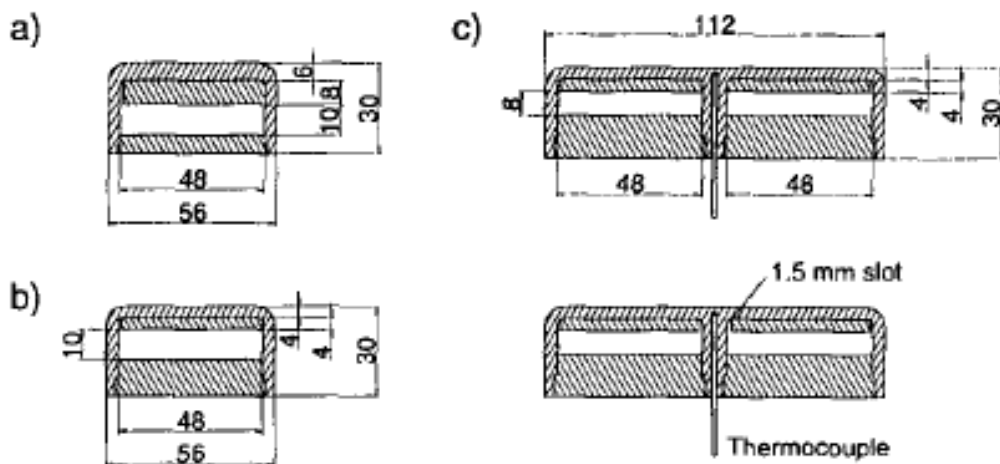


Fig 18 : Cross-sections of tested elements: a) standard JET Hypervapotron, b) new Box Scraper Hypervapotron und c) Box Scraper element prototype [41].

The material used for the construction of the Hypervapotrons is CuCrZr, and it is also mentioned in the paper [41] that the front wall surface temperature should be below 450 C due to strength limitation of the CuCrZr material. Figure 19 shows the maximum surface temperature rise (with respect to inlet temperature), as a function of power density, for various water flow velocities for the prototype element (figure 18 (c)). The data are very interesting as they cover a wide range of inlet velocities and heat fluxes, spanning different boiling regimes.

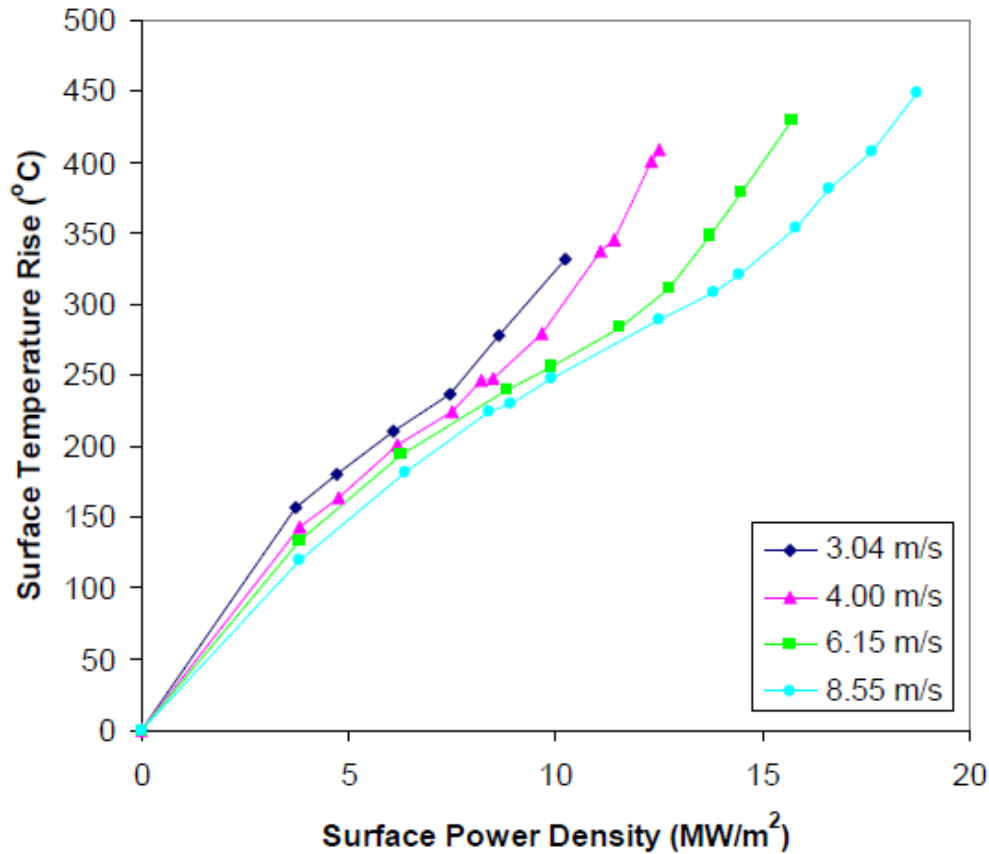


Fig 19: Boxscraper data showing the variation of the surface temperature with respect to the applied surface power density [19, 41]

### 2.2.2. MkI

MkI Hypervapotron tests report were presented by Altman et al [39] where the application of Hypervapotron is considered for JET NBI test bed. Figure 20 shows the typical Hypervapotron geometry along with the dimensions [39]. Figure 21 shows experimental data on the temperature variation with the heat flux collected during the experimental campaigns.

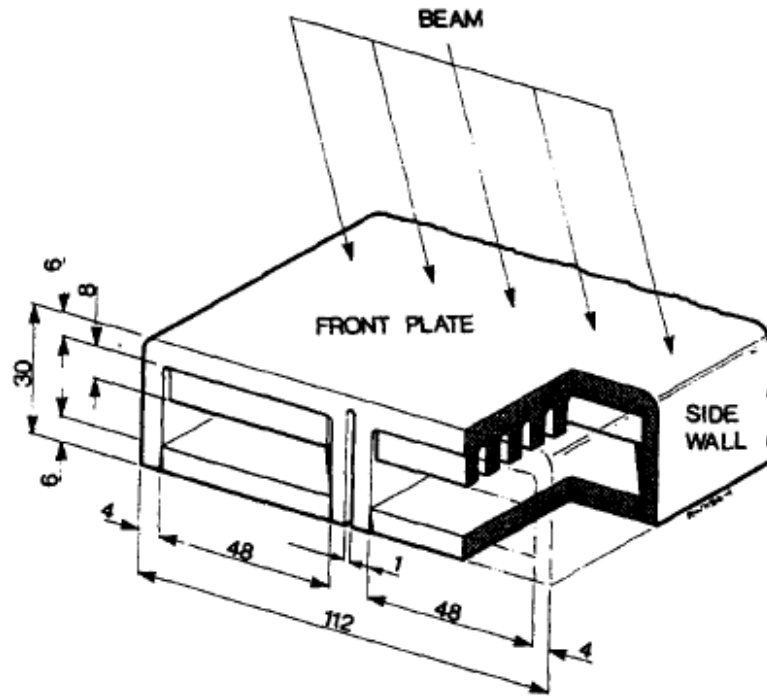


Fig 20: The modified MkI Hypervapotron with central slot [39]

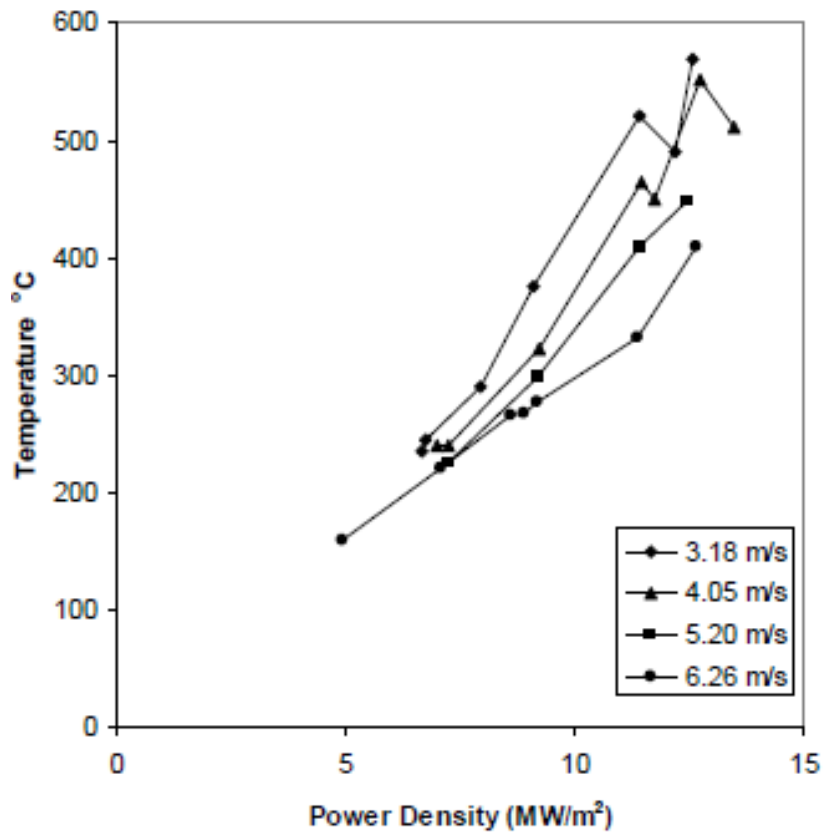


Fig 21: Variation of temperature with power density for the modified MkI Hypervapotron [39]

### 2.2.3. Div 4×3 and Div 6×6

The data for Div 4×3 and Div 6×6 comes from JET Divisional Notes [36, 40]. These reports are aimed at the potential application of Hypervapotrons for the JET Divertor.

Figure 22 shows the geometries tested by Falter et al [36],

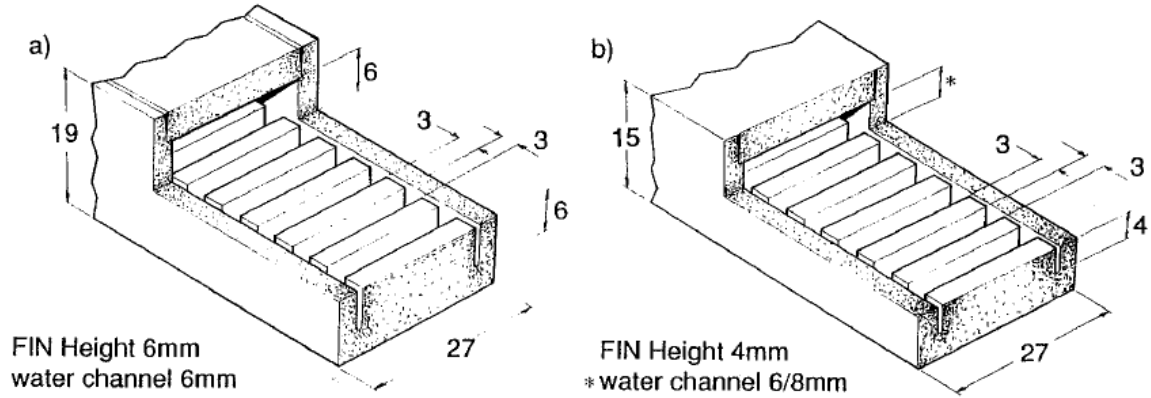


Fig 22: Hypervapotron designs tested by Falter et al [39]

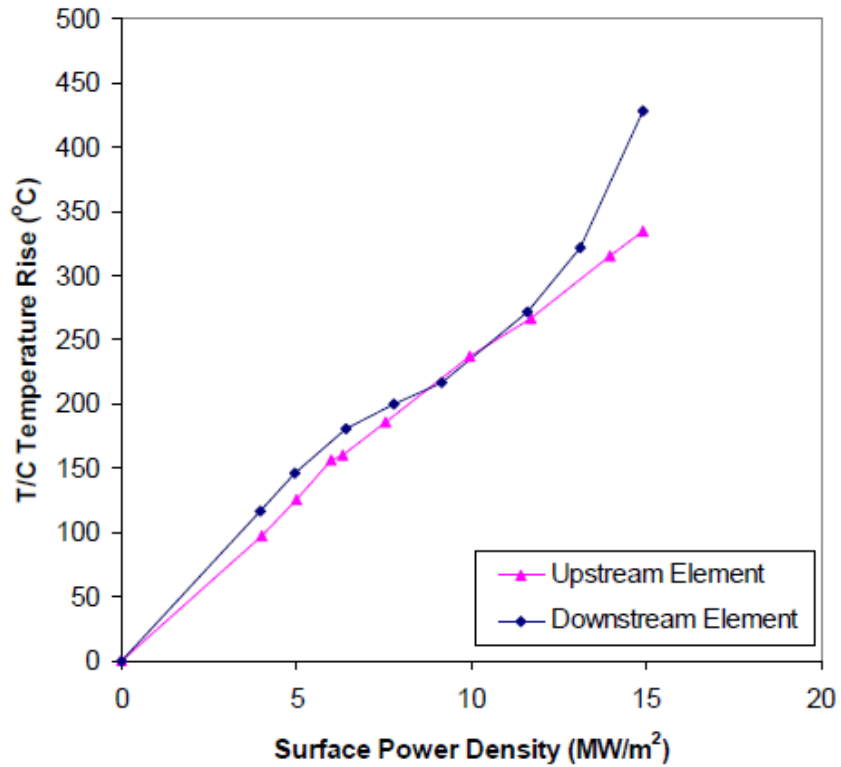


Fig 23: Div 6×6mm experimental data used in this thesis [19]

Figure 23 shows experimental data for case a) in figure 22 for Div 6×6, where data are plotted for surface temperature rise against the surface heat flux for the upstream and downstream elements (In the experimental apparatus there are two hypervapotron elements through which the coolant flows in series).

Massmann [40] subsequently performed a similar set of tests but these were restricted to a single geometry, specifically based on a 4mm fin and 3mm channel (It is called Div 4×3). Figure 24 shows the experimental data for Div 4×3 geometry, where for the data plotted represent the surface temperature rise against the surface heat flux for different inlet conditions.

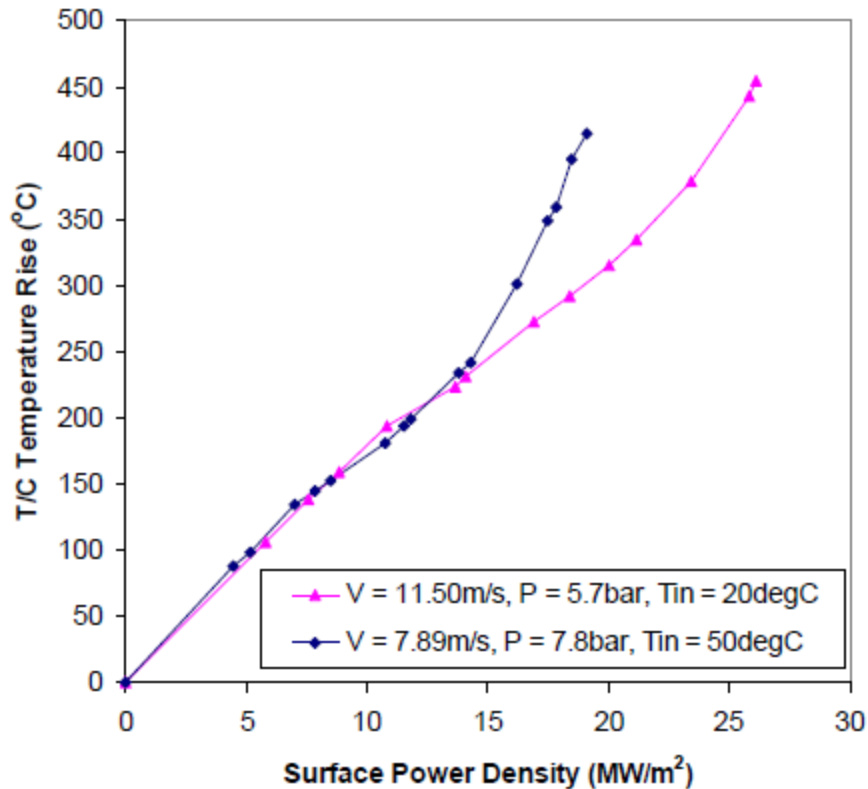


Fig 24: Div 4×3mm experimental used in this thesis [19]

The data collected from J. Milnes (which itself is taken from JET experiments), and used in this thesis show the appearance of three different boiling regions. For example see figure 25 where the data for Div 4×3 mm are discussed.

The experimental data can be divided into three regimes the first regime where the slope of the boiling curve is constant denotes no boiling (~till 6MW/m<sup>2</sup> for inlet velocity of 7.89 m/s) where heat transfer occurs only due to single phase forced convection flow. As we increase the heat flux the slope of the curve decreases (which is due to increase in the heat transfer coefficient due to nucleate boiling) and soft boiling starts (in the range 6-15 MW/m<sup>2</sup>). If we further increase

the heat flux hard boiling region starts ( approx.  $>15 \text{ MW/m}^2$ ) where we again observe change in slope ( increase in slope) due to more bubble formation and possibility of vapor blanketing, causing reduced heat transfer coefficient [36].

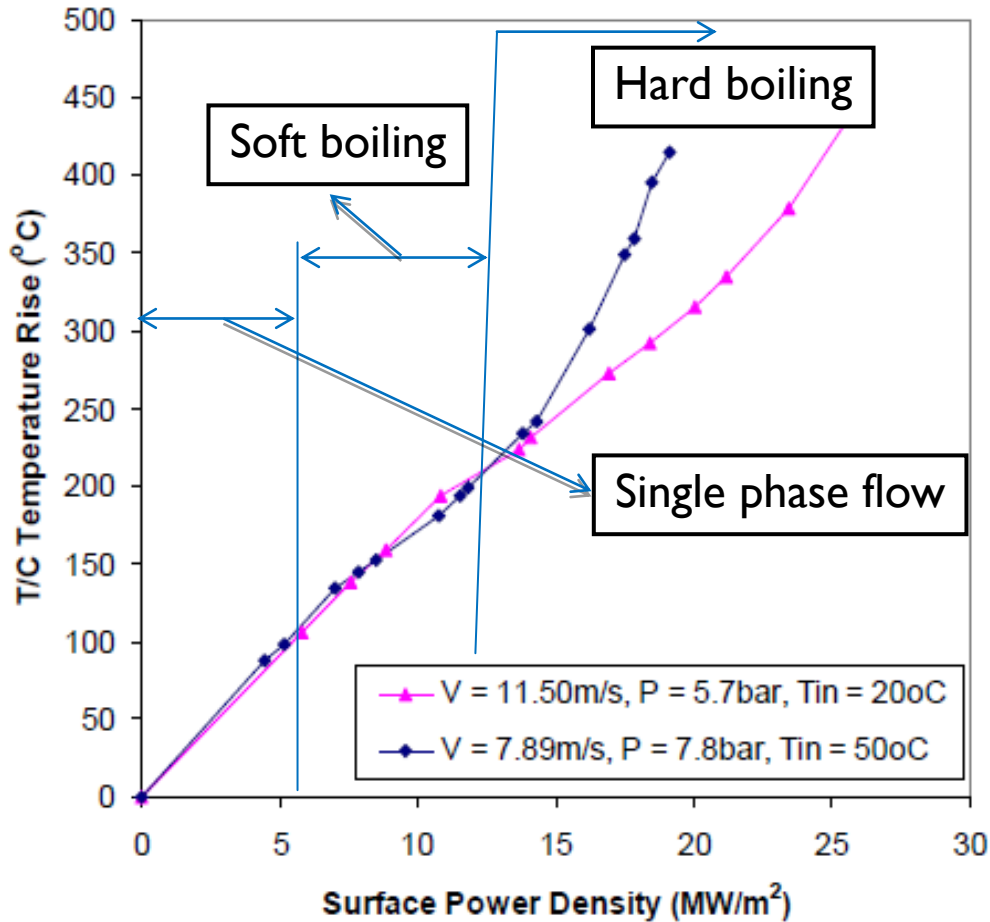


Fig 25: Experimental data of Div 4×3 mm showing different boiling regimes (the transition between different regimes is located for the case  $V_{in} = 7.89 \text{ m/s}$ ).

In a nutshell whenever there is a change in the boiling regime we always observe a change in slope in the experimental data, which is the qualitative feature of the inherent physics.



# 3. Models Description

To solve the flow problem numerically in either single phase or multiphase, first of all we need the governing equations which have the inherent physics embedded in them. The problem being dealt with in this thesis includes complex physics such as turbulence and subcooled boiling, so along with solving the equations of mass, momentum, and energy we also need some sub models to represent turbulence and near wall sub cooled boiling.

This chapter briefly describes the governing equations used for solving the fluid flow, both in single phase and multiphase flow and then the turbulence and boiling submodels used are described.

## 3.1. Introduction

There is a bunch of CFD codes available, both free and commercial [42], though not all of them have the capabilities of solving multiphase flow problems including subcooled boiling. Among the available softwares, some are fairly established and have been extensively validated, such as ANSYS-CFX, ANSYS-FLUENT, STARCD and STARCCM+.

In chapter 1 it was discussed that the authors in the recent past have used several tools to do the subcooled boiling modeling of Hypervapotron. For this thesis two such tools are used, namely ANSYS-FLUENT 13 [43] and STAR-CCM+7.02 [44], and using these tools 4 boiling models are tested,

1. Rensselaer Polytechnic Institute model (RPI model) using ANSYS FLUENT 13
2. Bergles and Rohsenow model (BR model), developed as an UDF in ANSYS FLUENT
3. Rohsenow boiling model using STARCCM+ 7.02
4. Transition boiling model using STARCCM+ 7.02

ANSYS [45] is a fairly established commercial tool solving problems related to multi-physics, Electromagnetics, Fluid dynamics and structural mechanics. ANSYS has two different widely used fluid dynamic analysis tools: ANSYS-FLUENT [43] and ANSYS-CFX [46]. Both of these have the capability of solving multiphase flows including subcooled boiling, but among these ANSYS-FLUENT-13 beta is chosen for our two phase flow analysis because it contains RPI model for solving nucleate boiling and it includes a Critical Heat flux Model to simulate the heat transfer near the critical heat flux region [47].

STAR-CCM+ has different boiling models implemented for a complete two phase flow analysis. The first one is the Rohsenow boiling model [4] and the second is Transition boiling model [4]. Both these models are capable of solving nucleate as well as hard boiling regions. The Transition boiling model is an improved version of the Rohsenow one. To tackle the regimes of boiling after nucleate boiling Rohsenow and Transition boiling model adopts different strategies which can be found in [4].

We implemented the BR model as an UDF in the commercial code ANSYS-FLUENT, and used it to test its applicability to the Hypervapotron, details about this model are given in section 3.3.2. Being a single phase model, it can potentially allow saving a substantial amount of CPU time, if compared to multiphase models, provided it is employed inside its applicability limits.

In this thesis the Eulerian approach is followed (RPI, Rohsenow, Transition boiling models), though alternative approaches exist, for details the reader is encouraged to consult the literature [4, 47- 52]. In the following sections the details of the equations solved are provided.

## 3.2. Governing Equations

### 3.2.1. Single phase flow

The governing equations to solve single phase fluid flow are shown below, which are partial differential equations that represent conservation of mass momentum and energy.

Conservation of mass

$$\frac{\partial \rho}{\partial t} + \nabla \cdot (\rho \vec{V}) = 0 \quad 3.1$$

Where  $\vec{V}$  is velocity vector and  $\rho$  is density.

Conservation of momentum

$$\frac{\partial(\rho \vec{V})}{\partial t} + \nabla \cdot (\rho \vec{V} \vec{V}) = -\nabla p + \nabla \cdot (\vec{\bar{\tau}}) + \rho \vec{g} \quad 3.2$$

Where  $p$  is the static pressure,  $\vec{g}$  is the gravitational vector,  $\vec{\bar{\tau}}$  is the stress tensor

Conservation of energy

$$\frac{\partial(\rho h)}{\partial t} + \nabla \cdot (\rho h \vec{V}) = \frac{\partial p}{\partial t} + \nabla \cdot (k_t \nabla T) + (\vec{\tau} \cdot \nabla) \vec{V} + S_h \quad 3.3$$

Where  $h$  is specific enthalpy,  $S_h$  is source of enthalpy and  $k_t$  is thermal conductivity.

### 3.2.2. Multiphase flow

In this section the multiphase approach used for this thesis are discussed. To solve the governing equations for mass, momentum and energy two different numerical models are used where, the first model is ‘The Eulerian Model’ (Inhomogeneous Multiphase flow model) as in ANSYS-FLUENT [47] and the second is ‘Volume Of Fluid (VOF) model’ (Homogeneous Multiphase flow model) as in STAR-CCM+ [4].

#### 3.2.2.1. The Eulerian Model

This model was used to perform boiling simulations using the commercial CFD code ANSYS FLUENT. This is a very complex model and solves the full set of momentum and continuity equation for each phase, with a single pressure shared by all phases. The different fluids interact via interphase transfer terms. For example, two phases may have separate velocity and temperature fields, but there will be a tendency for these to come to equilibrium through interphase drag and heat transfer terms. The governing equations which are solved in this model are shown below along with the interphase exchange terms [53],

Conservation of mass

$$\left( \frac{\partial}{\partial t} (\alpha_q \rho_q) + \nabla \cdot (\alpha_q \rho_q \vec{V}_q) \right) = \sum_{p=1}^n (\dot{m}_{pq}), \quad q = 1, \dots, n \quad 3.4$$

Where  $\vec{V}_q$  is the velocity vector,  $\rho_q$  is the density and  $\alpha_q$  is the volume fraction of phase  $q$ ,  $\dot{m}_{pq}$  denotes the mass transfer from phase  $p$  to  $q$ .

Conservation of momentum

$$\left( \frac{\partial}{\partial t} (\alpha_q \rho_q \vec{V}_q) + \nabla \cdot (\alpha_q \rho_q \vec{V}_q \vec{V}_q) \right) = -\alpha_q \nabla p + \nabla \cdot \vec{\tau}_q + \alpha_q \rho_q \vec{g} + \sum_{p=1}^n (\vec{R}_{pq} + \dot{m}_{pq} \vec{V}_{pq}) + (\vec{F}_q + \vec{F}_{lift,q} + \vec{F}_{vm,q}), \quad q = 1, \dots, n \quad 3.5$$

$$\text{And } \bar{\bar{\tau}}_q = \alpha_q \mu_q (\nabla \bar{V}_q + \nabla \bar{V}_q^T) + \alpha_q \left( \lambda_q - \frac{2}{3} \mu_q \right) \nabla \cdot \bar{V}_q \bar{I} \quad 3.6$$

Here  $p$  is the pressure shared by all phases  $\bar{\bar{\tau}}_q$  is  $q^{\text{th}}$  phase stress tensor,  $R_{pq}$  is the interfacial drag force,  $\bar{F}_q$ ,  $\bar{F}_{\text{lift},q}$  and  $\bar{F}_{\text{vm},q}$  are external body force, lift force (acts on bubbles mainly due to velocity gradients in primary phase flow field [47]) and virtual mass force (force exerted by the inertia of the primary phase mass encountered by the accelerating bubbles [47]) respectively,  $\bar{V}_{pq}$  is interphase velocity: if  $\dot{m}_{pq} > 0$  then  $\bar{V}_{pq} = \bar{V}_p$ , similarly if  $\dot{m}_{qp} > 0$  then  $\bar{V}_{qp} = \bar{V}_q$ .

Conservation of energy

$$\left( \frac{\partial}{\partial t} (\alpha_q \rho_q h_q) + \nabla \cdot (\alpha_q \rho_q \bar{V}_q h_q) \right) = \alpha_q \frac{\partial p}{\partial t} + \bar{\bar{\tau}}_q : \nabla \bar{V}_q - \nabla \cdot q_q + \quad 3.7$$

$$S_q + \sum_{p=1}^n (\mathcal{Q}_{pq} + \dot{m}_{pq} h_{pq}), \quad q = 1, \dots, n$$

Here  $h_q$  denotes specific enthalpy of  $q^{\text{th}}$  phase  $q_q$  is heat flux,  $S_q$  is source term,  $\mathcal{Q}_{pq}$  is intensity of heat exchange and  $h_{pq}$  is the difference in the formation enthalpies of phases  $p$  and  $q$ .

Finally the sum of all volume fractions must be equal to 1

$$\sum_{q=1}^n \alpha_q = 1 \quad 3.8$$

The following are the are restrictions on interfacial mass momentum and energy exchange terms

The rate of vapor formation per unit time is given by

$$\dot{m}_{lv} = [h_{ls} (T_l - T_{sat}) + h_{vs} (T_v - T_{sat})] \frac{A_i}{L} + \frac{q_E'' A_w}{(L + C_{pl} (T_{sat} - T_l))} \quad 3.9$$

The subscript  $l$ ,  $v$ ,  $sat$  stands for liquid vapor and saturation states respectively,  $C_{pl}$  is specific heat of liquid,  $h_{ls}$  is liquid side interfacial heat transfer coefficient, which is calculated using Ranz-Marshall coefficient [47]

$$h_{ls} = \frac{k_l}{D_b} \left( 2 + 0.6 \text{Re}^{0.5} \text{Pr}^{0.33} \right) \quad 3.10$$

And the interfacial area density is given by  $A_i = 6\alpha_{sv}(1 - \alpha_v)/D_b$  3.11

Here  $\alpha_{sv}$  is  $\min(\alpha_v, 0.25)$ ,  $k_l$  is liquid thermal conductivity,  $h_{vs}=105 \text{ W/m}^3/\text{K}$  which is vapor side interfacial heat transfer coefficient, which comes from the assumption that vapor temperature is close to saturation temperature and  $q_E''$  is the evaporative heat flux.

$L$  is the latent heat per unit mass,  $A_w$  is the interfacial area density at the wall surface and  $D_b$  is bubble diameter.

$$\vec{R}_{pq} = 0.75 C_d \rho_l \alpha_v \cdot |\vec{V}_l - \vec{V}_v| \cdot |\vec{V}_l - \vec{V}_v| / D_b \quad 3.12$$

Where the drag coefficient is determined by choosing the minimum of viscous regime and distorted regime (which is characterized by a vortex system developing behind the bubble, where the vortex departure creates a large wake region distorting the bubble itself and the following bubbles [54]):  $C_d = \min(C_d^{dis}, C_d^{vis})$

$$C_d^{vis} = \frac{24}{\text{Re}_b} (1 + 0.1 \text{Re}_b^{0.75}) (\max(\alpha_l, 0.5))^{-2} \quad 3.13$$

$$C_d^{dis} = \frac{2D_b}{3} (g(\rho_l - \rho_v)/\sigma)^{1/2} \cdot (\max(\alpha_l, 0.5))^{-1}$$

The lift force acting on the secondary phase ‘p’ due to the primary phase ‘q’ can be calculated using the formula

$$\vec{F}_{lift,q} = -C_l \rho_q \alpha_p (\vec{V}_q - \vec{V}_p) \times (\nabla \times \vec{V}_q) \quad 3.14$$

Here  $C_l$  is the lift coefficient

The lift coefficient is calculated following Moraga et al [55]

$$C_l = \begin{cases} 0.0767, & \phi \leq 6000 \\ -\left(0.12 - 0.2e^{-\phi/36000}\right) e^{\phi/3e^7}, & 6000 \leq \phi \leq 1.9e^5 \\ -0.002, & \phi \geq 1.9e^5 \end{cases} \quad 3.15$$

Here  $\phi = Re_b Re_v$  and  $Re_b = \frac{D_b |\vec{V}_l - \vec{V}_v|}{\nu_l}$  which is bubble Reynolds number and

$Re_v$  which is bubble shear Reynolds number is given by  $Re_v = \frac{D_b^2 |\nabla \times \vec{V}_l|}{\nu_l}$

### 3.2.2.2. Volume of Fluid model

This model was used to perform boiling simulations with the commercial CFD code STAR-CCM+, the VOF model could track the interface between two phases and it has been used widely in analyzing various two phase flow systems. In this model the governing equations are solved using the volume fraction in each cell. The equations solved in this model are given below

Continuity equation for volume fraction

$$\left( \frac{\partial}{\partial t} (\alpha_q \rho_q) + \nabla \cdot (\alpha_q \rho_q \vec{V}_q) \right) = S_\alpha \quad 3.16$$

Here  $S_\alpha$  is mass source term.

Momentum equation

$$\frac{\partial(\rho \vec{V})}{\partial t} + \nabla \cdot (\rho \vec{V} \vec{V}) = -\nabla p + \nabla \cdot (\bar{\tau}) + \rho \vec{g} + \vec{F} \quad 3.17$$

Where  $\vec{V}$  is a mass averaged velocity

$$\vec{V} = \frac{\alpha_l \rho_l \vec{V}_l + \alpha_v \rho_v \vec{V}_v}{\rho} \quad 3.18$$

Energy equation

$$\frac{\partial(\rho h)}{\partial t} + \nabla \cdot (\rho h \vec{V}) = \frac{\partial p}{\partial t} + \nabla \cdot (k_t \nabla T) + (\bar{\tau} \cdot \nabla) \vec{V} + S_h \quad 3.19$$

Here Enthalpy and Temperature are also mass averaged variables

The above shown governing equations are solved for vapor, water and for inter interfaces, using the following mixture density and viscosity and other physical properties shown in 3.20 [56].

$$\begin{aligned}
 \rho &= \sum_i \rho_i \alpha_i \\
 \mu &= \sum_i \mu_i \alpha_i \\
 C_p &= \sum_i (C_p)_i \alpha_i \rho_i / \rho
 \end{aligned}
 \tag{3.20}$$

### 3.3. Boiling models

There are several correlations proposed by many authors [57- 62] in the past to depict boiling, and the reader is encouraged to visit the relevant references for an exhaustive list and analysis. In this section the boiling models used for predicting the Hypervapotron thermal performance in this thesis are explained in detail.

#### 3.3.1. RPI model

This model was developed by Kurul and Podowski [62]; according to this model the wall heat flux is partitioned as

$$\begin{aligned}
 q_w'' &= q_L'' + q_Q'' + q_E'' \\
 q_L'' &= \text{liquid convective heatflux} \\
 q_Q'' &= \text{quenching heatflux} \\
 q_E'' &= \text{evaporative heatflux}
 \end{aligned}
 \tag{3.21}$$

Quenching heat flux is transferred to liquid when subcooled liquid fills the space near the heated wall vacated by a departing bubble.

The wall surface is divided in a fraction  $\Omega$ , covered by nucleating bubbles and  $(1 - \Omega)$  covered by liquid. The formula for calculating the convective heat flux is given below

$$q_L'' = h_{lw} \cdot (T_w - T_l) \cdot (1 - \Omega)
 \tag{3.22}$$

Where  $h_{lw}$  is single phase heat transfer coefficient, the quenching heat flux can be calculated as

$$\dot{q}_Q'' = 2.\Pi^{-0.5}.\Omega.(f.k_l.\rho_l.C_{pl})^{0.5}(T_w - T_l)$$

$f$  = bubble departure frequency

$k_l$  = Thermal conductivity of liquid

$C_{pl}$  = specific heat of liquid

$\rho_l$  = density of liquid

3.23

Bubble departure frequency is given as

$$f = \sqrt{\left(\frac{4.g.(\rho_l - \rho_v)}{3.d_{vw}.\rho_l}\right)}$$

3.24

Evaporative heat flux is calculated as

$$\dot{q}_E'' = \frac{\Pi}{6}.d_{vw}^3.f.n.\rho_v.L$$

$d_{vw}$  = bubble departure diameter

$n$  = nucleation site density

$L$  = latent heat

3.25

Where

$$n = 200.(T_w - T_{sat})^{1.8}$$

3.26

### 3.3.2. BR model

This model was developed by Bergles and Rohsenow [3]. They suggested that subcooled boiling heat transfer may be described by:

$$q_{total} = (q_{FC}^2 + (q_{FDB} - q_0)^2)^{1/2}$$

3.27

where  $q_{FC}$  and  $q_{FDB}$  are the forced convection and fully developed boiling heat flux, and  $q_0$  is the flux at the onset of nucleate boiling. The boiling curve predicted by figure 26 merges smoothly with the forced convection curve for  $q_{FDB} = q_0$ , and approximates accurately the fully developed curve for  $q_{FDB} \gg q_{FC}, q_0$ .  $q_{FC}$  is given by the single-phase wall heat transfer model for which we used the Dittus-Boelter equation

$$Nu = 0.023Re^{0.8} Pr^{0.4}$$

3.28



Where  $Nu$  is the Nusselt number, and  $Re$  and  $Pr$  are the Reynolds and Prandtl number, respectively.

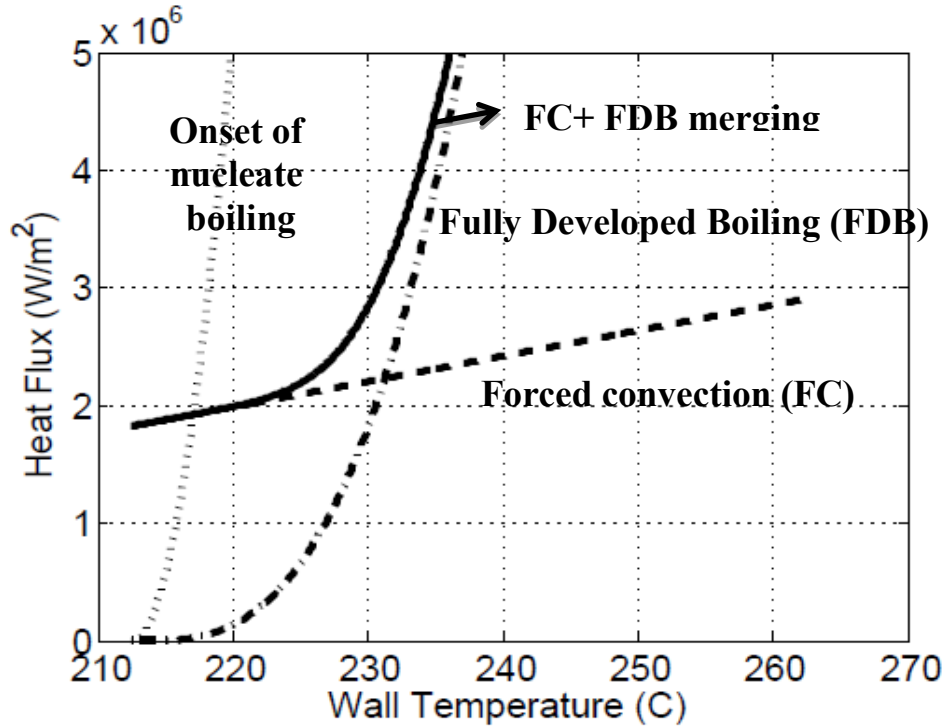


Fig. 26: Forced convection (dashed), onset of nucleate boiling (dotted), fully developed boiling (dash-dotted) heat fluxes, together with the BR merging (solid). Data are for the operating pressure of 20 bar.

$q_{FDB}$  is given by

$$q_{FDB} = ((T_w - T_{sat})/C_s)^3 \quad 3.29$$

where  $C_s$  is a free parameter. In principle, also the exponent in above equation must be input by the user. However, the value 3 is strongly recommended [3].

$q_0$  is given by the following formula,

$$q_o = \left( \frac{k_l h_{fg} \rho_v}{8\sigma T_{sat}} \right) (T_{w,o} - T_{sat})^2 \quad 3.30$$

Where  $k_l$  is the liquid thermal conductivity,  $h_{fg}$  is the latent heat of vaporization,  $\sigma$  is the liquid surface tension,  $T_{w,o}$ , is the wall temperature at onset of nucleate boiling, a discussion about this can be found in [32].

### 3.3.3. Rohsenow model

This model is implemented in the commercial CFD code STARCCM+, in this model a correlation proposed by Rohsenow [58] is used for nucleate boiling regime and a film boiling model [4] is also integrated into the Rohsenow implementation. This film boiling model will not turn on until the volume fraction of vapor exceeds a particular value of  $\alpha_{fb}$  which is one of the user input parameter.

The following formula shows the wall heat flux due to boiling given by Rohsenow

$$q_{bw} = \mu_l * h_{lat} * \sqrt{\frac{g(\rho_l - \rho_v)}{\sigma}} \left( \frac{C_{pl}(T_w - T_{sat})}{C_{qw} h_{lat} Pr_l^{n_p}} \right)^{3.03} \quad 3.31$$

where  $\mu_l$  is the liquid viscosity,  $C_{pl}$  the liquid specific heat,  $h_{lat}$  the latent heat,  $Pr_l$  the liquid Prandtl number,  $\rho_{l(v)}$  the liquid (vapor) density,  $T_{w(sat)}$  the wall (saturation) temperature,  $\sigma$  the surface tension,  $g$  gravity acceleration,  $n_p$  is the Prandtl number exponent and  $C_{qw}$  a constant dependent on the liquid/surface combination. The vapor mass generation rate is given by

$$\dot{m}_{ew} = \frac{C_{ew} q_{bw}}{h_{lat}} \quad 3.32$$

where  $C_{ew}$  is the heat flux fraction used to create vapor bubbles. The rate of evaporation and condensation is calculated using the formula

$$\dot{m}_{ec} = \frac{C_{HTCxArea} \cdot (T - T_{sat})}{h_{lat}} \quad 3.33$$

where  $C_{HTCxArea}$  ( $W/m^3K$ ) is the HTC between a bubble and the surrounding liquid times the contact area per unit volume, and  $T$  is the temperature of the mixture.

The film boiling model, used in a combination with the VOF multiphase model, assumes that the film thickness is resolved in one or more cells (one or more cells close to the heated wall are occupied by the vapor); in which case the expressions for the wall heat flux are the same as in the case of single phase flows. As this model is implemented using VOF approach, the same is used to track the liquid vapor interface in the film boiling regime. Switching between nucleate and film boiling is tuned by a critical value of the vapor fraction, called  $\alpha_{fb}$ .

An additional tunable parameter is the turbulent Schmidt number  $S_{ct}$ , the ratio of eddy viscosity to eddy mass diffusivity [4]. Overall, there are six user provided input parameters. All

these parameters have to be tuned for a particular geometry based on the available experimental data.

If the Rohsenow correlation is applied outside its range of applicability (for example, to the film boiling regime), unrealistically high heat fluxes could result, with fluid temperatures becoming higher than the near wall temperature. This behavior stems from the fact that the Rohsenow correlation does not depend on the fluid temperature; heat will enter the domain irrespective of the fluid temperature. To prevent this condition, the heat flux calculated by the correlation is multiplied by:

$$\max \left[ 0, \min \left( \left( \frac{T_w - T}{T_w - T_{sat}} \right), 1 \right) \right] \quad 3.34$$

where T is fluid temperature near heated wall.

### 3.3.4 Transition boiling model

This model also exists in the commercial CFD code STARCCM+. The model is based on the VOF approach and has added the necessary capabilities to deal with simulation of boiling in the most practical and reliable form. The nucleate boiling regime in the transition model is more general than the Rohsenow model. While the Rohsenow correlation is restricted to be proportional to  $\Delta T^{3.03}$  in the nucleate boiling regime the transition model allows for the user to specify the power  $k_1$  in the expression  $\Delta T^{k_1}$ .

This model adopts different correlation for the 3 regions shown in figure 27, trying to accurately capture the nucleate and the 2 transition regions:

Referring to the figure 27, the correlations in the 3 regions are as follows:

$$q_{boiling}(\Delta T) = q_{max} S \phi \left( \frac{\Delta T}{\Delta T_1} \right)^{k_1} \quad 0 \leq \Delta T \leq \Delta T_1 \quad 3.35$$

$$q_{boiling}(\Delta T) = q_{max} S \left( 1 - 4(1 - \phi) \left( \frac{\Delta T - \Delta T_{max}}{\Delta T_2 - \Delta T_1} \right)^2 \right) \quad \Delta T_1 \leq \Delta T \leq \Delta T_2 \quad 3.36$$

$$q_{boiling}(\Delta T) = q_{max} S \phi \left( \frac{\Delta T - \Delta T_1}{\Delta T_2 - \Delta T_1} \right)^{-k_2} \quad \Delta T_2 \leq \Delta T \quad 3.37$$

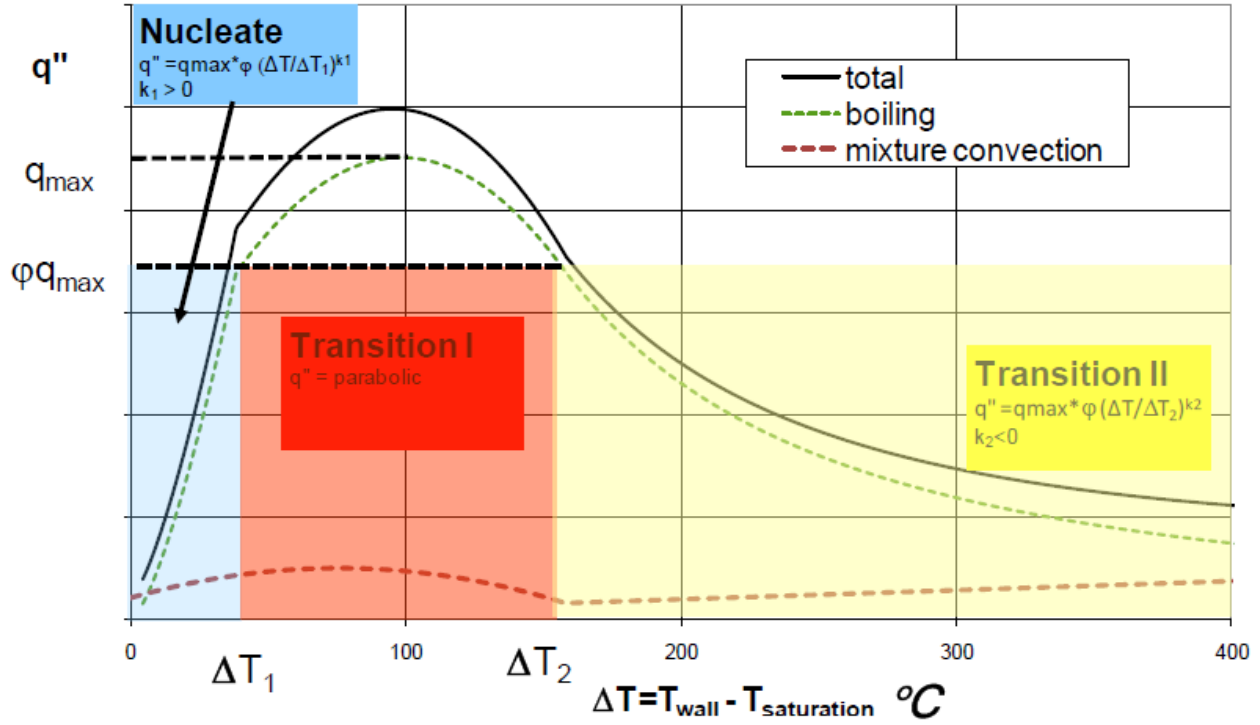


Fig 27: Heat flux vs Excess temperature [4]

Where  $q_{\text{max}}$ ,  $k_1$ ,  $k_2$ ,  $\Delta T_1$ ,  $\Delta T_2$ , are constants in the model which are all positive,  $\Delta T_2$  should be always greater than  $\Delta T_1$ , and  $S$  allows the user to scale  $q_{\text{max}}$  up or down for a given boundary.  $\phi$  is set equal to 0.75. All these constants are application specific and have to be tuned for a particular geometry based on the available experimental data.

In this model, the total heat flux at the wall is a sum of the heat fluxes due to boiling, convection and thermal radiation. In the above equations,  $q_{\text{max}}$  is the maximum of the boiling heat flux component and it is not the critical heat flux which is a maximum of the total heat flux. The effect of radiation heat transfer is most commonly not modeled directly but included in the boiling model constants. The boiling heat flux contribution to the total heat flux is considered to be zero when there is no liquid to boil in any cell adjacent to the wall. The remaining correlations adopted are the same as that of the Rohsenow boiling model.

### 3.4. Turbulence model

Turbulence modeling is necessary because it is difficult to afford big enough computers to directly capture every scale of motion. And it is always required to find a steady-state solution (with all the unsteady fluctuations averaged out) rather than a detailed time-accurate one that captures every little vortex. As a result, there are unsteady turbulent motions affecting the flow that cannot be resolved directly; they must therefore be modeled. In some cases, the turbulence

model used can have a huge effect on the results that are obtained using CFD, this kind of disparity in solution obtained is largely due to the fact that no model is right all the time; they all have their limitations. Because of this, there are dozens of variations available, and more are being developed all the time. At the end the choice comes down to two methods currently available within most CFD solvers:

1. Reynolds Averaged Navier Stokes (RANS)
2. Large Eddy Simulations (LES)

There are several methods within these categories, they are further broken down by the number of additional transport equations which one must solve in order to compute the model contributions [4, 47 and 63]. The ultimate objective of this study is to use the CFD model for predicting the thermal performance of Hypervapotron, the field of turbulence is in itself very large and cumbersome, which is out of the scope of this thesis to test all the available models and fine tune them for the specific geometry. So after sorting out the literature [4, 27-33, 47, 63-65], it is found that RANS approach is good enough because these are the models that are used for most production applications. In specific for this thesis an improvement of K-Epsilon model called the Realizable K-Epsilon Model is used.

The realizable K-Epsilon Model was developed by Shish et al [4], this model contains a new transport equation for the turbulent dissipation rate, the realizable K-Epsilon model is substantially better than the standard K-Epsilon model for many applications, and can generally be relied upon to give answers that are at least as accurate [4].

In this model the turbulent kinetic energy  $k$  and turbulent dissipation rate  $\varepsilon$  are calculated using the following formulas

Equation for calculating turbulent kinetic energy

$$\frac{d}{dt} \int_V \rho k dV + \int_A \rho k (v) \cdot da = \int_A \left( \mu + \frac{\mu_t}{\sigma_k} \right) \nabla k \cdot da + \int_V [G_k + G_b - \rho((\varepsilon - \varepsilon_0) + \gamma_M) + S_k] dV \quad 3.38$$

Equation for calculating turbulent dissipation rate

$$\begin{aligned} \frac{d}{dt} \int_V \rho \cdot \varepsilon \cdot dV + \int_A \rho \varepsilon (v) \cdot da = \int_A \left( \mu + \frac{\mu_t}{\sigma_\varepsilon} \right) \nabla \varepsilon \cdot da \\ + \int_V \left[ C_{\varepsilon 1} S \varepsilon + \frac{\varepsilon}{k} (C_{\varepsilon 1} C_{\varepsilon 3} G_b) - \frac{\varepsilon}{k + \sqrt{\nu \varepsilon}} C_{\varepsilon 2} \rho \varepsilon + S_\varepsilon \right] dV \end{aligned} \quad 3.39$$

where  $S_k$  and  $S_\varepsilon$  are the user-specified source terms,

The turbulent production is calculated as

$$\begin{aligned} G_k = \mu_t S^2 - \frac{2}{3} \rho k \nabla \cdot v - \frac{2}{3} \mu_t (\nabla \cdot v)^2 \\ \nabla \cdot v = \text{velocity divergence} \\ S = |\tau_s| = \text{modulus of mean strain rate tensor} \\ S = \sqrt{2 \tau_s : \tau_s^T} = \sqrt{2 \tau_s} \\ \tau_s = \frac{1}{2} (\nabla v + \nabla v^T) \end{aligned} \quad 3.40$$

The Buoyancy production is calculated as

$$G_b = \beta \frac{\mu_t}{\sigma_t} (\nabla T \cdot g) \quad 3.41$$

$\beta$  = coefficient of thermal expansion

$g$  = gravitational vector

$\nabla T$  = temperature gradient vector

$\sigma_t$  = turbulent prandtl number

The Compressibility Modification is given by

$$\begin{aligned} \gamma_M = \frac{C_M k \varepsilon}{c_s^2} \\ C_M = 2 \\ c_s = \text{speed of sound} \end{aligned} \quad 3.42$$

The turbulent viscosity is given by

$$\mu_t = \rho C_\mu \frac{k^2}{\varepsilon} \quad 3.43$$

Here  $C_\mu$  is no longer constant as with the standard K-Epsilon model.

$$C_\mu = \frac{1}{A_0 + A_s U^{(*)} \frac{k}{\varepsilon}} \quad 3.44$$

$$U^{(*)} = \sqrt{s : s - w : w}$$

$$A_s = \sqrt{6} \cos \phi$$

$$\phi = \frac{1}{3} a \cos(\sqrt{6}W)$$

$$W = \frac{s_{ij} s_{jk} s_{ki}}{S^3}$$

$$A_0 = 4.0$$

model constants

$$C_{\varepsilon 1} = \max\left(0.43, \frac{\eta}{\eta + 5}\right)$$

$$\eta = \frac{Sk}{\varepsilon}$$

$$C_{\varepsilon 2} = 1.9$$

$$\sigma_k = 1.0$$

$$\sigma_\varepsilon = 1.2$$

In STARCCM+ it is suggested that for this turbulence model the high  $y+$  wall treatment (High Wall Treatment is essentially the classic wall-function approach [63] , where wall shear stress, turbulent production and turbulent dissipation are all derived from equilibrium turbulent boundary layer theory) is suitable, and it restricts the wall-cell centroid to be situated in the logarithmic region of the boundary layer ( $y+ > 30$  ), it is unlikely that significant error will result from  $y+$  values as low as 12 [4]. So this recommendation is followed in all the mesh generations that were performed for this thesis.

# 4. Computational results and comparison with experiments

The main objective of this chapter is to present the computational results obtained by running the simulations on both Flat Channel and Hypervapotron geometry, and then compare them with the available experimental data base. The operating regimes of interest cover single phase, nucleate and hard boiling regions.

As explained in chapter 2, the experiments conducted at Efremov includes also data on Flat channel, so before running the simulations on Hypervapotron some tests were conducted on Flat channel geometry which helps to test the boiling models on a simple geometry and then use them on the more complex Hypervapotron setup. The transition boiling model is the model which is applied only to the Hypervapotron geometry.

The problem comes when we have to set the free parameters in the model [for details- chapter 3, sections 3.3.3, 3.3.4], and try to match the available experimental data with the computer simulations for all the inlet conditions and heat fluxes, the parameters should be optimized in such a way that it can be reasonably applied to all cavity shapes with minimum error.

## 4.1 Flat Channel

In the following sections the results obtained using different boiling models on the Flat channel geometry are presented. We will first discuss the grid selection procedure and then the obtained results.

### 4.1.1 Grid generation and selection

A typical grid used for performing the simulations for this geometry, a non uniform structured hexahedral mesh, is shown in figure 28. For the Flat channel geometry, a number of hexahedral non uniform meshes created with the commercial mesh generator GAMBIT, all ranging from 0.3 to 1.7 Mcells. We found that the relative variation of the computed temperature (at the location of thermocouples) is ~12% (using the inlet subcooling as the reference value) when the mesh size varied from 0.3 to 1.0 Mcells. This variation was reduced to ~2% when the mesh size went from 1 to 1.7 Mcells. Then, ~1 Mcells are a good compromise between



reasonable grid-independence of the solution and computational cost. This size of the mesh is also comparable to that chosen in previously published works on the same subject [29, 32].

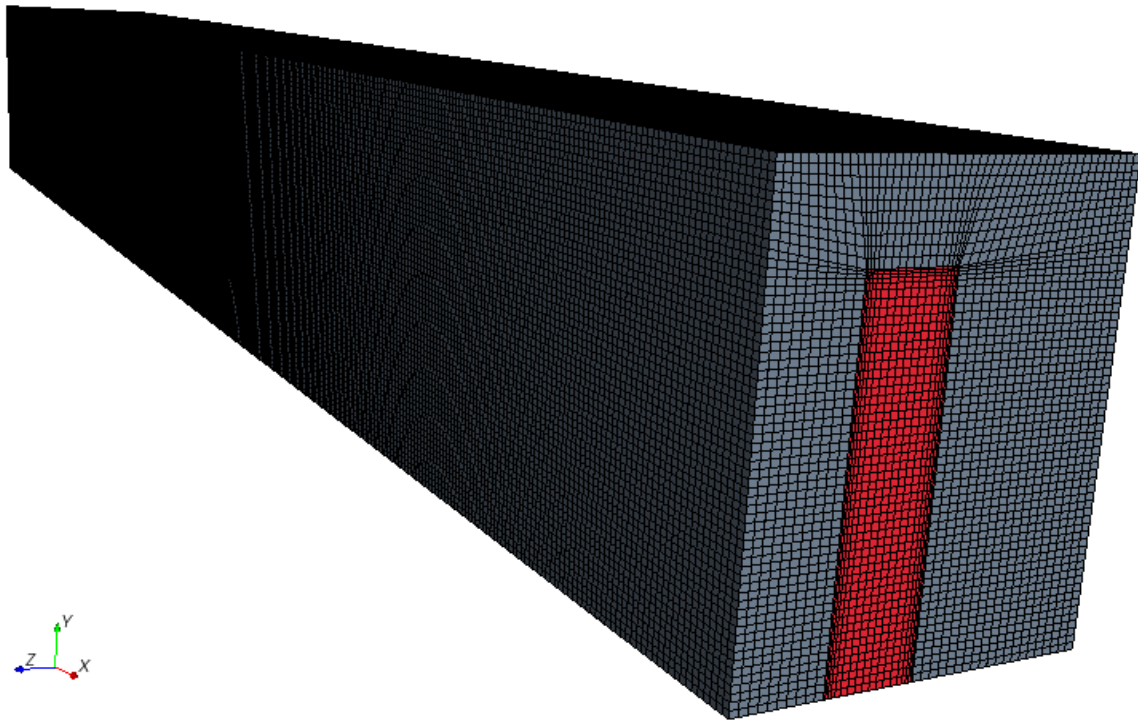


Fig 28: Mesh used for most of the computations for Flat channel.

#### 4.1.2 RPI Model

As explained in chapter 3 this boiling model is combined with the Eulerian approach to solve boiling problems. In section 3.2.2.1 the governing equations are discussed, along with the detailed set of relation for evaluating the interfacial transfer terms, in section 3.3.1 the details of the boiling model are presented.

Table 2 shows the other key settings used to perform the simulation, these settings are used to perform the simulations on the Flat channel geometry by using ANSYS FLUENT; the following strategy is adopted in order to get the solution faster

- First of all the computational domain is reduced; this is done by taking advantage of the symmetry in the geometry of the mockup along an axis parallel to the flow, which immediately reduces volume to be meshed to half of the original mockup.
- Secondly, to improve the convergence behavior an initial solution is computed by setting up an Eulerian model with above mentioned settings, but not solving the volume fraction equation(as suggested by ANSYS user guide). Once an initial solution is obtained the volume fraction equation is turned on and the full simulation is performed.

Table 2: Settings used to perform simulations using RPI model

<b>Setting</b>	<b>Modeling choice</b>
Inlet velocity profile	Uniform
Inlet temperature profile	Uniform
Inlet volume fraction	1e-15
Solver	Pressure based
Primary phase	liquid
Secondary phase	Vapor
Gravity	Included
Turbulence model	Realizable k- $\epsilon$ , (mixture model)
Wall boiling model	RPI model
Wall heat flux	Constant
Turbulent drift force	Included
Vapor bubble diameter	Sauter-mean
Drag	Ishii
Lift	Moraga
Interfacial heat transfer coefficient	Ranz-Marshall
Virtual mass force	Included
Inlet boundary condition	Velocity inlet

Outlet boundary condition	Pressure outlet
Boundary condition for turbulent kinetic energy (inlet & outlet)	Constant
Boundary condition for turbulent dissipation rate (inlet & outlet)	Constant

The mesh shown in figure 28 was imported in FLUENT; the proper settings have been applied as discussed above. The first simulations are done using an inlet velocity of 2 m/s and heat flux of 1 MW/m<sup>2</sup> (corresponding to a non-boiling case, as vapor formation is not observed from the simulations performed), the results obtained for the above inlet conditions are shown in figure 29.

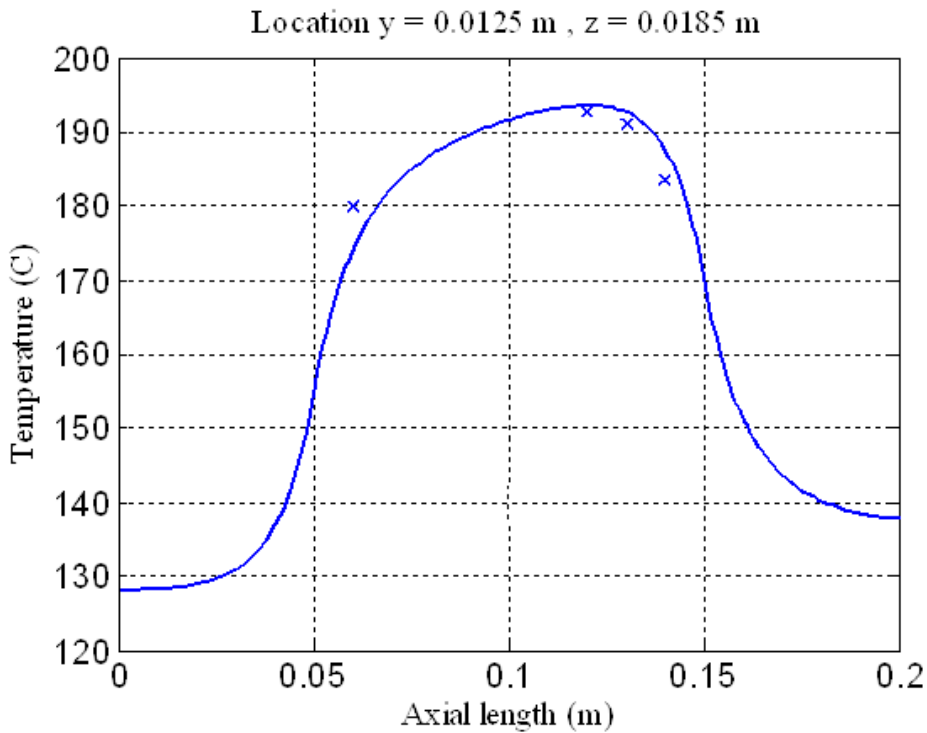


Fig 29: Comparison of temperatures simulated (solid), experimental (symbol) for input power of 1 MW/m<sup>2</sup> and inlet velocity 2m/s.

From the figure 29 it can be observed that for non boiling conditions this model was able to match the experimental data, with relative error < 5%. When the input heat flux was increased, it was found that whenever there was formation of vapor the model started diverging. In order to investigate the cause several tests were conducted, by changing the model user-defined constants

and the numerical relaxation parameters in the model, but the simulation never converged. The issue of robustness of the RPI model for one-side heated square ducts is now under investigation at ANSYS. As far as this thesis is concerned, this model was dropped at this point.

### 4.1.3 BR model

The details about this boiling model, which is coupled with a single-phase flow description, are explained in chapter 3, section 3.3.2. To predict the boiling phenomenon it uses an adhoc prescription of heat transfer coefficient due to subcooled boiling.

We implemented this model in the commercial CFD code FLUENT in the form of a User Defined Function. FLUENT adopts a law-of-the-wall for the near wall temperature profile  $T^*$  as shown in the following equation 4.1

$$T^* = \frac{(T_w - T_p) \rho c_p k_p^{1/2}}{\dot{q}}$$

$$= \begin{cases} \text{Pr}_p y^* + \frac{1}{2} \text{Pr}_p \frac{C_\mu^{1/4} k_p^{1/2}}{\dot{q}} U_p^2 & (y^* < y_T^*) \\ \text{Pr}_t \left[ \frac{1}{\kappa} \ln(E y^*) + P \right] & (y^* > y_T^*) \end{cases}$$

4.1

where the subscript “p” means that the corresponding quantity is evaluated at the center of the near-wall cell.  $U$  is the flow velocity,  $\kappa$  is the von Karman constant ( $\kappa = 0.4187$ ),  $E$  is an empirical constant ( $E = 9.793$ ) and  $P$  is defined in [66]. The dimensionless distance  $y^*$  is defined in [47]. It serves the purpose of extending the wall function applicability to non-equilibrium boundary layers. In the case of slowly varying flow properties, as the one we are interested in, we have  $y^* = y^+$ . The critical value  $y_T^*$  corresponds to the intersection of the linear and logarithmic layers.

$\text{Pr}_t$  is the energy Prandtl number, which we used to tune the model as follows:  $\text{Pr}_t$  was first optimized to match the flat-channel experimental data for a reference case ( $V_{\text{in}} = 2$  m/s,  $Q = 1$  MW/m<sup>2</sup>), and later  $C_s$  (section 3.3.2, equation 3.29) was tuned for  $V_{\text{in}} = 2$  m/s,  $Q = 2$  MW/m<sup>2</sup>. This left the remaining part of the available experimental database free to validate the choice using fully independent information [67]. As explained above the free parameters used in the model are shown in table 3

Table 3. Parameters in the FLUENT / BR model.

<b>Parameter</b>	<b>Value</b>
$Pr_t$	0.1
$C_s$	8.4e-3

The following table shows the other key settings used to perform the simulation

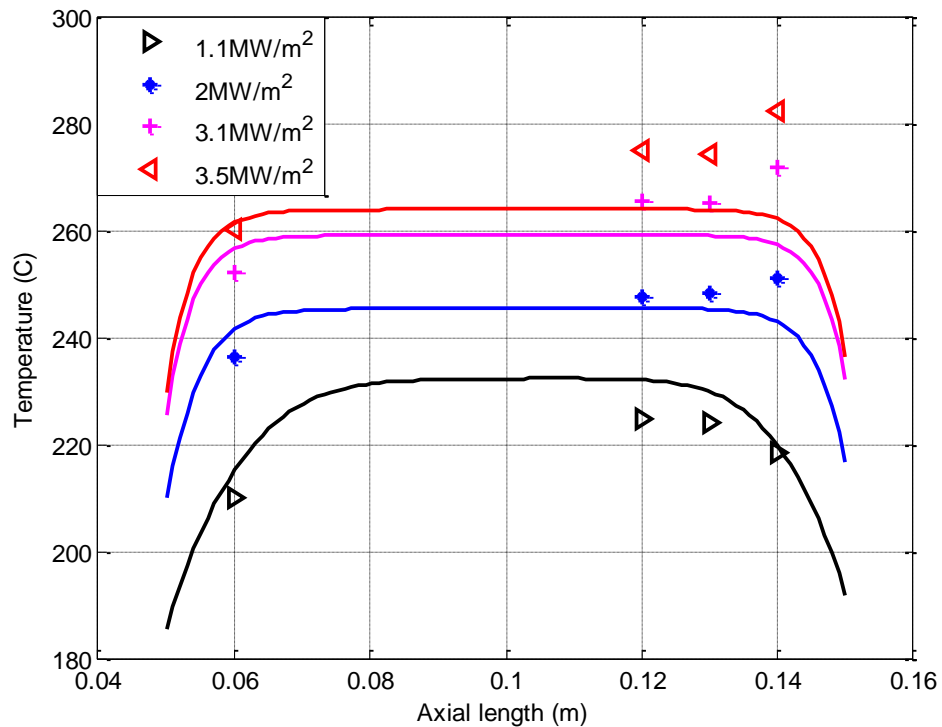
Table 4: Settings used to perform simulations using BR model

<b>Setting</b>	<b>Modeling choice</b>
Inlet velocity profile	Fully developed
Inlet temperature profile	Fully developed
Solver	Pressure based
Gravity	Not Included
Turbulence model	Realizable k- $\epsilon$ ,
Wall boiling model	BR model
Wall heat flux	Constant
Inlet boundary condition	Velocity inlet
Outlet boundary condition	Pressure outlet
Boundary condition for turbulent kinetic energy (Inlet & outlet)	Constant
Boundary condition for turbulent dissipation rate (Inlet & outlet)	Constant

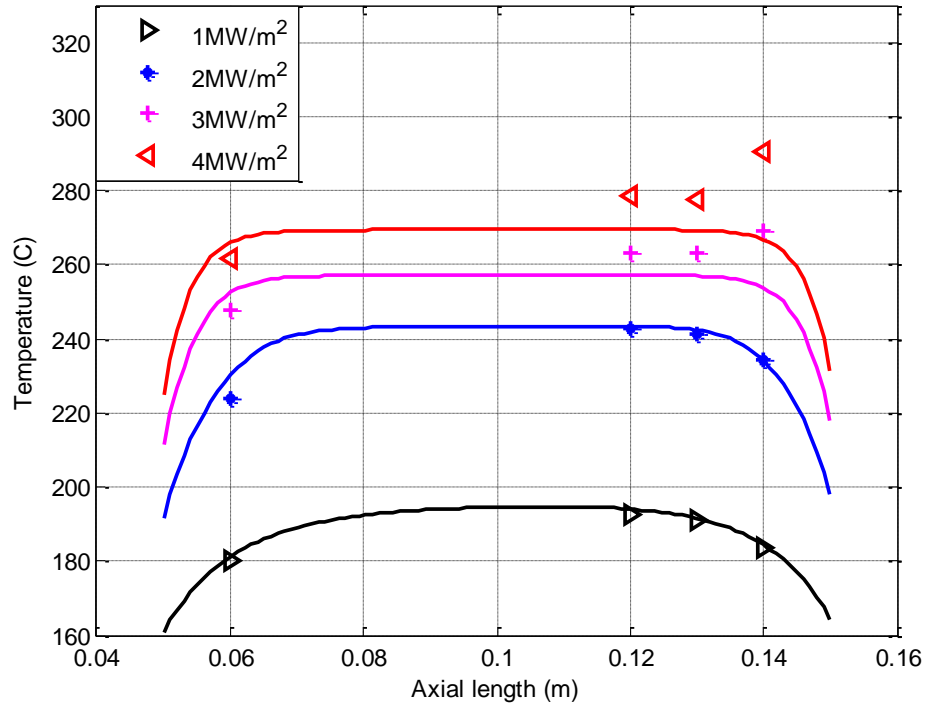
The above mentioned settings are used to perform the simulations on the flat channel geometry by using ANSYS FLUENT; the following strategy is adopted in order to get the solution faster

- First of all the computational domain is reduced; this is done by taking advantage of the symmetry in the geometry of the mockup along an axis parallel to the flow, which immediately reduces the number of cells to be used to half of the original mockup.
- We imposed fully developed flow conditions. We deemed it to be acceptable because in the experimental apparatus the entrance and exit ducts are orthogonal to the fluid flow in the main channel. This provides a sharp change in direction of the flow field which helps increasing turbulence. Moreover, the heated region starts  $\sim 17$  hydraulic diameters after the inlet section.

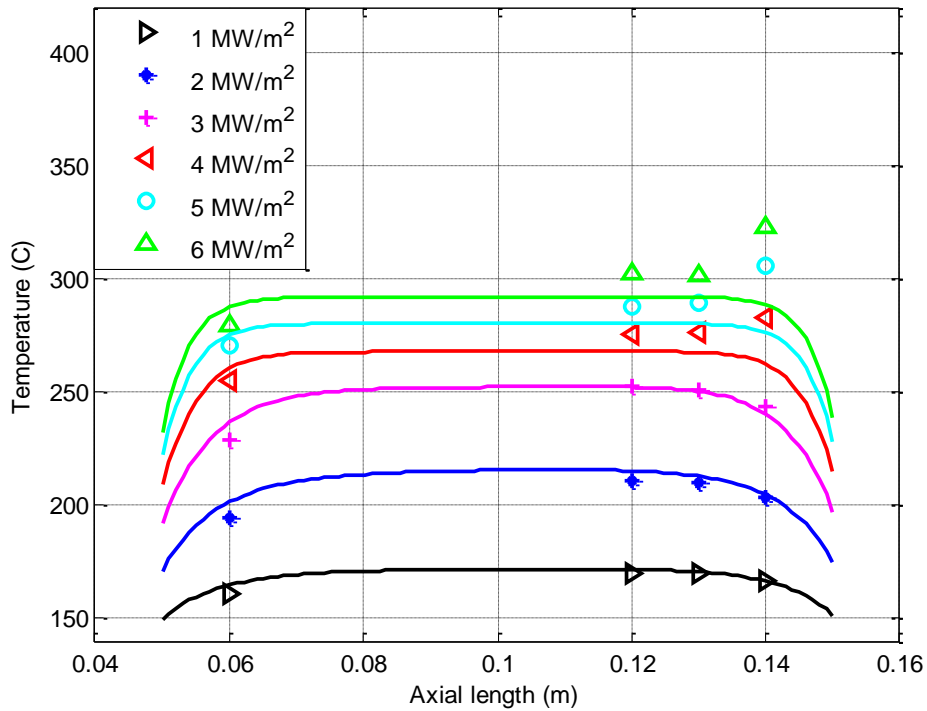
Figure 30 shows the results obtained by using the BR model. For higher heat fluxes, the measured temperature at the end of the heated section increases. This might be due to vapor accumulation near the end of the heated region, producing a localized thermal resistance and decreasing the heat transfer coefficient.



30 (a)



30 (b)



30 (c)

Fig 30: Comparison of temperatures computed with the BR model (solid line) with the experimental data (symbols) for different heat fluxes.(a)  $V_{in} = 1$  m/s, (b)  $V_{in} = 2$  m/s and (c)  $V_{in} = 4$  m/s.

As we observe from the comparison in figure 30, at lower heat fluxes (eg. For 2 m/s inlet velocity and heat fluxes  $< 2 \text{ MW/m}^2$ ) we observe there is a very good agreement between measured and simulated temperatures, with relative error  $< 8\%$ . However, as the heat flux is increased the relative error also increases up to  $\sim 15\%$ . The reason for this comes from the way in which the model is implemented in the code: it only accounts for the increase in heat transfer coefficient due to subcooled boiling and solves single phase flow equations, but does not account for the vapor formation. This fact is directly visible in the profiles: as we go to the end of heated region the profile is not following the path shown by the experimental data. So this model applicability is limited to low-to-moderate heat fluxes.

#### 4.1.4 Rohsenow model

As explained in chapter 3, this boiling model is coupled with the Eulerian in the volume of fluid (VOF) variation, to track the fluid-fluid interface, see also section 3.2.2.2 for the governing equations. In section 3.3.3 the details of the boiling model are presented. We also discussed that there are 6 free parameters in the model which have to be tuned for a particular application. In [29] Youchison did a similar task using STARCCM+; he mentioned that the six parameters in the boiling formalism are tuned in such a way that he obtained good agreement with data from high heat flux tests conducted at the Efremov Institute and at Sandia's Plasma Materials Test Facility on mock-ups with an open rectangular channel and on a Hypervapotron mock-up under a multitude of flow and heating flux conditions

The parameters from his data are given in table 5,

Table 5: Free parameters in the Rohsenow model, as determined by Youchison [29].

<b>Parameter</b>	<b>Value</b>
$C_{qw}$	0.01
$C_{ew}$	0.01
$HTC \times Area$	5e6
$\alpha$	0.3
$n_p$	1
$Sc_t$	0.5

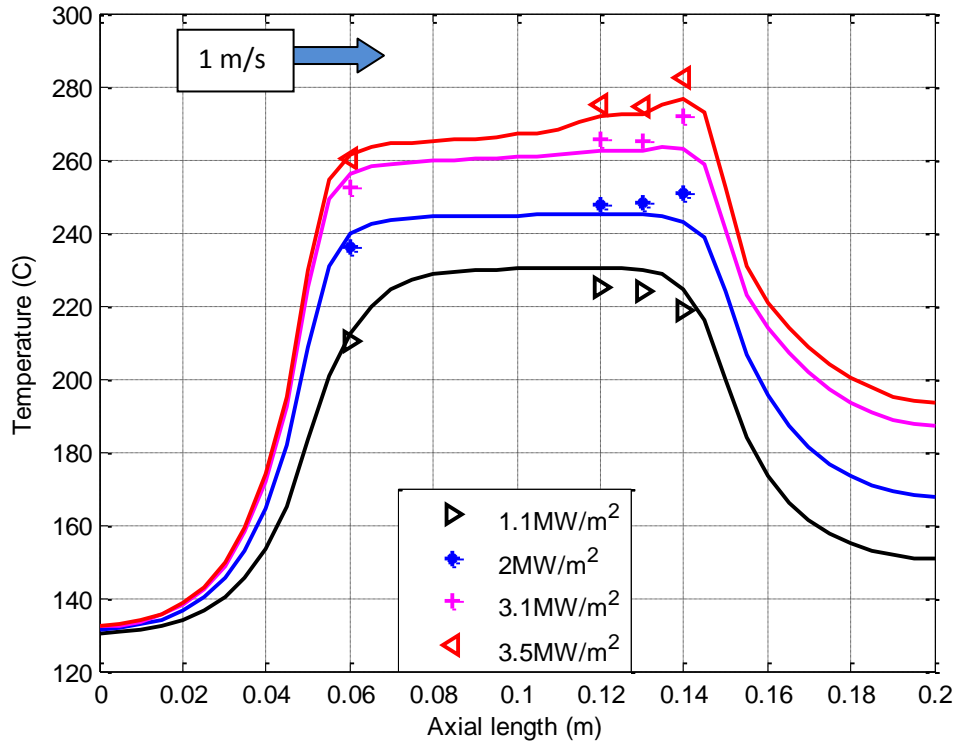
The following table shows the other key settings used to perform the simulation



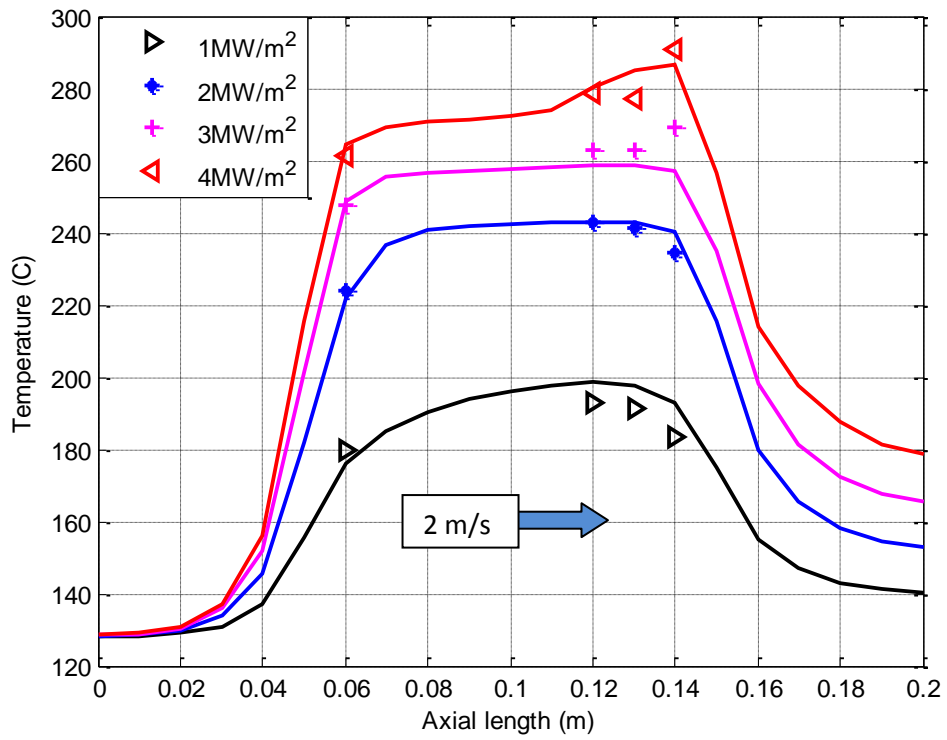
Table 6: Settings used to perform simulations using Rohsenow model

<b>Setting</b>	<b>Modeling choice</b>
Inlet velocity profile	Fully developed
Inlet temperature profile	Fully developed
Solver	Pressure based
Gravity	Included
Surface tension	Included
Turbulence model	Realizable k- $\epsilon$ ,
Wall boiling model	RPI model
Wall heat flux	Constant
Inlet volume fraction	1e-15
Inlet boundary condition	Velocity inlet
Outlet boundary condition	Pressure outlet
Boundary condition for turbulent kinetic energy (inlet & outlet)	Constant
Boundary condition for turbulent dissipation rate (inlet & outlet)	Constant

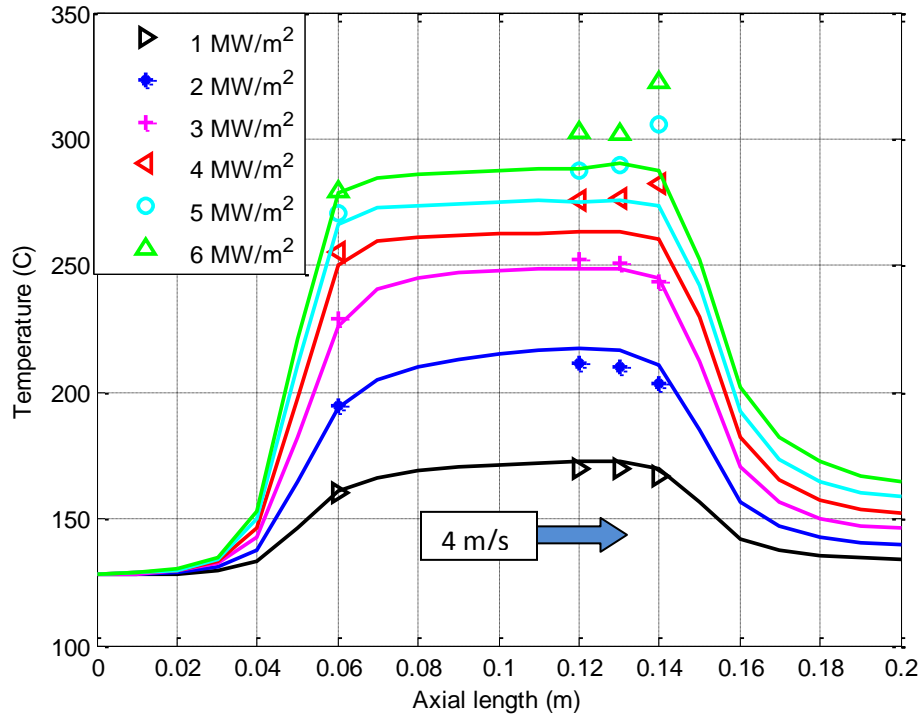
By using the above mentioned parameters simulations are performed on the flat channel geometry by using STARCCM+. The strategy adopted to achieve a proper numerical solution for BR model is also used here.



31 (a)



31 (b)



31 (c)

Fig 31: Comparison of temperatures computed with Rohsenow model (solid line) with the experimental data (symbols) for different heat fluxes and (a)  $V_{in} = 1$  m/s, (b)  $V_{in} = 2$  m/s and (c)  $V_{in} = 4$  m/s.

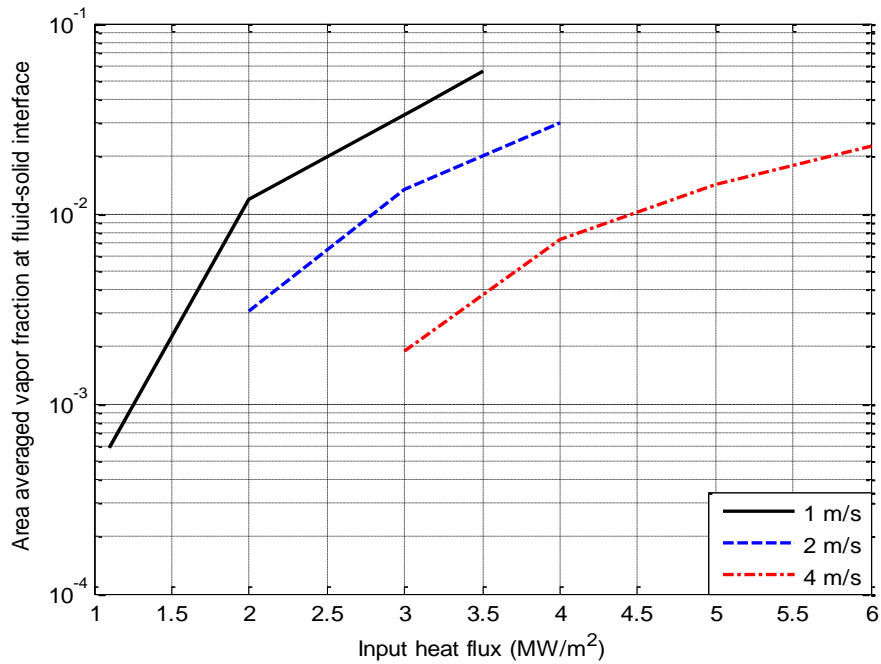


Fig 32: Flat channel-Rohsenow model. Vapor volume fraction, averaged over the fluid-solid interface on the heated side of the flat-channel, as a function of the input heat flux.  $V_{in} = 1, 2,$  and  $4$  m/s are considered.

Figure 31 shows the simulated results compared with the experimental data using the Rohsenow boiling model. Rohsenow model qualitatively follows the trend that is shown by the experiments for higher heat fluxes, which can be observed from the figure 31. The relative error using this model doesn't exceed 8% at all the observed heat fluxes and inlet velocities. Rohsenow model behaves better than BR model in terms of reproducing the experimental data, for more details see section 4.1.5. Figure 32 shows comparison of averaged vapor volume fraction using Rohsenow model for different inlet velocities and heat fluxes; from this it can be figured out that the average vapor volume fraction (over the upper fluid-solid interface), is extremely sensitive to the applied heat flux and inlet velocity. And for a particular heat flux the vapor generated is less for higher velocities, as expected.

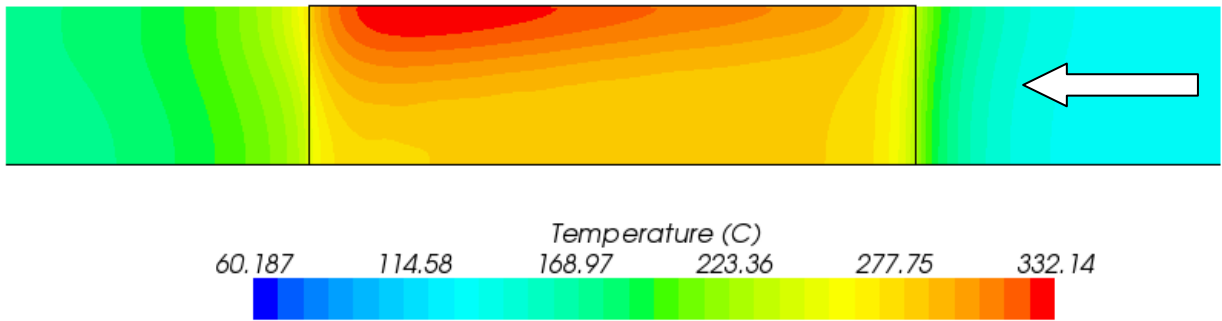
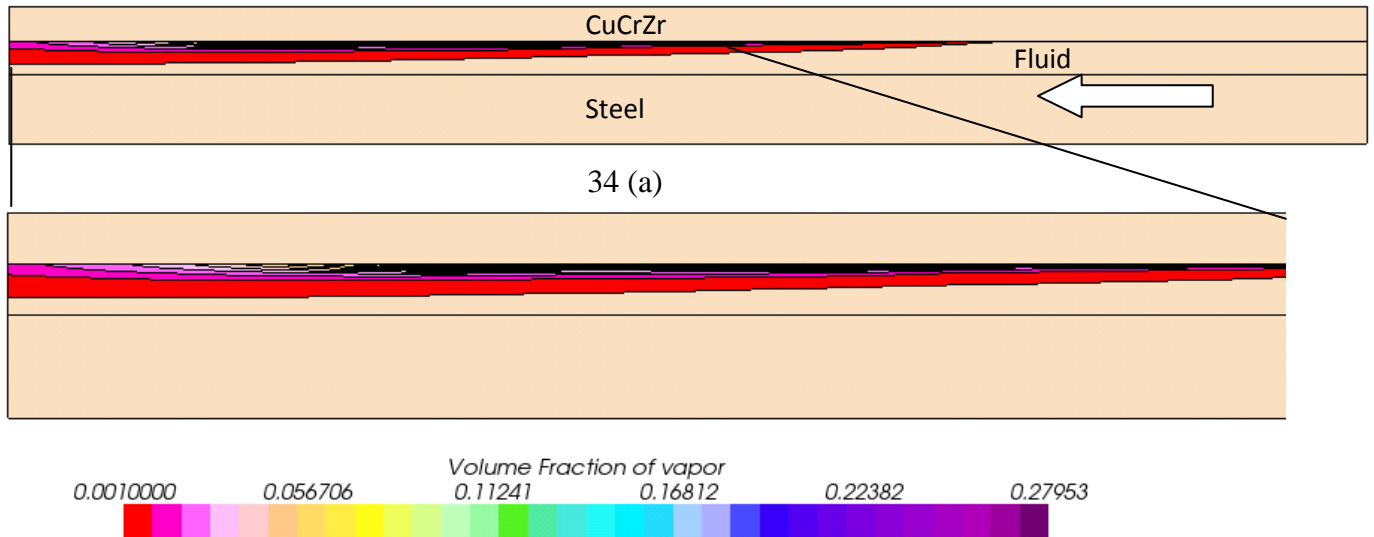


Fig 33: Flat channel, Surface temperature profile (CuCrZr face), for inlet velocity of 2 m/s and heat flux of 4 MW/m<sup>2</sup>.



34 (b)

Fig 34: vapor volume fraction profile at mid section, for inlet velocity of 2 m/s and heat flux of 4 MW/m<sup>2</sup> (a) over entire channel (b) Zoom at near the heated section

Figure 33 shows the surface temperature profile for inlet velocity of 2 m/s and surface heat flux of  $4 \text{ MW/m}^2$ , the maximum temperature reached is  $\sim 332 \text{ C}$ , and the peak temperature is found at the mid section of the mockup, near the end of the heated region. Figure 34 shows contours of volume fraction of vapor taken at mid section of the mockup, it can be observed from the figure that as we go towards the end of heated section the thickness of the vapor blanket increases thus increasing the surface temperature at the end and decreasing the heat transfer coefficient, which is evident from the experimental data discussed in section 2.1.2.

#### 4.1.5 Results comparison

In this section first, the computed results obtained using BR and the Rohsenow model are compared and some conclusions are drawn, later the results are compared with the previous work done on the same topic available in the literature.

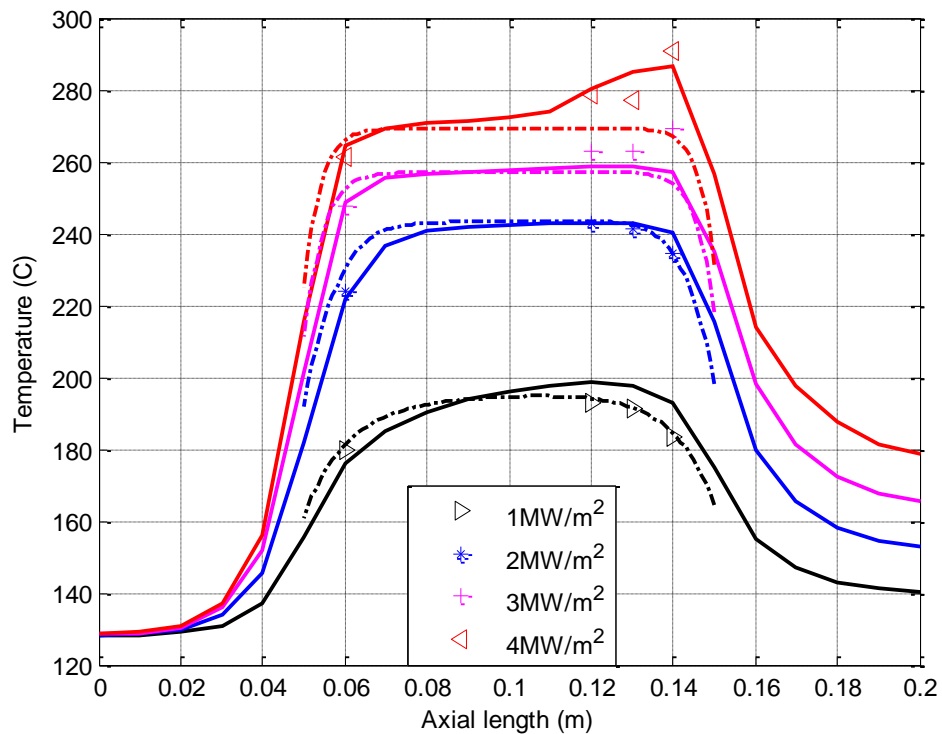


Fig 35: Flat channel. Comparison of temperatures computed with the Rohsenow (solid line) and the BR (dash-dot line) models, with the thermocouple data (symbols) for inlet velocity = 2 m/s and different heat flux levels.

Figure 35 shows results computed with the BR and the Rohsenow models against the experimental data. It can be observed from figure 35 that the Rohsenow model reproduces the shape of the peak in the temperature profiles at the end of the heated region for high heat fluxes, while the BR does not. In fact, at higher heat fluxes vapor accumulates near the end of the heated region, producing a localized thermal resistance which cannot be seen by the (single phase) BR

model. Thus the applicability of the BR model is limited for low to moderate heat fluxes. This also shows the superior capabilities of the Rohsenow model and its applicability to higher heat fluxes; so for studying the Hypervapotron thermal performance the Rohsenow model is considered as a potential candidate.

There were some tests conducted on the flat channel using BR model with the SC/TETRA code by Ying et al [32], in the article it was mentioned that their main objective is to validate the subcooled boiling model (BR model) in the SC/Tetra with the experimental data they have acquired from Sandia National Laboratories and at Efremov Institute. The error values found in this thesis using the simulations performed with BR model, with the geometry given by Efremov institute, are of the same order found in Ying et al work.

Youchison et al [29] conducted tests using Rohsenow model as in STAR-CCM+, with the experimental data they have acquired from Sandia National Laboratories and at Efremov Institute. The error values found in this thesis using the simulations performed with Rohsenow model, with the geometry given by Efremov institute, are of the same order found in Youchison et al work.

## 4.2 Hypervapotron

As discussed in chapter 2 the experimental data for Hypervapotron come from 2 different sources: the Efremov institute (Russia) and the JET tokamak (UK). The simulations performed over the mockups at these different laboratories will be discussed in this section, starting with the Russian data.

### 4.2.1 Efremov institute data

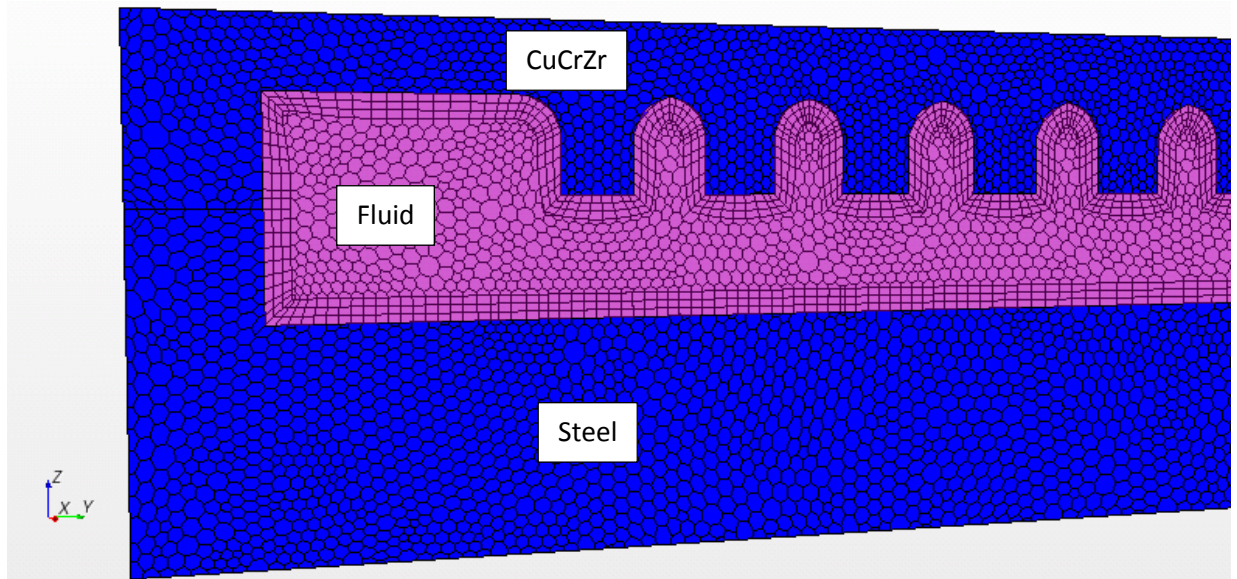


Fig 36: Mesh used for most of the computations for Hypervapotron.

The typical grid used for performing the tests on Hypervapotron is shown in figure 36. It is a non uniform unstructured polyhedral grid, for convenience of visualization the mesh is zoomed near the inlet.

#### 4.2.1.1 Rohsenow model

The free parameters used to run the first simulations are given in table 5. As a starting point we adopted the same parameters which proved to be satisfactory for the Flat channel.

Table 7: Settings used to perform simulations using Rohsenow model for Hypervapotron geometry

<b>Setting</b>	<b>Modeling choice</b>
Inlet velocity profile	Uniform
Inlet temperature profile	Uniform
Solver	Pressure based
Gravity	Included
Surface tension	Included
Turbulence model	Realizable k- $\epsilon$ ,
Wall boiling model	Rohsenow model
Wall heat flux	Constant
Inlet boundary condition	Velocity inlet
Outlet boundary condition	Pressure outlet
Boundary condition for turbulent kinetic energy (inlet & outlet)	Constant
Boundary condition for turbulent dissipation rate (inlet & outlet)	Constant

Table 7 shows the other key settings used to perform the simulation, the grid independence analysis for the Hypervapotron geometry was performed on the case 1 m/s (inlet velocity) and 4 MW/m<sup>2</sup> (heat flux). Initially using a uniform grid refinement factor of 1.2, increasing the number of cells in all the parts of mockup (CuCrZr, Fluid and Steel, figure 36), later only in fluid. Figure 37 shows the variation of temperature at the location of thermocouples with different grid sizes, from which it can be observed that the grid independence is non monotonic, and after refining the grid for 4 times the characteristic cell length scale has reduced to 0.25 mm corresponding to number of cells in the fluid about 10 million. At this point unfortunately we hit the capabilities of the machines which were used for performing the simulations. Figure 38 shows the variation of computational time with grid size for performing one iteration, as can be seen it was almost taking ~ 550 sec to perform one iteration (we performed the simulations on a Dell PE 1900, 2 Quadcore processors Xeon X5355 (2.66 GHz) with 16 GB RAM). Thus it was decided to abandon the Efremov institute data and go for data from JET, where the geometry used was smaller by a factor 20, thus allowing us to go for further refinement whenever required.

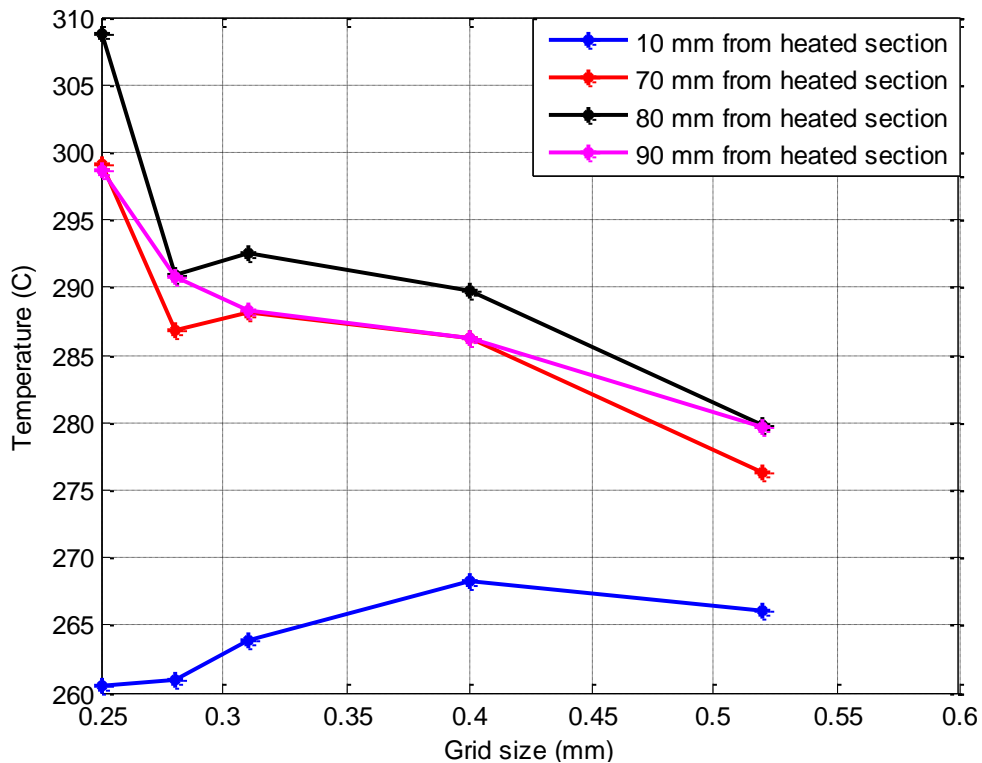


Fig 37: Variation of surface temperature with decreasing grid size at different thermocouple locations for 1 m/s inlet velocity and heat flux 4 MW/m<sup>2</sup>.



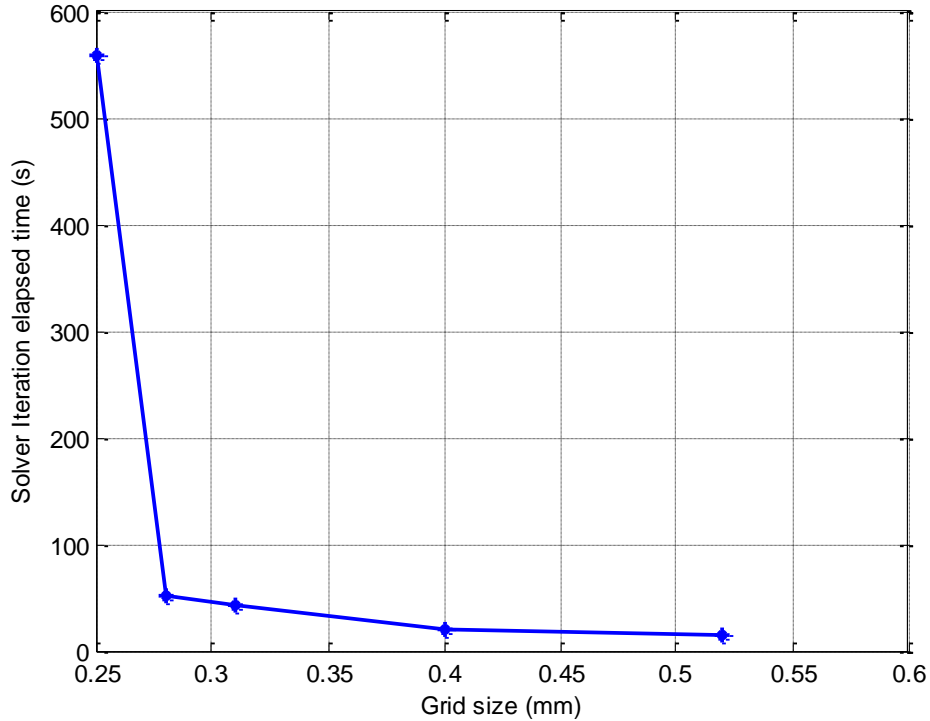


Fig 38: Variation of solver elapsed time per iteration with grid size for 1 m/s inlet velocity and heat flux  $4 \text{ MW/m}^2$

#### 4.2.2 JET data

The data available are for different cavity shapes, inlet velocities, and heat fluxes, as already explained in detail in chapter 2, section 2.2. For convenience the 4 validation cases with the relevant geometrical information are given in table 8 and figure 39.

In the following section first of all the simulations results obtained by using the Rohsenow model are discussed, and then the results obtained by using Transition boiling model will be presented. The strategy followed for performing the simulations using both the models is given below

- First of all the computational domain is reduced; this is done by taking advantage of the symmetry in the geometry of the mockup along an axis parallel to the flow, which immediately reduces the volume to be meshed to half of the original mockup.
- Grid independence analysis is performed on one of the cases which are discussed above. In particular Div 4x3 geometry is used (see section 4.2.2.1.1).
- Once the grid is finalized, the free parameters in the model are tuned (considering two cases i.e. two heat fluxes at the verge of changing boiling regime (see figure 25)) in such a way that the discrepancy between experimental and simulated data is  $<5\%$ .

- For each case the flow field is solved initially only for the liquid phase, and then the surface heat flux is applied.
- Once the above mentioned process is applied completely to a case, then similar grid size and free parameters obtained from the case are used for all the other cases to run the simulations.

Table 8: Summary of Hypervapotron validation cases [19]

Hypervapotron design	Boxscraper	Div 4×3mm	Div 6×6mm	MkI JET
Channel height	8mm	3mm	6mm	10mm
Channel width (z direction)	48mm	21mm	21mm	48mm
Cavity depth	4mm	4mm	6mm	8mm
Cavity width (x direction)	3mm	3mm	3mm	3mm
Front wall thickness	4mm	3mm	3mm	6mm
Cavity profile	Rounded	Square	Square	Rounded
Thermocouple position	Between twin channels, 3mm below from front surface	In the side wall, 2mm from the front surface	In the side wall, 2mm from the front surface	Between twin channels, 3mm below from front surface

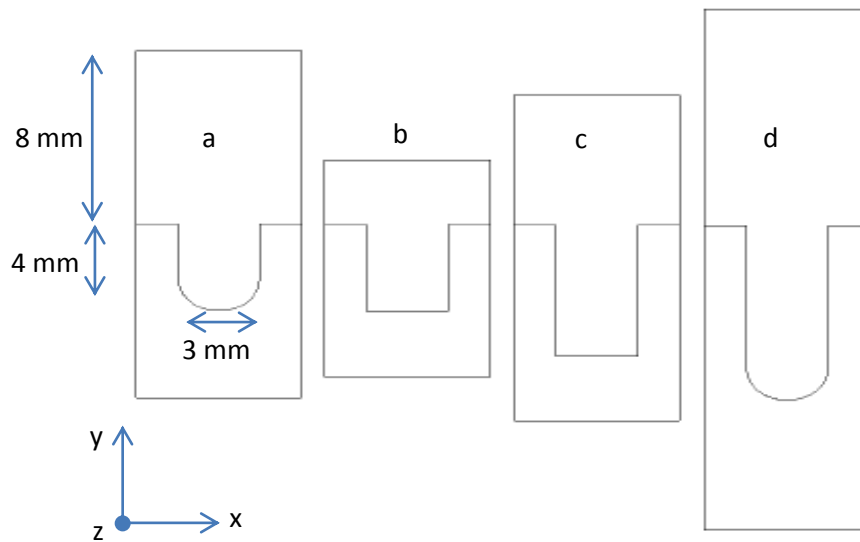


Fig 39: Hypervapotron cross-sections for a) Boxscraper, b) Div 4×3, c) Div6×6 and d) MkI respectively [19].

#### 4.2.2.1 Rohsenow model

In this section the simulated results obtained by using the Rohsenow model as in STARCCM+ for the 4 Hypervapotron geometries shown in table 6 are presented starting with DIV 4×3, then Boxscraper, then Div 6×6 and finishing with MkI Hypervapotron. Before presenting anything the strategy followed for selecting the grid and fine tuning of the parameters is explained.

##### 4.2.2.1.1. Grid selection

For selecting the proper grid a systematic grid convergence analysis is performed, using a grid refinement ratio of 1.2. For doing this analysis Div4×3 geometry is used, figure 40 shows geometry along with an example mesh used.

In figure 40 the bottom part is the front surface which receives the heat flux, and nothing much happens at the back surface (the top part) where the number of cells is kept as low as possible to reduce the computational time. Initially the number of cells is increased in both the solid and fluid parts; later the number of cells is only increased in the fluid, using the refinement ratio 1.2.

The convergence analysis is done for two heat fluxes at the verge of changing boiling physics (first one between no boiling to nucleate boiling and the second between nucleate boiling to hard boiling) as explained in chapter 2. The cases chosen were  $5.8 \text{ MW/m}^2$ ,  $18.7 \text{ MW/m}^2$ , and inlet velocity of 11 m/s.

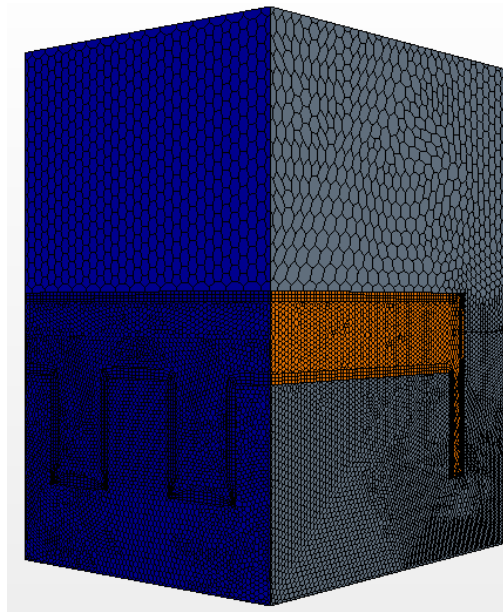
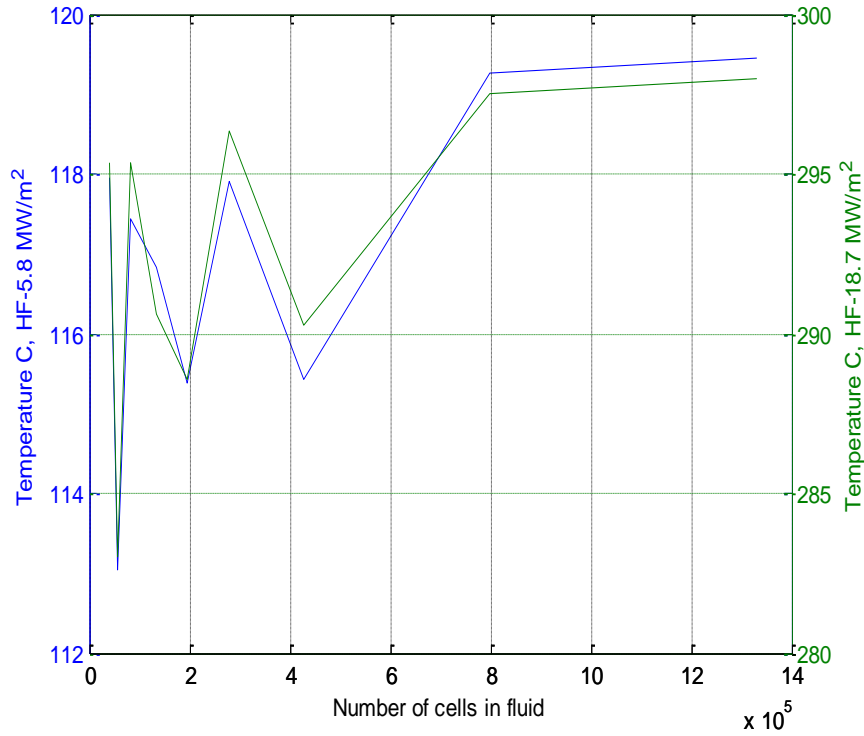
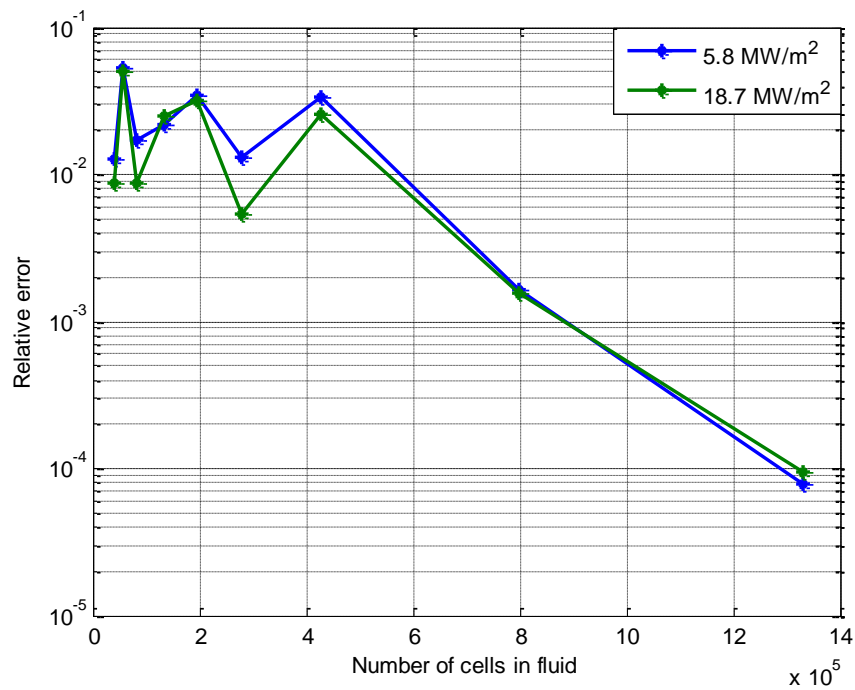


Fig 40: Div 4×3- Mesh used for most of the computations, non uniform unstructured polyhedral mesh.



41 (a)



41 (b)

Fig 41 : Grid convergence analysis on Div 4×3 for inlet velocity 11 m/s case (a) variation of temperature at thermocouple location with number of cells in fluid, (b) variation of relative error with number of cells in fluid

Figure 41 shows the grid convergence analysis performed for two cases mentioned before, where the variation of the surface temperature at the thermocouple location is shown and also the relative error (which is calculated as the ratio of, the difference between the data at thermocouple location with the extrapolated solution calculated using Richardson extrapolation to the extrapolated solution [68- 70]). It is estimated from the grid convergence analysis that the number of cells required in the fluid is in between 0.8-1.35 million. The grid size corresponding to 1 million cells in fluid for Div 4×3 case is assumed to give reasonably grid independent results for all other cases.

#### 4.2.2.1.2. Calibration of the model parameters

As discussed in the previous section, once the final grid size is decided the next step is to calibrate the model free parameters. There can be several ways for doing this analysis, but for this thesis the following steps are followed

1. First of all for a selected geometry and inlet conditions (Div 4×3 and 11 m/s inlet velocity) the two heat fluxes are chosen which are used for the convergence analysis (i.e. 5.8 and 18.7 MW/m<sup>2</sup> heat flux). As these two heat fluxes stand at the verge of changing boiling regimes, they will allow us to vary the parameters depending on the boiling physics independently for each one.
2. The 5.8 MW/m<sup>2</sup> heat flux is considered first, for this case the parameters are changed by doing educated guess based on physical considerations (e.g. the parameters that have a major effect on the solution for this heat flux level are  $C_{qw}$ ,  $n_p$ ,  $Sc_t$  while these parameters are little or not affected by the vapor formation, so mostly these three parameters are adjusted for this case), such that the discrepancy between the simulated and the experimental data is as low as possible.
3. Once a first optimum set is obtained, repeat the procedure for the case 18 MW/m<sup>2</sup> (in this case three parameters that are varied for 5 MW/m<sup>2</sup> are kept fixed).
4. The first proposed set of final parameters is then obtained by merging the two optima configuration obtained (this is relatively easy to do, because the global set of free parameters was effectively split in two decoupled subsets, each referring to a different boiling regime).
5. A fine tuning of the parameter is done at this point, considering the Div 4×3 geometry, 11 m/s inlet conditions, but varying the power over all the available levels.
6. Once the first optimum set is obtained then these parameters are applied on to the other set of initial conditions for this same geometry i.e Div 4×3.
7. Again the discrepancy was estimated for the new inlet conditions and then if necessary fine tuning of these parameters is done by varying the required parameter/s depending on the region where higher discrepancies are found (based on the tactics listed above).

8. Finally these new parameters and the old parameters (referring to parameters used in point 6) are averaged such that the obtained parameters give least error for all the inlet velocities and heat fluxes.
9. Once the parameters for this geometry are finalized, these parameters are used to run simulations on the other cases (i.e. geometries) without further tuning.

Once the above process is completed, the next step is to do simulations on all the cases reported. In the following sections we give the results obtained for each case using the Rohsenow model.

#### 4.2.2.1.3. Div 4×3

The geometry and the mesh used for Div 4×3 are shown in figure 40. In figure 42 the performance curves obtained from the experiments carried out are shown, which are used for comparison with simulated results. Each curve follows different boiling regimes, as we briefly pointed out in chapter 2. The parameters used for running the simulations after fine tuning are shown in the table 9, and the settings used for performing the simulations are reported next to the free parameters used in the model.

Table 9. Free parameters used in the Rohsenow model for Hypervapotron.

<b>Parameter</b>	<b>Value</b>
$C_{qw}$	0.01
$C_{ew}$	0.0125
$HTC \times Area$	1e6
$\alpha$	0.1
$n_p$	0.85
$Sc_t$	1

The other key settings used to perform the simulation

Table 10: Settings used to perform simulations using Rohsenow model for Hypervapotron geometry

<b>Setting</b>	<b>Modeling choice</b>
Inlet velocity profile	Uniform
Inlet temperature profile	Uniform
Solver	Pressure based
Gravity	Included
Surface tension	Included
Turbulence model	Realizable k- $\epsilon$ ,
Wall boiling model	Rohsenow model
Wall heat flux	Constant
Inlet volume fraction	1e-15
Inlet boundary condition	Velocity inlet
Outlet boundary condition	Pressure outlet
Boundary condition for turbulent kinetic energy (inlet & outlet)	Constant
Boundary condition for turbulent dissipation rate (inlet & outlet)	Constant

Results obtained after running the simulations are shown in figure 43, which shows the comparison of experimental data with the simulation results for different inlet velocity and heat fluxes.

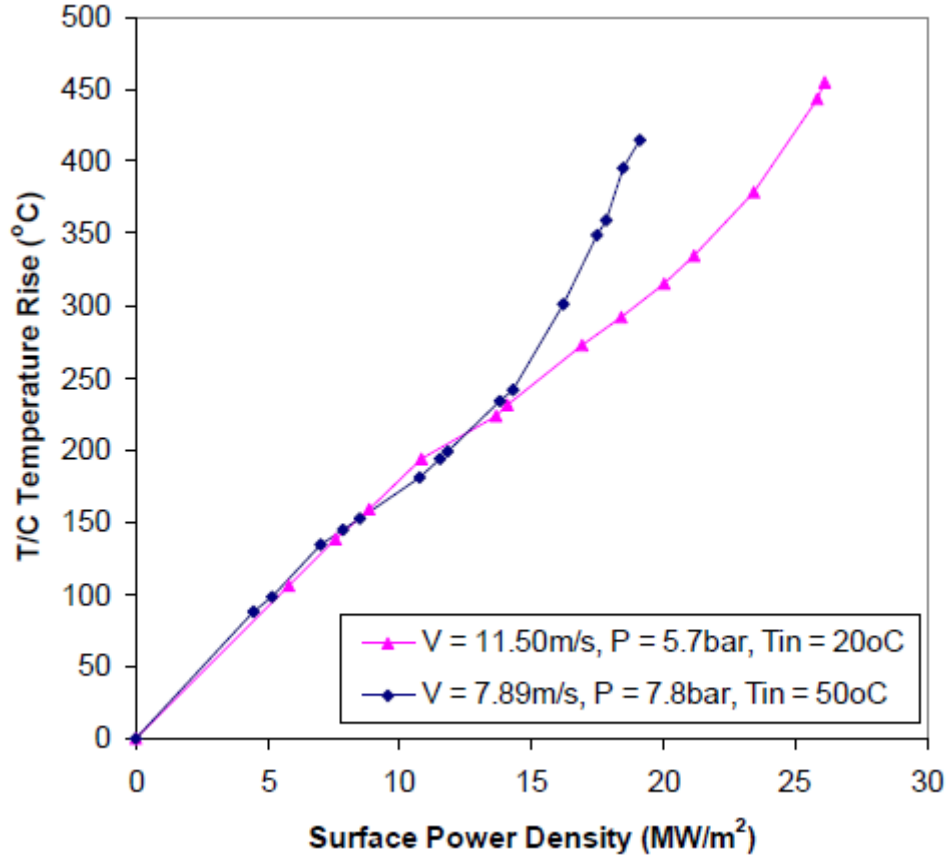


Fig 42: Div 4×3mm experimental data used in the CFD validation exercise [19]

The Rohsenow model shows very good agreement with the experimental data for all given inlet conditions and heat fluxes. However, this model is able to show the change in slope only while going from no boiling to nucleate boiling conditions but not the second change in slope as explained in chapter 2 at the end of section 2.2.3. Quantitatively this boiling model shows very good agreement in all regimes but qualitatively (in terms of following the characteristic nature of the experimental data) it doesn't follow the slope changes as we go from one boiling regime to the other (look for circles in figure 43 for 7.89 m/s inlet velocity case).

Figure 44 (a) shows the temperature contours in the Div 4×3 system and 44 (b) shows the vapor volume fraction in the fluid domain. The inlet conditions used are 11 m/s and 18.7 MW/m<sup>2</sup> heat flux. From figure 44 it can be observed that the majority of vapor is generated at the center of the channel (near the symmetry), while most of the vapor is driven away in the side channel. The maximum temperature observed at the front face is around 480 C.



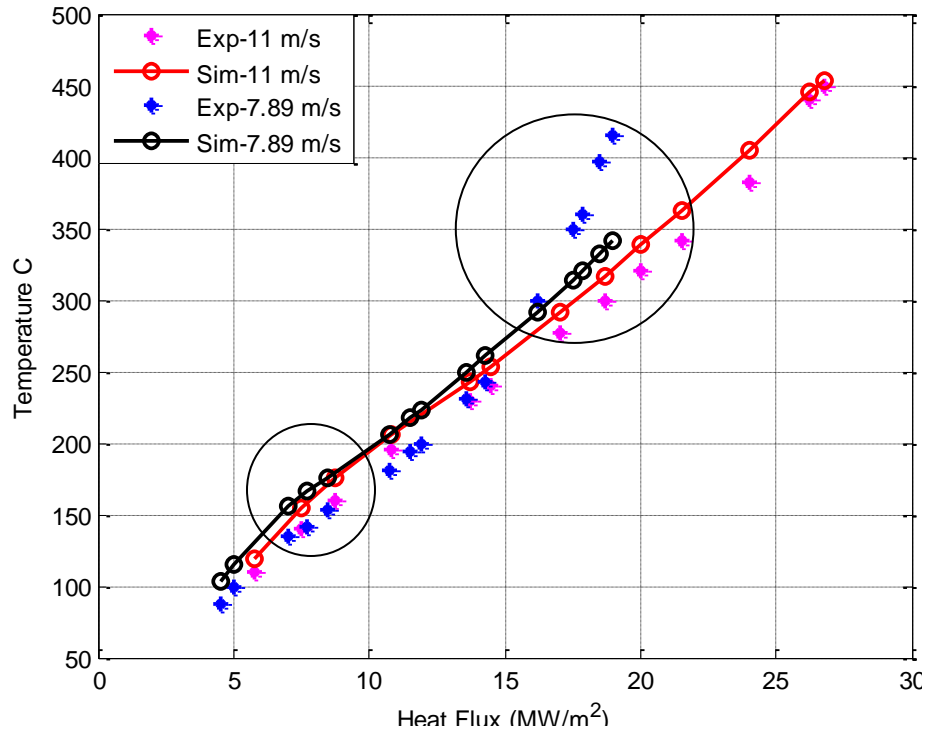
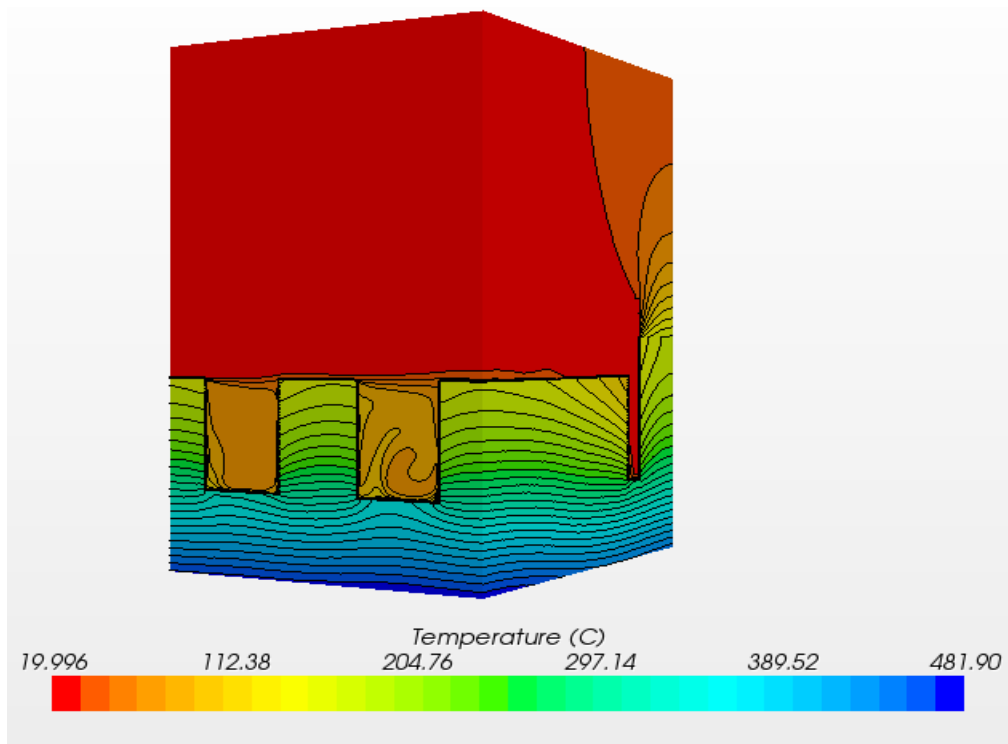
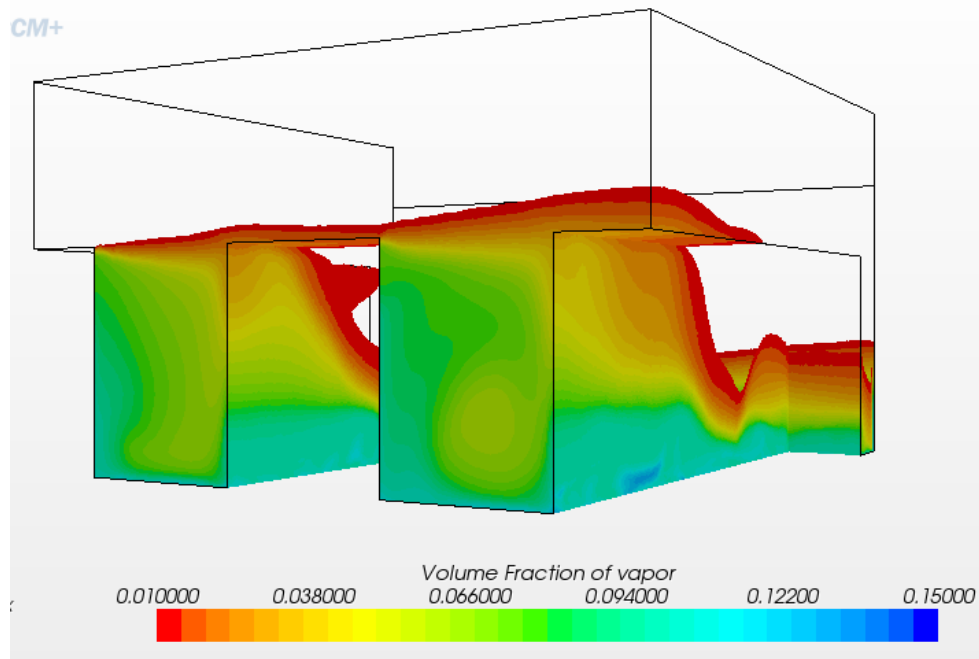


Fig 43: Div 4×3, Comparison of temperatures computed with Rohsenow model (solid line) with the experimental data (symbols) for different heat fluxes and inlet velocities.



44 (a)



44 (b)

Fig 44: Div 4×3 (a) Temperature contours in the solid and fluid domain, (b) vapor volume fraction, for inlet velocity of 11 m/s and surface heat flux of 18.7 MW/m<sup>2</sup>.

#### 4.2.2.1.4. Boxscraper

The details of the experimental data for this geometry are given in chapter 2, where it is also mentioned that the data for this case are comprehensive and cover the 3 regimes of interest (no boiling, nucleate and hard boiling regimes). The main drawback of the data comes from the lack of information about the inlet conditions such as inlet temperature, and operating pressure. As suggested in the thesis of J.Milnes [19], the inlet temperature is assumed to be 50 C and the inlet pressure to be 6 bar for the computations. Finally to reduce the number of runs to a reasonable level, it was decided to select only 2 of the 4 curves, specifically those corresponding to inlet flow velocities of 4 and 8.55m/s respectively,. Figure 45 shows the performance curves obtained from the available experimental data, which are used for comparison with simulated results.

The grid size used for this case is similar to the grid size used for the DIV 4x3 case, figure 46 shows the mesh used to perform the simulations. The free parameters used are same as that used for Div 4×3 geometry, which are shown in table 9. The same settings and strategy are used for running the simulations as used for DIV 4×3 case. Figure 47 shows the comparison of simulated with experimental data for different velocities.

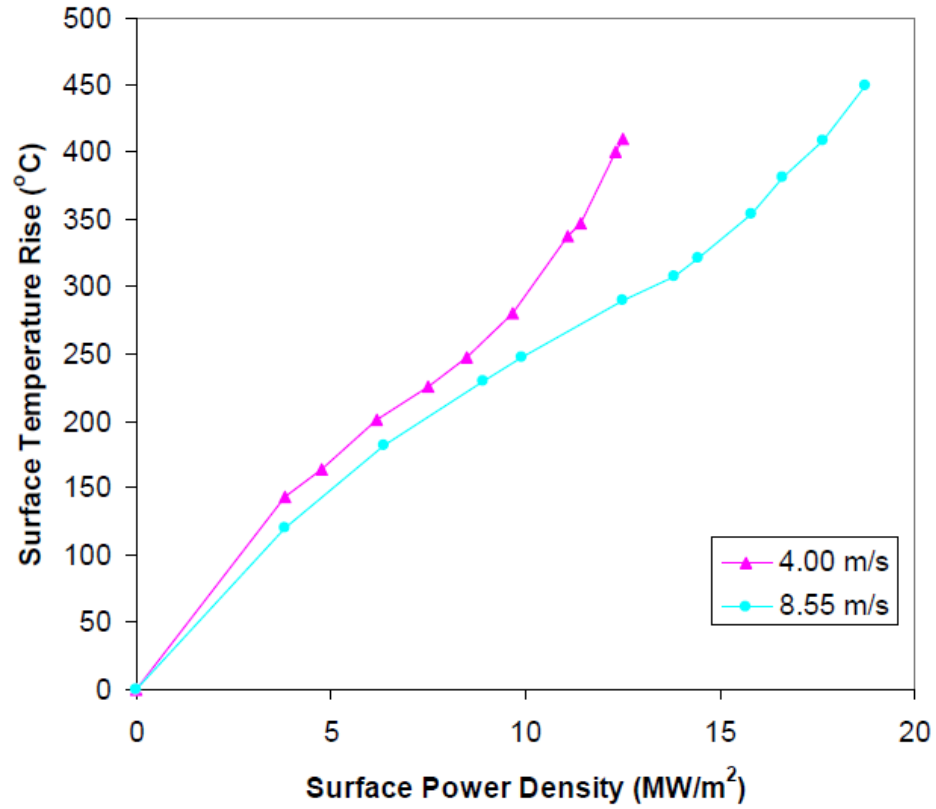


Fig 45: Boxscraper experimental data [19]

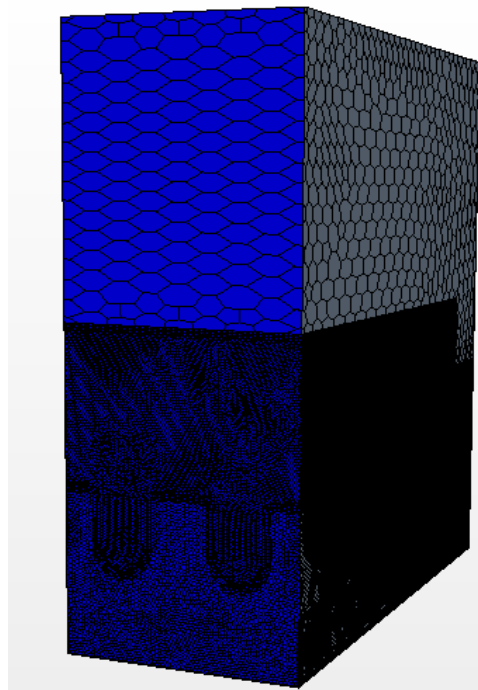


Fig 46: Boxscraper- Mesh used for most of the computations, non uniform unstructured polyhedral mesh.

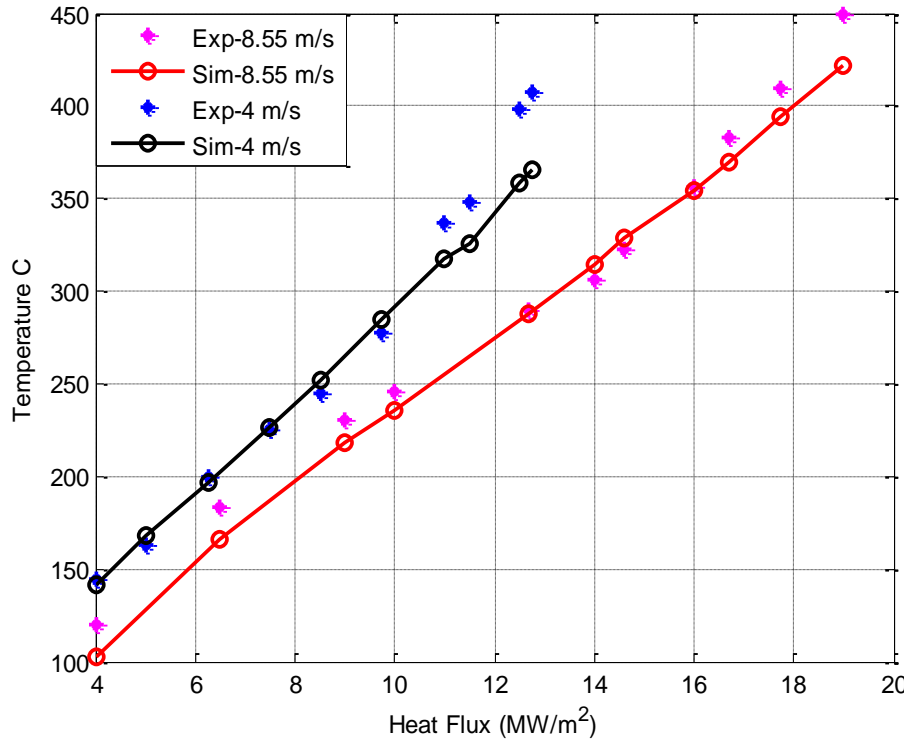


Fig 47: Boxscraper, Comparison of temperatures computed with Rohsenow model (solid line) with the experimental data (symbols) for different heat fluxes and inlet velocities.

As can be observed from figure 47, the results are in good agreement with the experimental data over all the regimes, which indicated that the free parameters set are having good applicability when we change the cavity shape from square to circular. But it has the same problem as listed for the Div 4×3 case: this model is able to show the change in slope only while going from no boiling to nucleate boiling conditions.

#### 4.2.2.1.5. Div 6×6

The details of the experimental data for this geometry are given in chapter 2, where it is also said that the main drawback of the data comes from the lack of information about the inlet conditions such as inlet temperature, operating pressure. As suggested in the thesis of J.Milnes [19], the inlet temperature is assumed to be 50 C and the inlet pressure to be 6 bar for the computations. Figure 48 shows the performance curves obtained from the experiments carried out, which are used for comparison with simulated results.

The grid size used for this case is similar to the grid size used for the Div 4×3 case, figure 49 shows the mesh used to perform the simulations. Also the model free parameters and running strategy already successful for the Div 4×3 geometry are reproduced here. Figure 50 shows the comparison of simulated data with experimental data for different velocities.

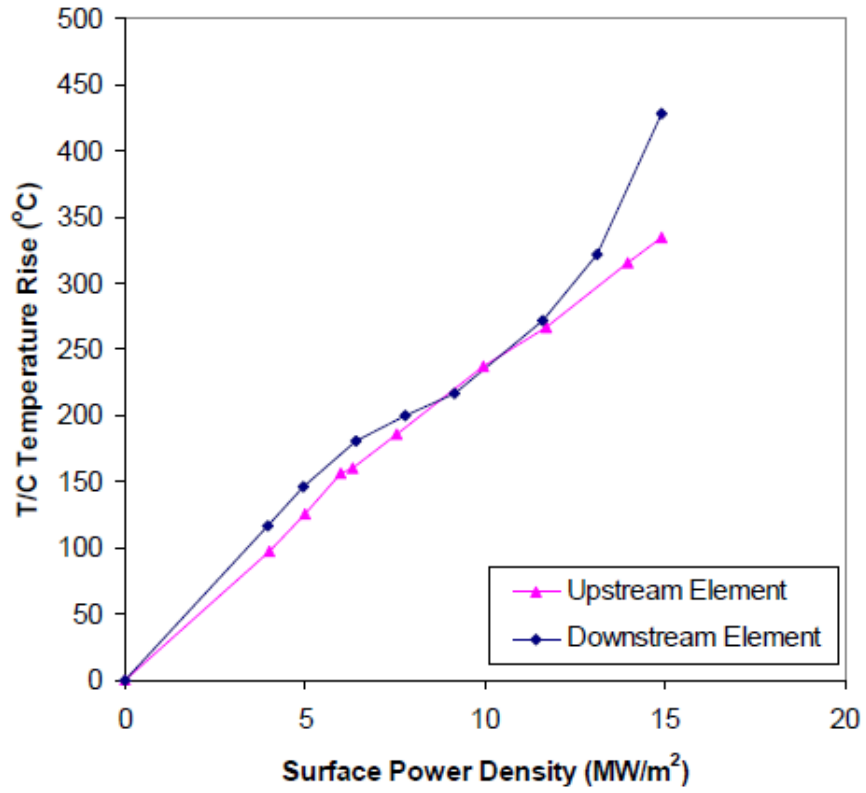


Fig 48: Div 6×6 experimental data [19]

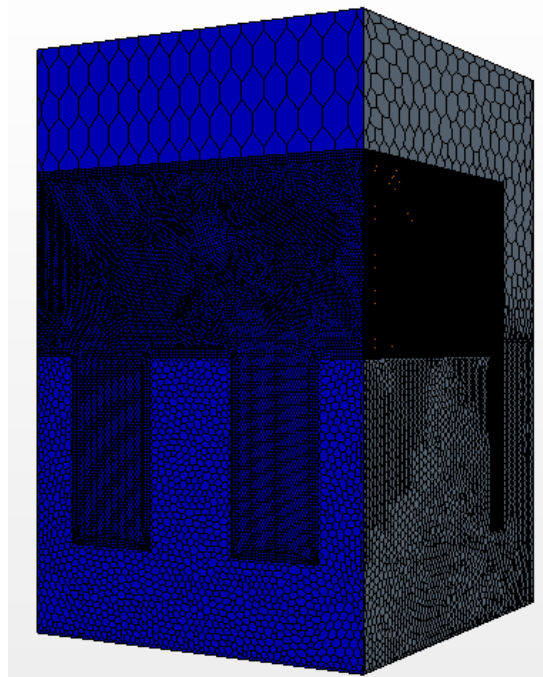


Fig 49: Div 6×6- Mesh used for most of the computations, non uniform unstructured polyhedral mesh.

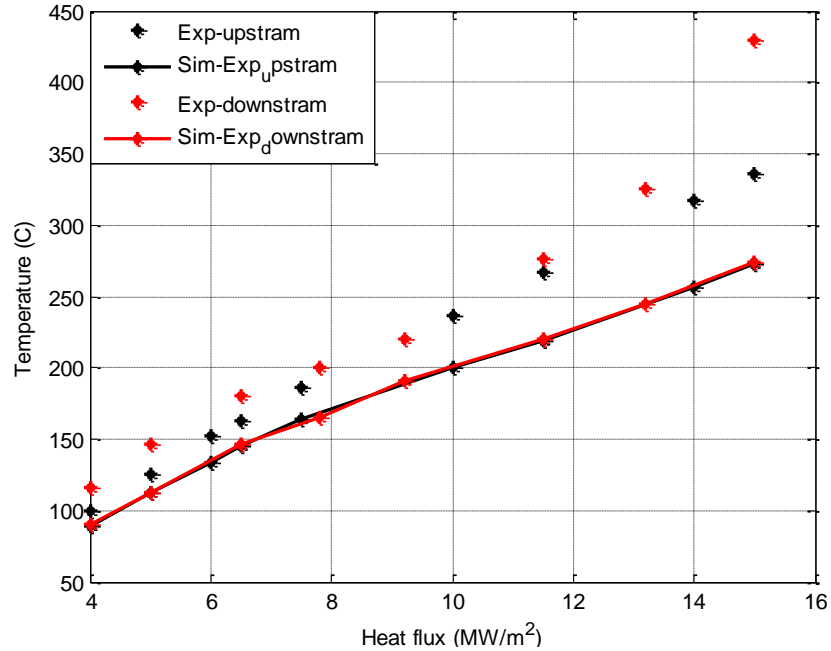


Fig 50: Div 6×6, Comparison of temperatures computed with Rohsenow model (solid line) with the experimental data (symbols) for different heat fluxes and inlet velocities.

#### 4.2.2.1.6. MkI

The details of the experimental data for this geometry are given in chapter 2. In the original paper [38] the error bars are not given: the error bars are taken from the data points which indicate significant errors in the measurement of temperature. In the paper, the plotted data between temperature and heat flux does not mention that the temperature is surface temperature rise (i.e. the difference between absolute thermocouple temperature and the initial temperature of the surface) or the absolute temperature of the thermocouple. The inlet temperature of the fluid entering the channel is assumed to be 50 C [19].

According to J.Milnes thesis, it was mentioned that the resultant data with error bars is derived such that, if the original data was surface temperature rise with an inlet temperature of ~50 C, then it would yield the data at the lower bound of the error bars. If, however, the original data was indeed a measure of the absolute temperature, this would yield the values at the upper bound of the error bars. Figure 51 shows the performance curves obtained from the experiments carried out together with the error bars, which are used for comparison with simulated results. Figure 52 shows the grid used for performing the simulations

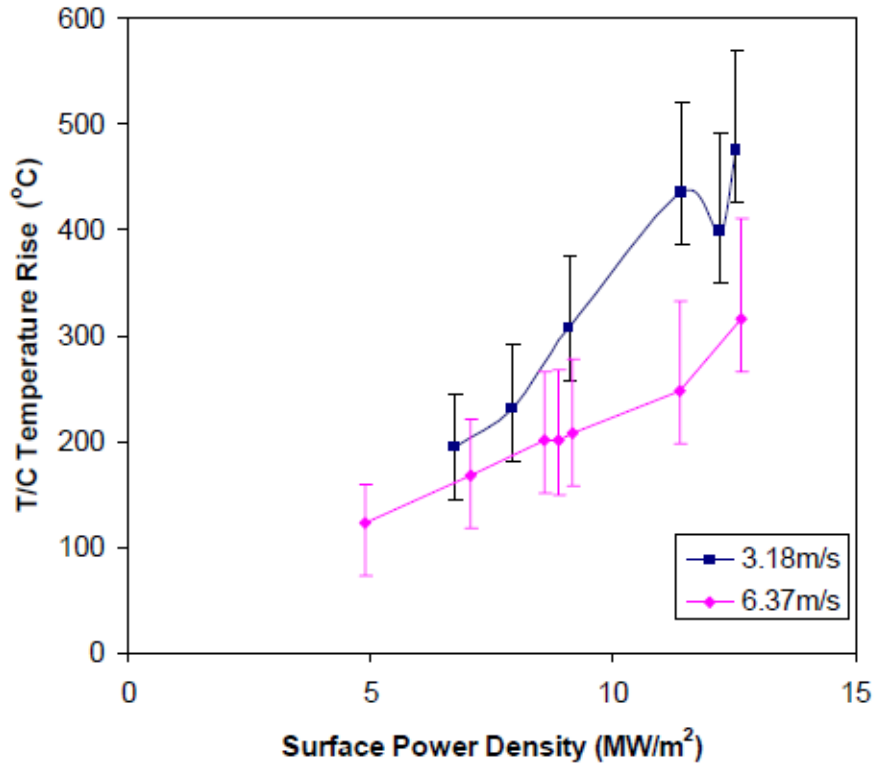


Fig 51: Mk1 experimental data [19]

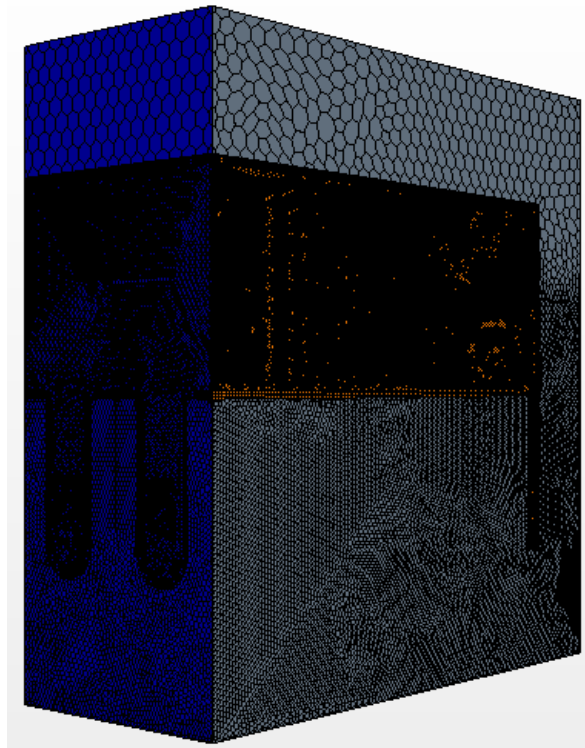


Fig 52: Mk1- Mesh used for most of the computations, non uniform unstructured polyhedral mesh.

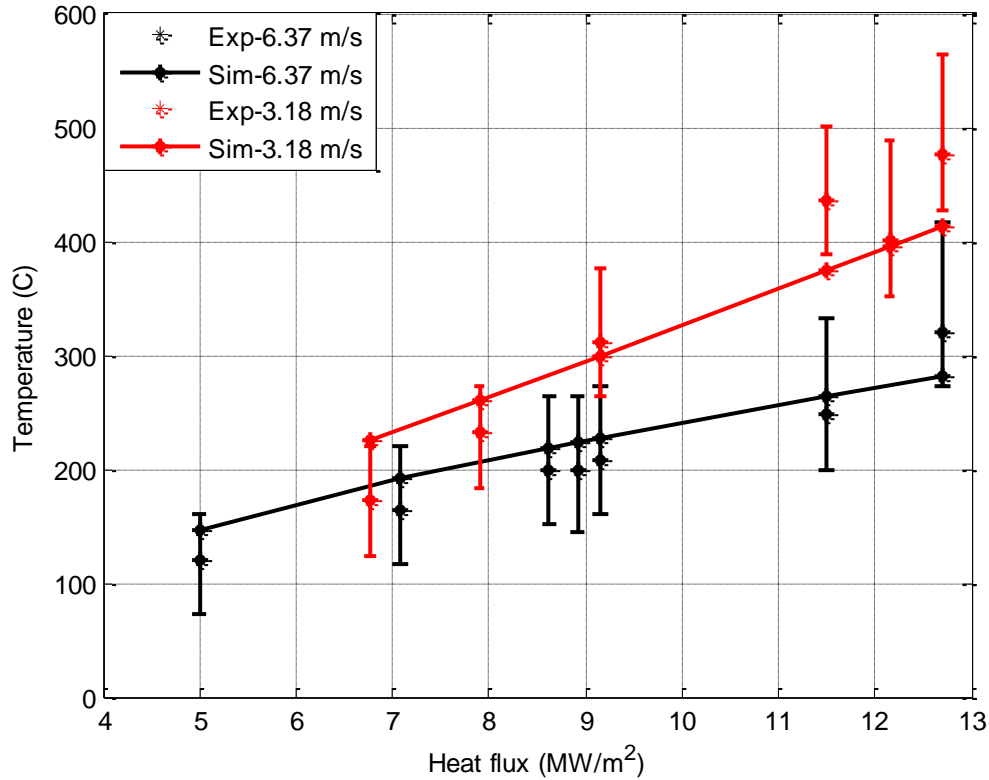


Fig 53: Mk1, Comparison of temperatures computed with Rohsenow model (solid line) with the experimental data (symbols) for different heat fluxes and inlet velocities.

The results shown above are in good agreement with the experimental data; the model proves that it is capable of predicting the performance of Hypervapotron very well quantitatively for a given set of free parameters derived using one particular case.

#### 4.2.2.2. Transition boiling model

As explained in chapter 3 this boiling model is coupled with the Eulerian approach to solve the fluid flow with volume of fluid method to track fluid-fluid interface, see also section 3.2.2.2 for a more detailed discussion. In section 3.3.4 the details of the boiling models along with the information to find out the key terms are presented, it is also discussed that there are 9 free parameters in the model which have to be tuned for a particular application. Since there are some similarities between this and the Rohsenow model some of the free parameters such as  $C_{ew}$ ,  $S_{ct}$  and  $C_{HTC \times Area}$  are kept frozen [see section 3.3.4].

The grid size, which was estimated as explained in 4.2.2.1.1, is found sufficient for running simulations using this model. The next step after deciding the grid size is to tune the free parameters in the model. A strategy similar to that explained in 4.2.2.1.2 is followed using Div 4×3 geometry and the final parameters are reported in table 11



Table 11: Free parameters used in the Transition boiling model for Hypervapotron.

<b>Parameter</b>	<b>Value</b>
$C_{ew}$	0.0125
$HTC \times Area$	1e6
$q_{max}$	9e6
$\Delta T_1$	55
$\Delta T_2$	140
$\phi$	0.75
K1	1.2
K2	1.25
$Sc_t$	1

The following table shows the other key settings used to perform the simulation

Table 12: Settings used to perform simulations using Transition boiling model

<b>Setting</b>	<b>Modeling choice</b>
Inlet velocity profile	Uniform
Inlet temperature profile	Uniform
Solver	Pressure based
Gravity	Included
Surface tension	Included
Turbulence model	Realizable k- $\epsilon$ ,
Wall boiling model	Transition boiling model

Wall heat flux	Constant
Inlet volume fraction	1e-15
Inlet boundary condition	Velocity inlet
Outlet boundary condition	Pressure outlet
Boundary condition for turbulent kinetic energy (inlet & outlet)	Constant
Boundary condition for turbulent dissipation rate (inlet & outlet)	Constant

In the following sections the key results obtained by our modeling campaign are presented.

#### 4.2.2.2.1. Div 4×3

The details about the experimental data and other key points are explained in section 4.2.2.1.3, the free parameters used are shown in table 11 followed by the key settings in the model in table 12. Figure 54 shows the comparison of the simulated with the experimental data for the given heat flux and inlet velocities

The Transition boiling model shows very good agreement with the experimental data for all given inlet conditions and heat fluxes. This model is able to show the change in slope while going from no boiling to nucleate and hard boiling conditions. The results obtained from this model are in good agreement with the experimental data qualitatively and quantitatively, almost covering all the boiling regimes, showing its superiority over the Rohsenow boiling model, for more details see section 4.2.2.2.3.

Figure 55 shows the contours of temperatures and vapor volume fraction using transition boiling model, the maximum surface temperature reached using this model is 474 C, and the maximum vapor volume fraction in the fluid is 0.47. More vapor is generated at the center of the channel (near the symmetry), and most of the vapor is driven away in the side channel.

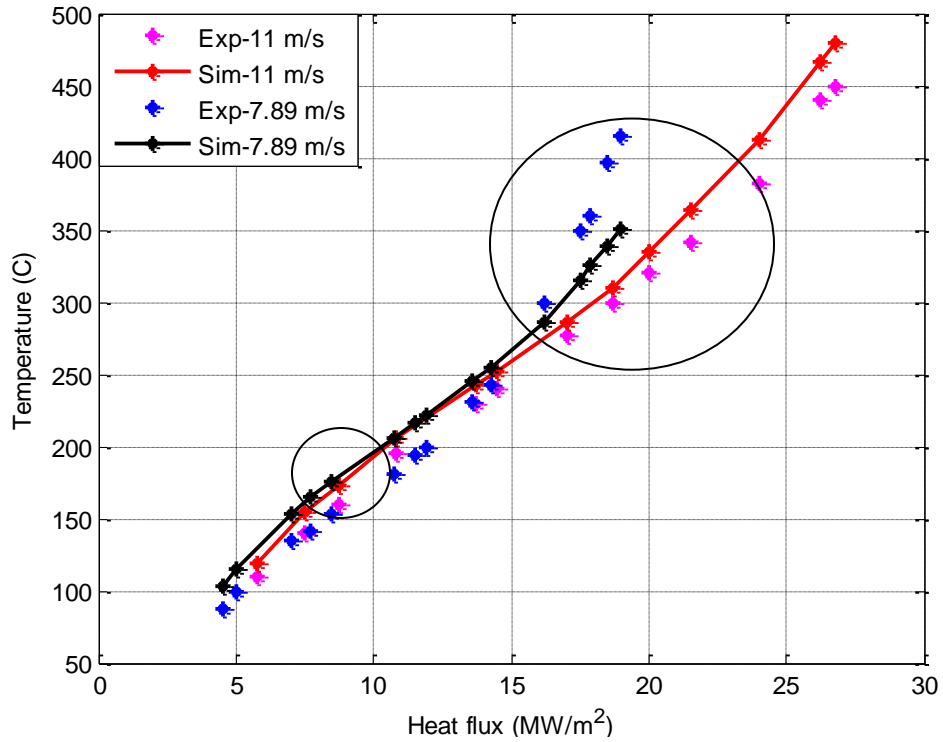
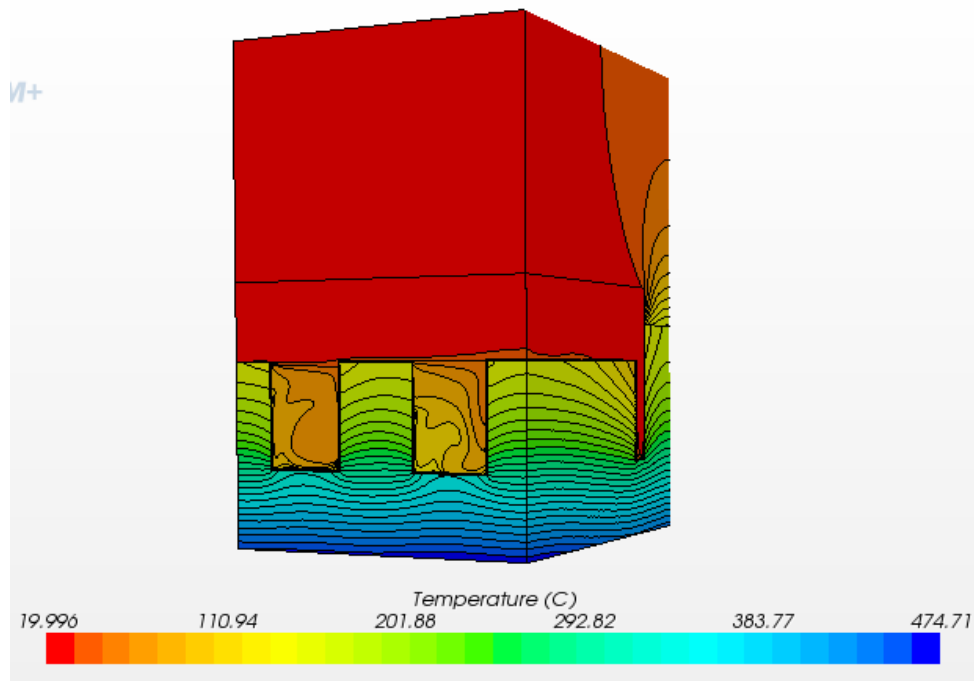
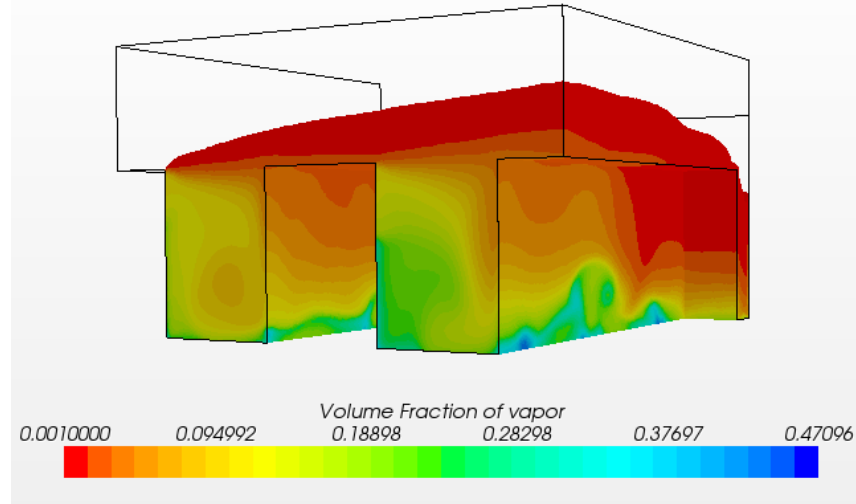


Fig 54: Div 4×3, comparison of temperatures computed with Transition boiling model (solid line) with the experimental data (symbols) for different heat fluxes and inlet velocities.



55 (a)



55 (b)

Fig 55: Div 4×3 (a) Temperature contours in the solid and fluid domain, (b) vapor volume fraction, for inlet velocity of 11 m/s and surface heat flux of 18.7 MW/m<sup>2</sup>.

#### 4.2.2.2.2. Boxscraper, Div 6×6 and Mk1

In this section the results obtained using the transition boiling model with the geometries of all the other Hypervapotron configurations i.e. Boxscraper, Div 6×6 and MkI are given. The details about the experimental data and some other key points (including the inlet conditions) are explained for the three geometries in sections 4.2.2.1.4-4.2.2.1.6. The free parameters used are shown in table 11 followed by the key settings in the model. Figures 56-58 show the comparison of the simulated with the experimental data for the given heat flux and inlet velocities. It can be observed that the free parameter set derived using Div 4×3 geometry is able to reproduce the thermal performance in terms of thermocouple temperature measurement even if the cavity shapes are changed.

The results obtained with this model in most cases are better than or at least similar to those obtained with the Rohsenow model. The main advantage of this model is the freedom given in terms of the free parameters which allows us to simulate the three boiling regimes by properly adjusting them. This model gives us confidence about using commercial CFD codes for predicting the thermal performance of the Hypervapotron as these results follow the qualitative shape of the experimental data allowing us to get much closer to what is happening in the physics of the Hypervapotron.

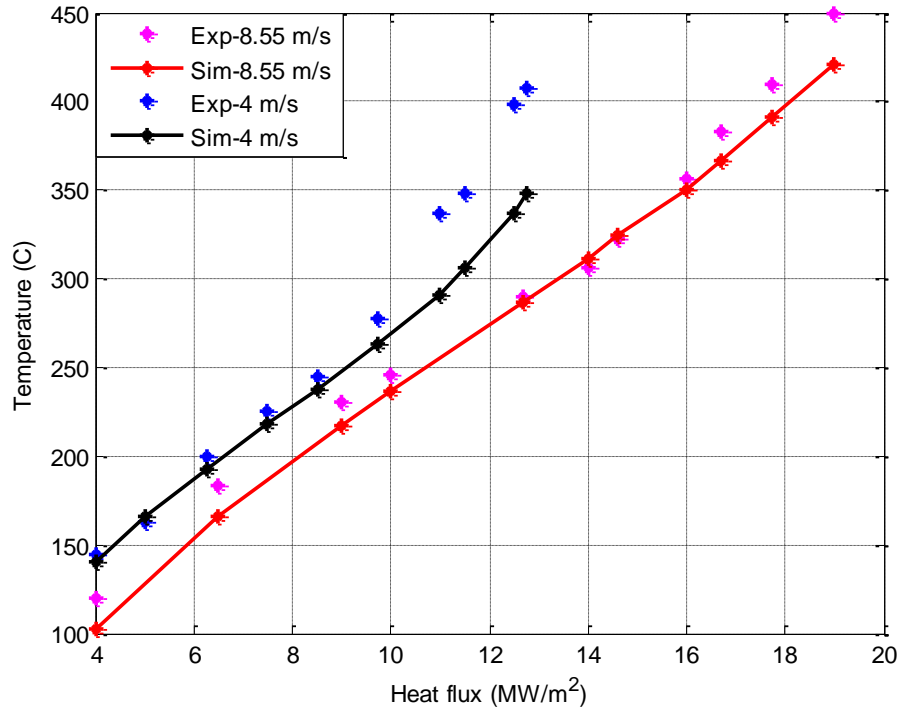


Fig 56: Boxscraper, comparison of temperatures computed with Transition boiling model (solid line) with the experimental data (symbols) for different heat fluxes and inlet velocities.

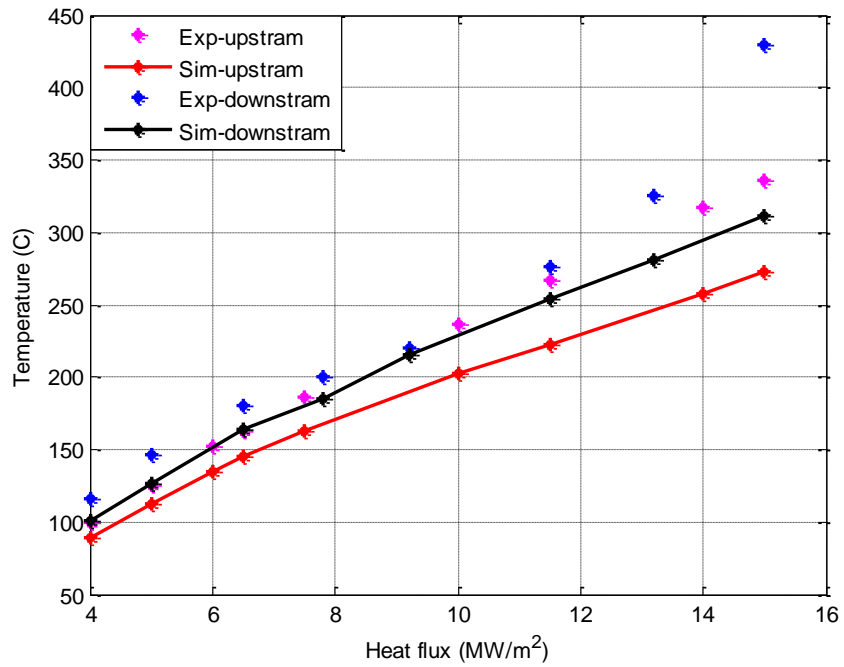


Fig 57: Div 6x6, comparison of temperatures computed with Transition boiling model (solid line) with the experimental data (symbols) for different heat fluxes and inlet velocities.

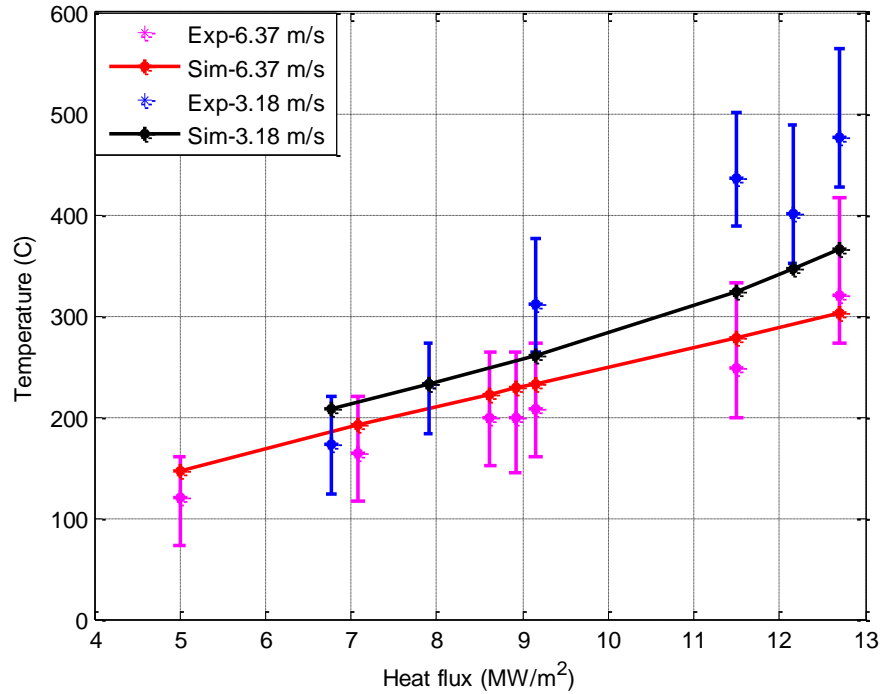


Fig 58: Mk1, comparison of temperatures computed with Transition boiling model (solid line) with the experimental data (symbols) for different heat fluxes and inlet velocities.

In the next section a comparison of the Rohsenow with the Transition boiling model is made, which will help us seeing the advantages of using transition boiling model, and also a comparison is made with the results that are obtained by J. Milnes [19].

#### 4.2.2.2.3. Comparison of results

Figure 59 shows a comparison of results between the Rohsenow and the Transition boiling model with respect to the experimental data

From figure 59 it can be observed that the experimental data have two different slope changes as explained in chapter 2. This qualitative shape is followed by the Transition but not the Rohsenow boiling model. Though quantitatively the errors obtained in the two models can be similar, we believe that the model to be selected to explain the nature of a process should be able to give the performance of the system quantitatively and also qualitatively. The superior qualities of the transition boiling model for predicting the thermal performance of the Hypervapotron comes as the model follows different correlations for each boiling regime, covering a range much larger than the Rohsenow one. The results obtained using Transition boiling model follows the general behavior of the performance curves predicted by the experiments, so it can be assumed that the boiling physics described by this model is much closer to the experiments.

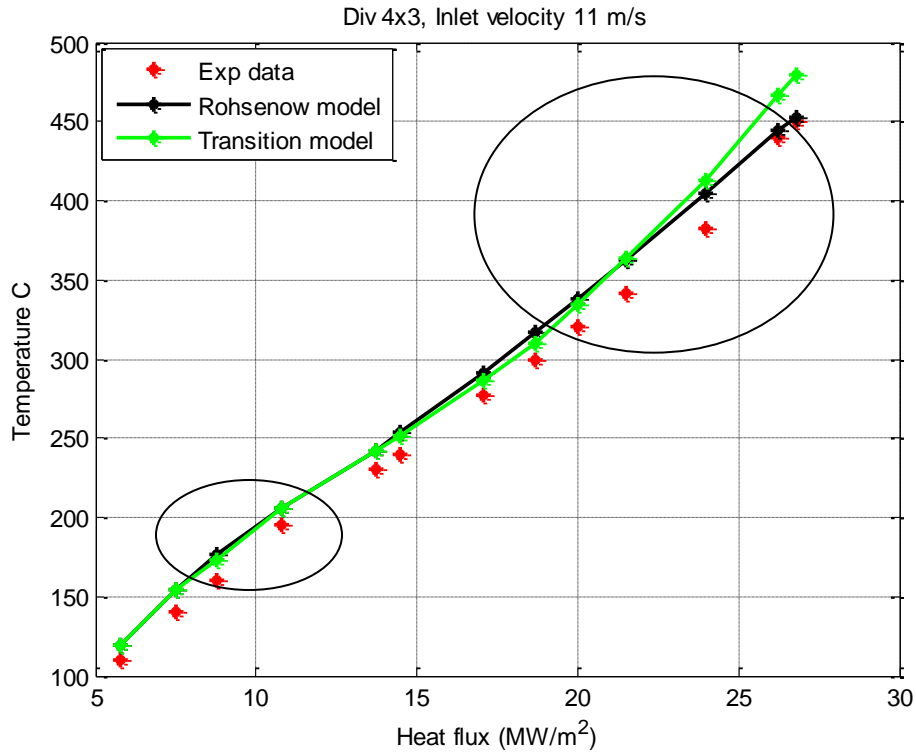


Fig 59: Comparison of results between Rohsenow model, Transition boiling model with experimental data, for Div 4×3 geometry and 11 m/s inlet velocity.

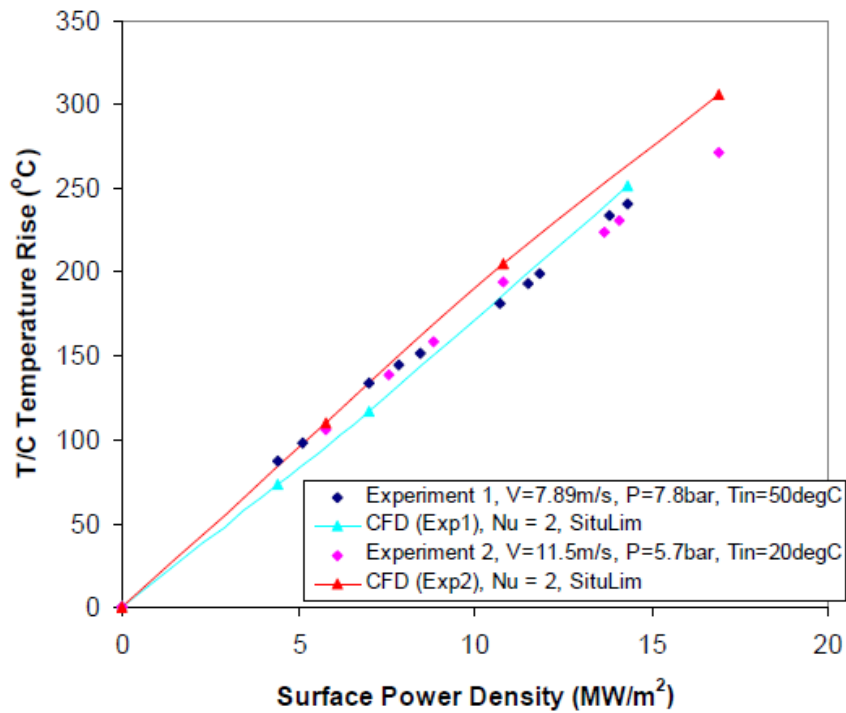


Fig 60: Performance of boiling model against Div 4×3mm HV [19]

Figure 60 shows for the above case simulations performed by J.Milnes, which was reported in his thesis [19]. For the 11 m/s inlet velocity case he only compares the data till the nucleate boiling regime as his model is only capable of doing the analysis until that regime. We believe that the results obtained from the above analysis are superior in two senses, the first is that the regime of applicability of the results is extended to hard boiling regime and second that the qualitative features of the experimental data are preserved. This is quite interesting as it gives an indication about the reliability for the modeling of sub cooled boiling and the application of CFD using a commercial tool.



# 5. Conclusions

This section presents our conclusions drawn from the analysis performed on the Hypervapotron, and also proposes some areas of future study.

## 5.1. Summary and Conclusions

The study conducted in this thesis deals with the estimation of the thermal performance of Hypervapotron device, which is a heat sink heated from one side for handling very high heat fluxes to cool a number of fusion reactor components. Very high heat transfer coefficients are achieved by using water as a coolant in forced convection subcooled boiling regime. Moreover, the Hypervapotron device has fins and cavities that are placed transverse to the direction of the fluid flow to maximize the heat transfer capability.

To assess the thermal performance of the Hypervapotron two commercial CFD codes are used to test four boiling models. The commercial CFD codes used are ANSYS FLUENT 13 and STAR-CCM+ 7.02 and the four boiling models tested are

1. Rensselaer Polytechnic institute model (RPI model) as in ANSYS FLUENT
2. Bergles and Rohsenow model (BR model), developed as an UDF in ANSYS FLUENT
3. Rohsenow boiling model as in STARCCM+
4. Transition boiling model as in STARCCM+

Among these models 1, 3 and 4 does complete 2 phase flow analysis, which means they account for both liquid and vapor, whereas 2 adopts an ad-hoc prescription for the increase in Heat Transfer Coefficient in the subcooled boiling region, and it only solves single phase flow equations. Thus the computational cost of simulations done by the BR model will be less compared to that of the other models.

Before using these models on the complex Hypervapotron geometry, they have been tested on the simpler Flat channel geometry. The key results obtained from these tests are reported below

- All the tests conducted using RPI model and FLUENT using the data from Efremov institute for Flat channel never converged whenever there is a formation of vapor. The issue of robustness of the RPI model for one-side heated square ducts is now under investigation at ANSYS. So it was decided not to use this model for further simulations.

- The tests conducted using BR model as an UDF in FLUENT and data from Efremov institute for Flat channel show some promising results for low to moderate heat fluxes where the discrepancies reported are <8 %, but the model performance worsens for high heat fluxes, and for large vapor formations the discrepancies reported are about 15 %. This behavior is due to the fact that this model only accounts for the increase in heat transfer coefficient due to subcooled boiling and solves single phase flow equations but does not account for the vapor formation, while for higher heat fluxes vapor has an important role in determining the flow characteristics and thermal behavior.
- The tests conducted using the Rohsenow model and STAR-CCM+ using the data from Efremov institute for Flat channel are very promising both qualitatively and quantitatively for all the heat fluxes and inlet velocities, with discrepancy <8 %. And this model for very high heat fluxes follows the qualitative shape of the experimental data towards the end of the heated region as it also accounts for the formation of vapor.
- The comparison made between the Rohsenow and the BR model shows that, notwithstanding its less detailed physics, the BR model may be a good engineering choice for first approximation analysis up to medium heat fluxes. In cases where more accurate information on the thermal behavior is required for all range of heat fluxes, or if the details of the flow field are considered a valuable output of the analysis, the Rohsenow model with transition to film boiling for high heat fluxes should be preferred. But looking at the range of heat fluxes that are in the experimental data base for the Hypervapotron and considering also that the physics of Hypervapotron itself relies mostly on vapor formation and condensation effects [20], it was decided to use Rohsenow model for doing simulations and if necessary to use the Transition boiling model, which itself is an extension of Rohsenow boiling model.

As a next step the tests were conducted on Hypervapotron using Efremov data and the results are summarized below

- The grid independence was not achieved even with number of cells in fluid around 10 million, and a further increase in number of cells made us to hit the RAM limits of the machine so it was decided not to run the simulations using these data and use the data from JET where the geometry used smaller by a factor 20.

Using the data from JET several simulations were conducted. The conclusions from the analysis are summarized below

- The tests conducted using Rohsenow model and STAR-CCM+ and data from JET for Hypervapotron are very promising. Quantitatively, the discrepancies reported for all the test cases are about 10%, for a given set of free parameters derived using one particular

case. Qualitative features using this boiling model are good till the nucleate boiling regime only.

- The tests conducted using Transition boiling model and STAR-CCM+ with experimental data from JET for Hypervapotron are very promising, both quantitatively and qualitatively. The discrepancies reported for all the test cases are either better or equal to the Rohsenow boiling model. This model gives us confidence on using commercial CFD codes for predicting the thermal performance of the Hypervapotron as these results follow the qualitative shape of the experimental data of the Hypervapotron.

Finally from the analysis conducted on Hypervapotron, it is concluded that the simulations performed using the boiling models can predict the performance in nucleate as well as hard boiling regions, which is very important as this type of CFD analysis provides a designer with important information about the flow distribution and heat transfer in two-phase flow problems including boiling, accounting cooling in between various boiling regimes.

## **5.2. Future work**

As a future further work on Hypervaporon geometry several things may be done such as, doing the optimization of geometry in terms of teeth height, spacing and channel width. Also several other designs such as screw tubes and holotrons can be tested and their performance can be evaluated with respect to Hypervapotron geometry.

A detailed physics of Hypervapotron using simulations can be studied (which allows us to get deeper understanding regarding the core physics, and allows us to optimize the geometry) to see the condensation and evaporation phenomenon occurring in the slots, but it requires very small time steps and lot of computational time.

# References

1. M.Merola et al., ITER plasma-facing components, *Fusion Engineering and Design* 85 (2010) 2312–2322.
2. N. KURUL, M.Z. PODOWSKI, “Multidimensional Effects in Forced Convection Subcooled Boiling,” 9th International Heat Transfer Conference, Jerusalem, Israel 1-BO-04 (1990) 21-26.
3. A.E. Bergles and W.M. Rohsenow, The determination of Forced convection surface boiling heat transfer, *Journal of Heat Transfer* 86 (1964) 365-372.
4. STAR-CCM+ version 7.02 user’s guide, CD-apdapco.inc. (2012).
5. G.P.Celata, Recent achievements in the thermal hydraulics of high heat flux components in fusion reactors, *Experimental Thermal and Fluid Science* 7 (1993) 263-278.
6. F.Escourbiac, A.Durocher, A.Grosman, F.Cismondi, X.Courtois, J.L.Farjon, J.Schlosser, M.Merola, R.Tivey, Qualification, Commissioning and in situ monitoring of high heat flux plasma facing components, *Fusion Engineering and Design* 82 (2007) 1730–1738.
7. R.A. Pitts, S. Carpentier, F. Escourbiac, T. Hirai, V. Komarov, A.S. Kukushkin, S. Lisgo, A. Loarte, M. Merola, R. Mitteau, A.R. Raffray, M. Shimada, P.C. Stangeby, Physics basis and design of the ITER plasma-facing components, *Journal of Nuclear Materials* 415 (2011) 5957-5964.
8. J. Schlosser, F. Escourbiac, M. Merola, B. Schedler, P. Bayetti, M. Missirlian, R. Mitteau, I. Bobin-Vastra, Flat Tile Armour Cooled by Hypervapotron Tube: a Possible Technology for ITER, *Physica Scripta T111* (2004) 199–202.
9. <http://www.iter.org/>
10. <http://www.efda.org/jet/>
11. <http://www-drfc.cea.fr/gb/cea/ts/ts.htm>
12. A.R. Raffray, et al., Critical heat flux analysis and R&D for the design of the ITER divertor, *Fusion Engineering and Design* 45 (1999) 377–407.
13. J. Schlosser, et al., Technologies for ITER divertor vertical target plasma facing components, *Nuclear Fusion* 45 (2005) 512–518.
14. C.B.Baxi. Comparison of Swirl Tube and Hypervapotron for Cooling of ITER Divertor. Proceedings of the 16th IEEE/NPSS Symposium on Fusion Engineering, Champaign, IL (1995).
15. I.Smid, J.Schlosser, J.Boscary, F.Escourbiac, G.Vieider, Comparison between various thermal hydraulic tube concepts for the ITER divertor, *Fusion Technologies* (1996) 263-266.
16. J. Schlosser, J; Boscary, F. Escourbiac, M. Merola, G. Vieider, Thermal hydraulic design of high heat flux elements for controlled fusion, 15th IUT NHTC Turin (1997) 45-59.

17. C. Beurtheret, Transfert de flux superieur a  $1\text{kW}/\text{cm}^2$  par double changement de phase entre une paroi non isotherme et un liquide en convection forcee, Proceedings of the Fourth International Heat Transfer conference, Versailles France (1970).
18. C. Baxi, H.Falter, Analytical prediction of thermal performance of Hypervapotron and its application to ITER, Proceedings of the 18th SOFT, Fusion Technology (1992) 186–190.
19. Joseph Milnes, Computational Modelling of the Hypervapotron Cooling Technique for Nuclear Fusion Applications, PhD thesis (2010).
20. G.Cattadori, G.P.Gaspari, G.P.Celata, M.Cumo, A.Mariani, G.Zummo, Hypervapotron Technique in Subcooled Flow Boiling CHF. Experimental Thermal and Fluid Science 7 (1993) 230 – 240.
21. F. Escourbiac , J. Schlosser, M. Merola, I. Bobin Vastra, Experimental optimization of a Hypervapotron concept for ITER plasma facing components, 22nd Symposium on Fusion Technology 66–68 (2003) 301–304.
22. Peipei Chen, Ty A.Newell, Barclay G.Jones, Heat transfer characteristics in subcooled flow boiling with Hypervapotron, Annals of Nuclear Energy 35 (2008) 1159–1166.
23. Baxi, B., Falter H. (1992). A Model for Analytical Performance Prediction of Hypervapotron. In: Proceedings for the 5th International Topical Meeting on Nuclear Reactor Thermal Hydraulics, Salt Lake City, Utah (1992).
24. S. Pascal-Ribot, A.F.Saroli, M.Grandotto, P.Spitz, F.Escourbiac, 3D numerical simulations of Hypervapotron cooling concept. Fusion Engineering and Design 82 (2007) 1781–1785.
25. N. Seiler, O.Simonin, J.M.Seiler, S.Mimouni, P.Gardin, Advanced results in the modelling and the computation of heat transfer at jet impingement, in: Proceedings of the Fifth International Conference of Multiphase Flow, ICMF'04, Yokohama, Japan (2004).
26. R.M. Podowski, D.A. Drew, R.T. Lahey, M.Z. Podowski, Mechanistic modeling of CHF in forced-convection subcooled boiling, International conference on convective flow, Munich, Germany (1997).
27. D.L.Youchison, M.A.Ulrickson, J.H.Bullock, Two-Phase Computational Fluid Dynamics Analysis of a Hypervapotron Heatsink for ITER First Wall Applications, Fusion Engineering (2009) 1 – 4.
28. D.L.Youchison, M.A.Ulrickson, J.H.Bullock, A Comparison of Two-Phase Computational Fluid Dynamics Codes Applied to the ITER First Wall Hypervapotron, Plasma Science, IEEE Transactions (2010) 1704-1708.
29. D.L.Youchison, M.A.Ulrickson, J.H.Bullock, "Prediction of Critical Heat Flux in Water-Cooled Plasma Facing Components using Computational Fluid Dynamics" Fusion Engineering (2011) 1 – 6.
30. D.L.Youchison, M.A.Ulrickson, J.H.Bullock, "Effects of Hypervapotron Geometry on Thermalhydraulic Performance", Plasma Science, IEEE Transactions 40 (2012) 653 - 658.

31. Ling Tao, Yuanlai Xie, Chundong HU, Zhimin Liu, Numerical analysis of a cooling system for high heat flux components in the neutral beam injection system, *Fusion Engineering and Design* 85 (2010) 2095–2099.
32. A.Ying, T.Waku, D.L.Youchison, R.Hunt, H.G.Zhang, M.A.Ulrickson, A subcooled boiling heat transfer predictive model for ITER EHF FW designs, *Fusion Engineering and Design* 86 (2011) 667–670.
33. J. Milnes, D. Drikakis, Qualitative assessment of RANS models for Hypervapotron flow and heat transfer, *Fusion Engineering and Design* 84 (2009) 1305–1312.
34. J. Milnes, A.Burns, D. Drikakis, Computational modelling of the Hypervapotron cooling technique, *Fusion Engineering and Design* 87 (2012) 1647–1661.
35. Zhongwei Wang, Yuntao Song, Shenghong Huang, Design of the Hypervapotron module for the EAST device, *Fusion Engineering and Design* 87 (2012) 868–871.
36. Falter, H.D., Deschamps, G.H., Hemsworth, R.S., Martin, D., Massmann, P. Test of Divertor Elements, JET Divisional Note, JET-DN-C(91)93.
37. M.Rödiger, M.Akiba, P.Chappuis, R.Duwe, M.Febvre, A.Gervash, J.Linke, N.Litounovsky, S.Suzuki, B.Wiechers, D.L.Youchison, Comparison of electron beam test facilities for testing of high heat flux components, *Fusion Engineering and Design* 51/52 (2000) 715–722.
38. I. Mazul, et al., Russian development of enhanced heat flux technologies for ITER first wall, *Fusion Engineering and Design* 87 (2012) 437–442.
39. Altmann, H., Falter, H., Hemsworth, R., Martin, D., Papastergiou, S., Tivey, R. A comparison between Hypervapotron and Multitube high heat flux beam stopping elements. In: *Proceedings for the 13<sup>th</sup> IEEE/NPSS Symposium on Fusion Engineering*, Knoxville, TN (1989) 931 – 936.
40. Massmann, P., Falter, H.D., Deschamps, G.H. Test of a Narrow Channel Vapotron (4mm Fins, 3mm Water Channel), JET Divisional Note, JET-DN-C(91)96.
41. Ciric, D., Akiba, M., Falter, H-D., Martin, D., Sato, K., Yokoyama, K. Design Issues and Fatigue Lifetime of Hypervapotron Elements of the JET Neutral Beam Injectors, In: *Proceedings for the 18<sup>th</sup> IEEE/NPSS Symposium on Fusion Engineering*, Albuquerque, NM, USA (1999).
42. <http://www.cfd-online.com/Wiki/Codes>.
43. <http://www.ansys.com/Products/Simulation+Technology/Fluid+Dynamics/Fluid+Dynamics+Products/ANSYS+Fluent>.
44. [http://www.cd-adapco.com/products/star\\_ccm\\_plus/](http://www.cd-adapco.com/products/star_ccm_plus/).
45. <http://www.ansys.com>.
46. <http://www.ansys.com/Products/Simulation+Technology/Fluid+Dynamics>
47. ANSYS-FLUENT-13.0, User's guide, ANSYS.inc. (2010).
48. S.V. Patankar, *Numerical Heat Transfer and Fluid Flow*, Hemisphere, Washington DC (1980).

49. G. H. YEOH, J. Y. TU., Modelling subcooled boiling flows, Nova Science Publishers Inc., New York (2009).
50. J.H. Ferziger, M.Peric, Computational methods for Fluid dynamics, Springer, London (2002).
51. M.Ishii, T.Hibiki, Thermo-Fluid dynamics of Two-phase flow, Springer, New York (2011).
52. Shankar Subramaniam, Lagrangian-Eulerian methods for multiphase flows, Progress in Energy and Combustion Science 39 (2013) 215-245.
53. S.Narumanchi, A.Troshko, D.Bhatathan, V.Hassani, Numerical simulations of nucleate boiling in impinging jets: Applications in power electronics cooling, International Journal of Heat and Mass Transfer 51 (2008) 1-12.
54. N.I. Kolev, Multiphase Flow Dynamics 2, Springer, Berlin (2011).
55. F.J. Moraga, F.J. Bonetto, R.T. Lahey, Lateral forces on spheres in turbulent uniform shear flow, International Journal of Multiphase Flow 25 (1999) 1321–1372.
56. Seong-Su Jeon, Seong-Jin Kim, Goon-Cherl Park, CFD Simulation of Condensing Vapor Bubble using VOF Model, World Academy of Science, Engineering and Technology 60 (2009) 209-215.
57. FANG Xiande, SHI Rongrong, ZHOU Zhanru., Correlations of Flow Boiling Heat Transfer of R-134a in mini channels: Comparative Study, Energy science and technology 1 (2011) 1-15.
58. W.M. Rohsenow , A Method of Correlation Heat Transfer Data for Surface Boiling of Liquid, Transactions of ASME 74 (1952) 969-976.
59. K. E. GUNGOR , R. H. S. WINTERTON, A general correlation for flow boiling in tubes and annuli, J. Heat Mass Transfer 29 (1986) 351-358.
60. Robert W.Bjorge, Garry R.Hall, W.M.Rohsenow, Correlation of forced convection boiling heat transfer data, J. Heat Mass Transfer 25 (1982) 753-757.
61. N. KURUL, M.Z. PODOWSKI, “Multidimensional Effects in Forced Convection Subcooled Boiling,” 9th Intl. Heat Transfer Conf., Jerusalem, Israel 1-BO-04 (1990) 21-26.
62. M.Z. PODOWSKI, “Multidimensional Modeling of Two-Phase Flow and Heat Transfer,” Intl. J. of Numerical Methods for Heat and Fluid Flow 18 (2008) 491-513.
63. D.C. Wilcox, Turbulence modeling for CFD, DCW Industries.inc., California (1993).
64. C.T.Crowe, T.R.Troutt, J.N.Chung, Numerical models for two-phase turbulent flows, Annual Review of Fluid Mechanics 28 (1996) 11-43.
65. Bostjan Koncar, Iztok Tiselj, Influence of near wall modeling on boiling flow simulation, Nuclear Engineering and Design 240 (2010) 275-283.
66. C. Jayatillaka, The influence of Prandtl Number and Surface Roughness on the Resistance of the Laminar Sublayer to Momentum and Heat Transfer, Prog. Heat Mass Transfer (1969) 193-321.

67. P.Domalapally, CFD analysis of flow boiling in the ITER first wall, *Fusion engineering and design* 87 (2012) 556-560.
68. C.I.Roy, Review of code and solution verification procedures for computational simulation, *Journal of computational physics* 205 (2005) 131-156.
69. P.J.Roache, P.M.Knupp, Completed Richardson extrapolation, *Communications in numerical methods in engineering* 9 (1993) 365-374.
70. P.J.Roache, Perspective: A method for uniform reporting of grid refinement studies, *Journal of fluids engineering* 116 (1994) 405-413.



# **Appendix A**

**Computation of JT-60SA TF coil temperature margin using the 4C code**



## Computation of JT-60SA TF coil temperature margin using the 4C code

R. Bonifetto<sup>a</sup>, P.K. Domalapally<sup>a</sup>, G.M. Polli<sup>b</sup>, L. Savoldi Richard<sup>a</sup>, S. Turtu<sup>'b</sup>, R. Villari<sup>b</sup>, R. Zanino<sup>a,\*</sup>

<sup>a</sup> Dipartimento di Energetica, Politecnico di Torino, I-10129 Torino, Italy

<sup>b</sup> ENEA, EURATOM Association, I-00044 Frascati, Italy

### ARTICLE INFO

*Article history:*  
Available online 9 April 2011

*Keywords:*  
Fusion reactors  
Superconducting coils  
Simulation  
ITER  
Thermal-Hydraulics  
JT-60SA

### ABSTRACT

The recently developed 4C thermal-hydraulic code, currently under validation, is used to compute the temperature margin of the superconducting NbTi toroidal field coil of the ITER satellite tokamak JT-60SA, for the nominal burn operation of the machine. Repetitive conditions in the simulation are reached after two plasma pulses. For given (computed) thermal load distribution on winding and coil case due to nuclear heating only, helium temperature  $\sim 4.4$  K at the winding inlet, reference strand, and the most recent conductor and winding layout, the computed minimum margin occurs in pancake #7 at the peak field location and turns out to be  $\sim 0.2$ – $0.3$  K above the design value of 1.2 K.

© 2011 Elsevier B.V. All rights reserved.

### 1. Introduction

Within the so-called Broader Approach signed by the EU and Japanese governments in 2007, the upgrading of the JT-60 tokamak to the JT-60SA superconducting tokamak was decided as a “satellite” facility to the International Thermonuclear Experimental Reactor (ITER). Among other components, the EU is in charge of supplying the 18 toroidal field (TF) superconducting coils, which will be made of NbTi [1].

The TF coils will be subject to different kinds of thermal loads, among which a major role will be played by the nuclear heating due to neutrons coming from D–D fusion reactions and secondary gammas [2]. These thermal loads enter the calculation of a fundamental design parameter of the TF coils, namely the so-called temperature margin  $\Delta T$ , which is defined as the difference between the current sharing temperature (or quench temperature, in the case of NbTi) and the operating temperature. In JT-60SA the minimum allowable value of  $\Delta T$  is 1.0 K after burn and a disruption event and 1.2 K for nominal burn operation [1].

The JT-60SA TF coil temperature margin for nominal burn operation was computed in [3] for the conductor/winding layout which was used as reference in that phase of the design. After that, the design was changed [4]. Here we apply the 4C thermal-hydraulic code [5], which was already applied to the quench simulation in an ITER TF coil [6] and also showed good agreement with experiment in validation exercises against ITER Toroidal Field Model Coil data [7], as well as W7-X non-planar coil data [8], to the calculation

of  $\Delta T$  in the new design of the JT-60SA TF coils; one of the nominal burn operation scenarios is considered – the double-null full-current inductive scenario [9] – in the case of purely nuclear heat load.

4C implements a model of compressible 1D supercritical helium flow in the entire winding (and in the case cooling channels, where present), coupled with 3D heat conduction in the solid structures and fed by an external cryogenic circuit which may include pumps, heat exchangers, cryolines, valves, etc. The results of 4C are presented and compared with those of previous analyses, where possible.

### 2. Problem definition

#### 2.1. Coil and conductor

The 3D structure of a JT-60SA TF coil is discretized in the poloidal direction with a series of cuts as shown in Fig. 1. On each cut the transverse transient 2D heat conduction problem is solved by finite elements, coupled to transient 1D advection/diffusion in the third direction, along each pancake (the case cooling channels are included in the 4C model but they are not used in the present case, see [10,11], so that we assume them to be adiabatic here); we use cuts of two different cross sections here, as shown in Fig. 2, which is adequate in the case at hand (each cut could have a different cross section, if needed).

The JT-60SA TF coils will be wound in double pancakes, using rectangular NbTi conductors (12 pancakes P1–P12 hydraulically in parallel, of 6 turns each, with L316 SS jacket) as shown in Fig. 3. The main conductor and strand data used for the present analysis are given in Table 1. (While different types of strands are

\* Corresponding author. Tel.: +39 0110904490.  
E-mail address: [roberto.zanino@polito.it](mailto:roberto.zanino@polito.it) (R. Zanino).

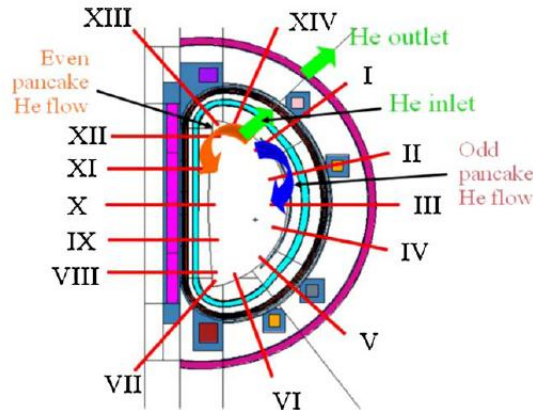


Fig. 1. Sketch of the JT-60SA coil system highlighting 2D cut locations and numbering (I–XIV) used in this paper, as well as He inlet/outlet locations and flow direction in odd/even pancakes.

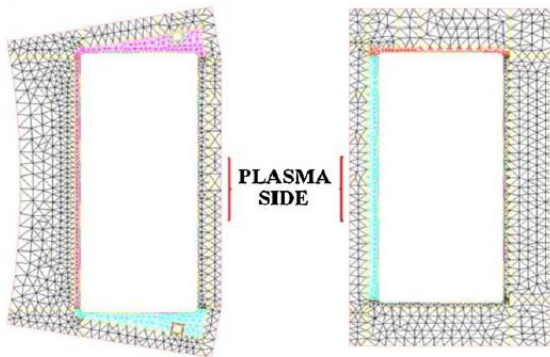


Fig. 2. Geometry of 2D cuts and example of corresponding finite element discretization. Inboard cuts (VII–XIII) with case cooling channels shown on the left; outboard cuts (XIV, I–VI) shown on the right (case cooling channels should be attached on the plasma side surface [10], but are not shown as not relevant here).

still under consideration [12,13], we shall concentrate here on the Luvata strand, that has been used in the manufacture of the two sample prototypes tested in the Sultan facility [14].) The strand critical current density (non Cu) is parameterized here according to the scaling in [15] and using the following values for the parameters:  $C_0 = 3.355 \times 10^{11}$  AT/m<sup>2</sup>,  $B_{C20} = 15.19$  T,  $T_{C0} = 8.907$  K,  $\alpha = 1.67$ ,  $\beta = 1.88$ ,  $\gamma = 2.249$ ,  $n = 1.7$ , which were obtained from the strand characterization [11]; a value of the *cable n* is also needed here and it was assumed equal to 50. Two types of insulation are treated differently by 4C: 1 mm glass-epoxy around each conductor + 1 mm glass-epoxy sheet between double pancakes are treated as thermal

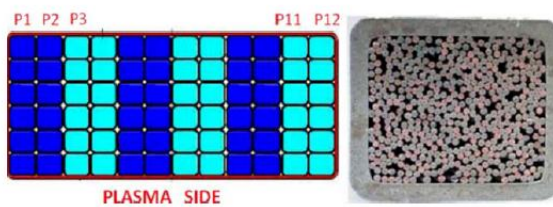


Fig. 3. Left: sketch of the JT-60SA TF coil winding layout (numbering and "plasma side" refer to an inboard cut, e.g. cut X). Right: cross section of a JT-60SA conductor sample tested in SULTAN [13].

Table 1  
Main JT-60SA conductor and strand parameters used here.

Conductor area	18 mm × 22 mm
Pancake hydraulic length	114 m
Jacket thickness	2 mm
Number of SC/Cu strands	324/162
Void fraction	32%
Strand diameter	0.81 mm
Cu/non-Cu	1.6

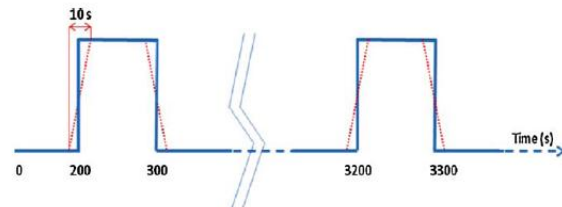


Fig. 4. Nuclear heat load during two consecutive pulses: ideal (solid), approximate used here (dashed).

resistance, i.e., they are not discretized; 3 mm polyimide-kapton between winding and case + glass-epoxy filler/ground insulation are homogenized with volume-averaged properties and discretized by finite elements.

The conductor friction factor  $f$  determines the relation between mass flow rate and pressure drop across the winding. Here we use for  $f$  the correlation  $f = 6.1 \times Re^{-0.51}$  [16] where  $Re$  is the Reynolds number.

### 2.2. Scenario and drivers

We consider the double null full-current inductive operating scenario, as defined in [9], with constant transport current  $I_{op} = 25.7$  kA in the TF coils. In this scenario, plasma pulses last for  $\tau_1 = 100$  s (flat top) and are repeated every  $\tau_2 = 3000$  s. The corresponding nuclear heat load evolution is shown in Fig. 4.

The resulting distribution of the peak magnetic field intensity (on the respective conductor cross section), computed along the most critical pancakes P6 and P7 by means of OPERA 3D TOSCA, a magnetostatic 3D code based on the analytical integration of the Biot–Savart law, is shown in Fig. 5. We assume this distribution as constant in time, since the effect of the other coils on the field in the TF is practically negligible.

The nuclear heat load distribution in the coil case (see Fig. 6a) and winding (see Fig. 6b) at the plateau of each pulse has been recently computed by 3D neutronic analysis [17]. (Note that

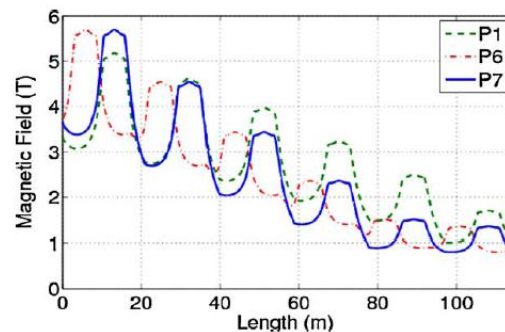


Fig. 5. Peak field maps computed along P1, P6 and P7 (maximum over whole coil ~5.7 T).



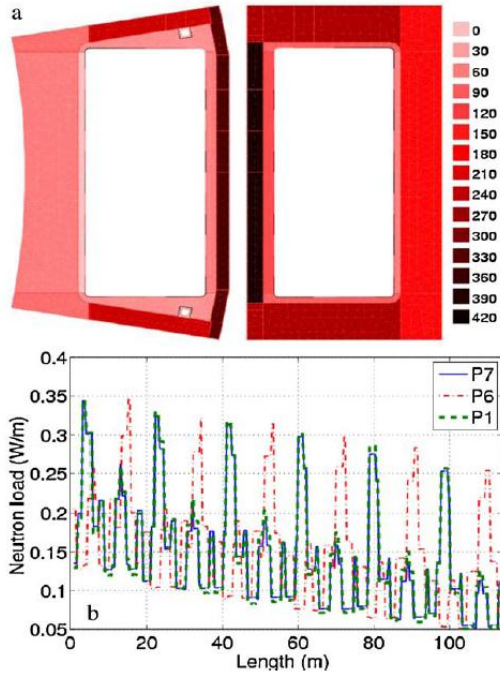


Fig. 6. Plateau nuclear heating: (a) on case ( $W/m^3$ ); (b) along P7 (solid), P6 (dash-dotted) and P1 (dashed) ( $W/m$ ). Nominal case ( $F=1$ ).

although the load on the coil case is symmetric, we cannot reduce the size of the computational domain because of opposite He flow directions in neighboring pancakes, see Fig. 1.) The nuclear load is assumed to be the only driver for the transient; AC losses in the winding and eddy currents in the case are neglected in this paper following [3], meaning however that the computed  $\Delta T$  is not fully conservative and could be somewhat underestimated. The simulation follows a series of pulses, until a fully repetitive thermal behavior of the coil is reached.

2.3. Cryogenic circuit

For the circuit feeding the He coolant to the coil reference operating conditions were defined in [18], then updated in [19]: pressure  $p_{op} \sim 5$  bar and temperature  $T_{in} \sim 4.4$  K at the winding inlet, mass flow rate  $(dm/dt)_p \sim 4$  g/s/pancake.

In the model we adopt a simple circuit including only the essential components, as shown in Fig. 7, namely: the TF coil itself, the cold and hot cryolines connecting it to the two heat exchangers HXFluid with the He bath, upstream and downstream of the pump. The parameters characterizing the Dymola model [5] of each component are given in Table 2 and were chosen following [19], scaling back the pipe size in order to account for a single coil out of 18. Before applying the nuclear heat pulses to winding and case, the circuit is run without external load until it reaches a slowly varying state, approximately reproducing the constraints on  $p_{op}$ ,  $T_{in}$  and  $(dm/dt)_p$ ; this is then used as initial condition for the simulation.

3. Results

Results are presented both for the case of nominal heat load (safety factor  $F=1$ ), as shown in Fig. 6, and for the case of safety factor  $F=1.8$ . The convergence of the results was guaranteed through dedicated studies, proving insensitivity to the main numerical

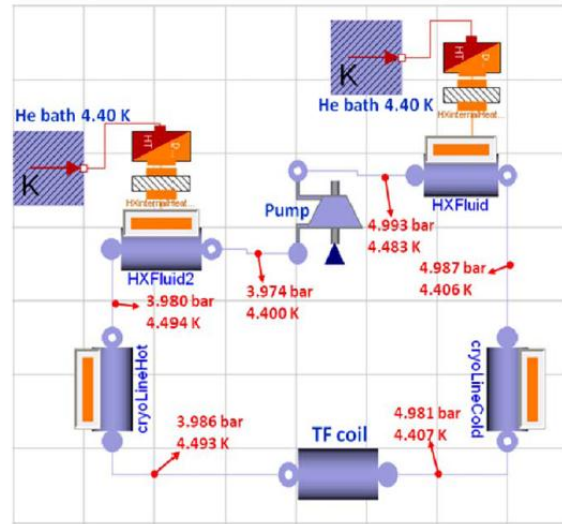


Fig. 7. Schematic of the cryogenic circuit adopted for the present simulations and thermodynamic states before the application of the load.

Table 2

Main parameters used in the Dymola model of the cryogenic circuit components adopted here.

Component	Parameter	Value
Pump	Flow rate @ zero pressure increase (kg/s)	0.062
	Pressure increase at zero flow (MPa)	0.5
	Length of single tube (m)	1.5
HXFluid	# of tubes	10
	Diameter (m)	0.0178
	Heat transfer coeff. ( $W/m^2 K$ )	500
	Length (m)	35
Cold cryoline	Diameter (m)	0.024
	Length (m)	51
Hot cryoline	Diameter (m)	0.024
	Length (m)	51

parameters in the model: time step, # of nodes/pancake, # of triangles/cut, # of cuts.

The evolution of the outlet He temperature in Fig. 8 shows that it is sufficient to run the simulation for a total time  $\sim 4000$  s  $< 2 \times \tau_2$ , as the transient after the third pulse is already repetitive. The peak in the outlet temperature is reached  $\sim 150$  s after the end of the heat pulse; this time is shorter than the transit time of He along the pancake ( $\sim 450$  s) because of relatively strong inter-turn and inter-layer thermal coupling.

Arguably the most important result of the present paper is reported in Fig. 9. It is seen that pancake P7 reaches the minimum

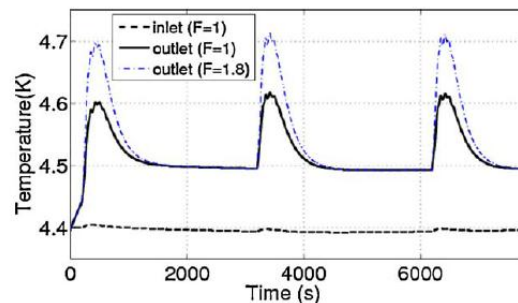


Fig. 8. Evolution of computed He temperatures at inlet and outlet of P7, for both  $F=1$  and  $F=1.8$ .

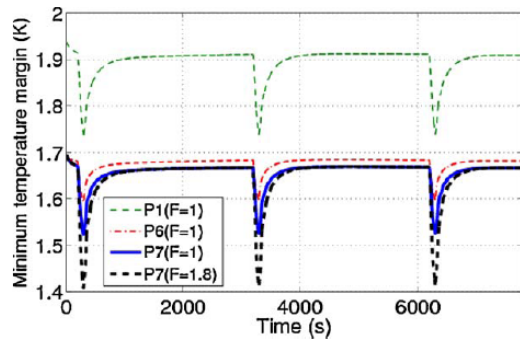


Fig. 9. Evolution of the minimum temperature margin for pancakes P1, P6 and P7 (the latter for both  $F=1$  and  $F=1.8$ ).

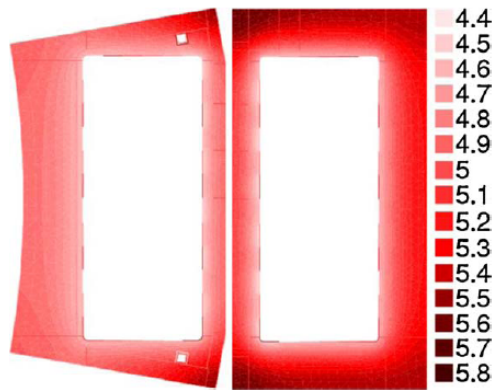


Fig. 10. Computed temperature distribution (K) at the end of the second pulse in cuts X (left) and III (right), for  $F=1$ .

$\Delta T$  of the coil,  $\Delta T_{\min} \sim 1.53$  K in the case  $F=1$  and  $\Delta T_{\min} \sim 1.41$  K in the case  $F=1.8$  (the reduction in margin directly corresponds to the temperature increase proportional to the heat load, see Fig. 8). P7 is the most critical pancake of the coil because, if compared to P6, a higher load is applied upstream of the maximum field, see Figs. 5 and 6b. The minimum  $\Delta T$  is reached at the end of the pulse and at the max field location,  $\sim 13.3$  m from the He inlet. Edge pancakes P1 and P12 correspondingly have the highest  $\Delta T$  ( $\Delta T_{\min} \sim 1.74$  K) because of lowest field (see Fig. 5), despite the highest load coming from the structures, which are in contact with P1 and P12 all along the conductor length, see Fig. 6a.

A quantitative comparison between the present work and previous analyses, e.g. [3] or [20], is not meaningful due to the different

assumptions made on the conductor in [3] or on the strand in [20]. These quantitative input differences induce also qualitative output differences: for instance, the strand scaling used in [20], combined with a magnetic field distribution somewhat different from that we use, result in the lateral pancakes being identified as the most critical ones in [20], as opposed to the central ones here.

The temperature distribution in the coil case, computed at the end of the second pulse on the two equatorial plane cuts, see Fig. 10, reflects the heat load distribution of Fig. 6a and the strong cooling effect of the He in the winding (recall that the case cooling channels have been assumed to be adiabatic here).

#### 4. Conclusions and perspective

A detailed analysis of the temperature margin of the JT60-SA TF coil, performed with the recently developed 4C code, currently under validation, shows that for given 1) thermal load distribution on winding and coil case due to nuclear heating only, 2) helium entering the winding at 4.4 K, 3) reference strand, and 4) the most recent conductor and winding layout, the computed minimum margin is  $\sim 0.2$ – $0.3$  K above the design value for nominal burn operation.

The 4C code could be profitably used for the analysis of different operating scenarios and/or design options of JT60-SA.

#### References

- [1] V. Tomarchio, et al., IEEE Trans. Appl. Supercond. 20 (2010) 572.
- [2] R. Villari, et al., Fusion Eng. Des. 84 (2009) 1947.
- [3] S. Nicollet, et al., Cryogenics 50 (2010) 18.
- [4] K. Yoshida, et al., Physica C (2010) 195, doi:10.1016/j.physc.2010.05.
- [5] L. Savoldi Richard, et al., Cryogenics 50 (2010) 167.
- [6] R. Zanino, et al., Fusion Eng. Des. 85 (2010) 752.
- [7] R. Zanino, et al., Validation of the 4C thermal-hydraulic code against 25 kA safety discharge in the ITER Toroidal Field Model Coil (TFMC), presented as paper 2-LZ-06 at ASC, Washington DC, 2010, IEEE Trans. Appl. Supercond. (2011).
- [8] R. Bonifetto, et al. Modeling of W7-X superconducting coil cool-down using the 4C code Presented as paper P4-133 at SOFT, Porto, 2010, Fusion Eng. 194 Des. (2011).
- [9] Plant Integration Document (PID), v. 2.3, JT-60SA Report, IDM # AST.D.222QVA (2009).
- [10] G.M. Polli, et al., Fusion Eng. Des. 84 (2009) 1531.
- [11] P. Barabaschi et al., JT-60SA Toroidal Field Coils Conceptual Design Report, JT60SA Report, IDM # AST.D.223N23 (2009).
- [12] L. Zani, et al., IEEE Trans. Appl. Supercond. 20 (2010) 451.
- [13] L. Muzzi, et al., IEEE Trans. Appl. Supercond. 19 (2009) 2544.
- [14] L. Muzzi, et al., IEEE Trans. Appl. Supercond. 20 (2010) 442.
- [15] L. Bottura, IEEE Trans. Appl. Supercond. 10 (2000) 1054.
- [16] M. Wanner, Pressure Drop of the W7-X Cable-in-Conduit Conductor, JT60SA Report, AST.D.2234VD1.1 (2009).
- [17] R. Villari, TFC Nuclear Heating, JT-60SA Report, IDM # BA.D.223JMT v1.1 (2010).
- [18] P. Roussel, et al., Adv. Cryog. Eng. 55 (2010) 1445.
- [19] D. Hitz, et al., Impact of mass flow rate reduction on the cryogenic system, presented at the 8th Technical Coordination Meeting, Frascati, April, 2010.
- [20] B. Lacroix, et al., Adv. Cryog. Eng. 55 (2010) 471.

# **Appendix B**

## **CFD analysis of flow boiling in the ITER first wall**





## CFD analysis of flow boiling in the ITER first wall

Phani Domalpalay<sup>a,\*</sup>, Enrico Rizzo<sup>b</sup>, Laura Savoldi Richard<sup>a</sup>, Fabio Subba<sup>a</sup>, Roberto Zanino<sup>a</sup>

<sup>a</sup> Dipartimento di Energetica, Politecnico, I-10129 Torino, Italy

<sup>b</sup> Institut fuer Technische Physik, Karlsruhe Institute of Technology, Karlsruhe, Germany

### ARTICLE INFO

Article history:  
Available online 23 February 2012

Keywords:  
Boiling  
First wall  
Two phase flow  
Computational Fluid Dynamics

### ABSTRACT

This paper compares two Computational Fluid Dynamic (CFD) approaches for the analysis of flow boiling inside the first wall (FW) of the International Thermonuclear Experimental Reactor (ITER): (1) the Rohsenow model for nucleate boiling, seamlessly switching to the Volume of Fluid (VOF) approach for film boiling, as available in the commercial CFD code STAR-CCM+, (2) the Bergles–Rohsenow (BR) model, for which we developed a User Defined Function (UDF), implemented in the commercial code FLUENT. The physics of both models is described, and the results with different inlet conditions and heating levels are compared with experimental results obtained at the Efremov Institute, Russia. The performance of both models is compared in terms of accuracy and computational cost.

© 2012 Elsevier B.V. All rights reserved.

### 1. Introduction

In ITER, the FW heat load during operations can be as high as several MW/m<sup>2</sup>, which should be removed by a proper cooling system to prevent damage of the component [1]. The proposed sink to handle this load consists of copper alloy (CuCrZr) hypervapotron or swirl tubes, which exploit the large heat transfer coefficient (HTC) characteristic of highly sub-cooled boiling [2].

In order to predict the system performance, a dedicated thermal hydraulic analysis has to be conducted, and several papers have been devoted during the last few years to this task on different geometries foreseen for the ITER first wall [3–7].

Here we test and compare two approaches, based respectively on an enhancement of the Rohsenow model [8] and on the classical Bergles–Rohsenow (BR) work [9]. The first model is available in the commercial STAR-CCM+ code, including a smooth transition to the VOF model for film boiling. We implemented the second in the FLUENT code, specifically for this work. We then compared our computed results with experimental data from Efremov Institute, Russia [10].

Although our ultimate goal is to develop predictive capabilities for the hypervapotron, we start by analyzing in some detail the simpler case of a rectangular (so-called flat) channel, heated on one side. This allows us concentrating on the details of the heat transfer model performances. Preliminary results for the hypervapotron are discussed at the end of the paper.

The layout of this work is as follows: in the next section we discuss the system geometry and meshing issues. In Section 3 we

describe the physical models. In Section 4 we present and discuss our results, in terms of both accuracy and numerical performance. To the best of our knowledge, this is the first time that the Rohsenow and BR models are critically compared for an ITER-relevant application. Also, we are not aware of an implementation of the BR model in FLUENT so far and, indeed, previous applications of FLUENT to ITER-relevant boiling problems met only limited success [6].

### 2. Geometry and mesh

Fig. 1 represents the experimental test section. It also shows the location of a set of thermocouples inserted 1.5 mm below the heated surface. Fig. 2 shows a cross-section highlighting the inner dimensions of a flat channel. In the hypervapotron case, a number of teeth are machined at the top of the fluid flow channel, along with a side channel. The hypervapotron channel dimensions are given in Fig. 3, showing cross and longitudinal sections. In both cases, the top wall is heated over a length of 100 mm, the system being otherwise thermally insulated.

For the flat-channel geometry, we tested a number of hexahedral non-uniform meshes created with the commercial mesh generator GAMBIT, ranging from 0.3 to 1.7 Mcells. We found a relative variation of the computed temperature of ~12% (using the inlet subcooling as the reference value) when the mesh size varied from 0.3 to 1.0 Mcells. This variation was reduced to ~2% when the mesh size went from 1 to 1.7 Mcells. Then, ~1 Mcells are a good compromise between reasonable grid-independence of the solution and computational cost. This size of the mesh is also comparable to that chosen in previously published works on the same subject [6,7]. For the hypervapotron, we kept the same average cell size (~0.5 mm), but we used tetrahedral cells because of the more complex flow

\* Corresponding author.

E-mail address: [phani.domalpalay@polito.it](mailto:phani.domalpalay@polito.it) (P. Domalpalay).

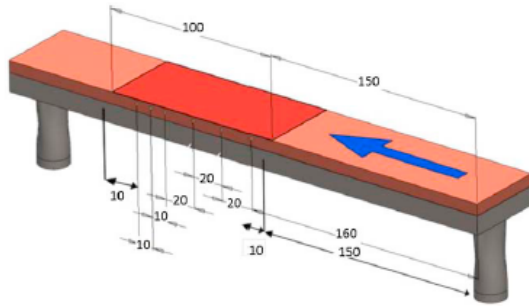


Fig. 1. 3D sketch of the experimental test section geometry (the dark region on the top marks the heated surface, all dimensions are in mm).

geometry. In both cases, left-right symmetry was assumed, i.e., the computational domain included only half of the channel.

### 3. Modeling

Typical experimental inlet conditions for the flat-channel are pressure  $p_{in} = 20$  bar, temperature  $T_{in} = 128^\circ\text{C}$  (i.e., a subcooling of  $\sim 85^\circ\text{C}$ ),  $V_{in} = 1\text{--}4$  m/s. For the hypervapotron, they were similar except for a lower inlet temperature  $T_{in} = 110^\circ\text{C}$  (i.e., a stronger subcooling of  $\sim 103^\circ\text{C}$ ). In these conditions, the flow was always turbulent (Reynolds number  $Re \sim 5 \times 10^4$  for the lowest mass-flow rate).

Both models compared in this paper are based on the Navier–Stokes equations. Turbulent flow was accounted for by the realizable  $k$ -epsilon model, with wall-functions to handle  $y^+ \sim 30$  near the wall, where  $y^+$  is defined in [11]. In the experimental apparatus the entrance and exit ducts are orthogonal to the fluid flow in the main channel. This provides a sharp change in direction of the flow field which helps increasing turbulence. Moreover, the heated region starts  $\sim 17$  hydraulic diameters after the inlet section. Consequently, we imposed fully developed flow conditions. STAR-CCM+ solves the two-phase flow field with the Eulerian approach combined with the Rohsenow model for nucleate boiling smoothly transitioning to VOF for film boiling. It includes gravity and surface tension. In contrast, FLUENT consider a single fluid (liquid), with an ad hoc prescription for the HTC in the subcooled boiling region, following the BR treatment [9]. Surface tension is not present in the model and, due to the limited density variation with temperature in the liquid phase, gravity is also not included.

Both codes were run with a pressure-based segregated solver [12]. We run STAR-CCM+ mostly in steady-state mode. A few tests (including power level higher than the experimental CHF) showed

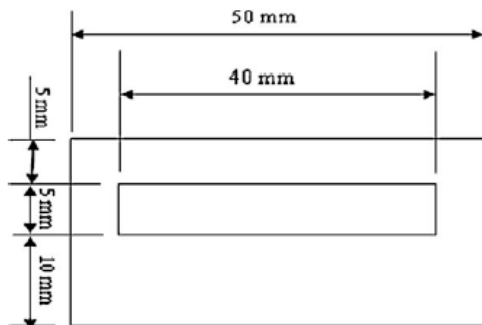


Fig. 2. Flat-channel cross-section.

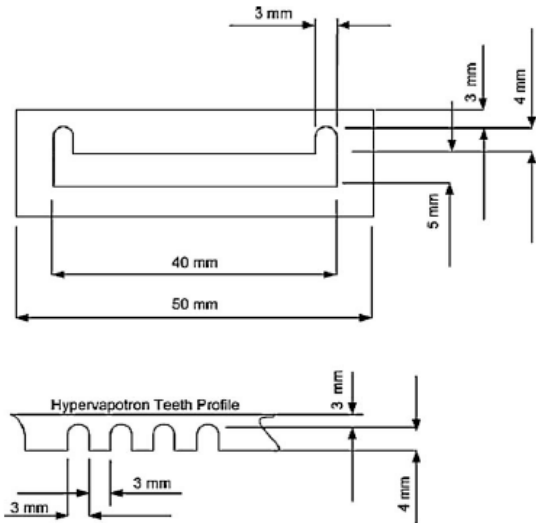


Fig. 3. Cross (top) and longitudinal (bottom) sections of the hypervapotron channel.

that transient runs led to the same solution, with a higher computational cost. In contrast, we needed to run FLUENT in transient mode, since in steady state mode it accepts prescription on the HTC at the first iteration only.

The BR model is computationally less expensive than the Rohsenow one. In fact, solving for one phase only, it saves both the memory allocation needed to store the vapor-related information and the iterations required to solve the vapor equations. Furthermore, the single-phase approach avoids sharp variations in the fluid properties, with beneficial effects on the convergence.

#### 3.1. STAR-CCM+/Rohsenow model

The Rohsenow model implemented in STAR-CCM+ employs an empirical correlation to calculate the surface heat flux due to boiling [8]. This is given by

$$q_{bw} = \mu_l h_{lat} \sqrt{\frac{g(\rho_l - \rho_v)}{\sigma}} \left( \frac{C_{pl}(T_w - T_{sat})}{C_{qw} h_{lat} Pr_l^{n_p}} \right)^{3.03} \quad (1)$$

where  $\mu_l$  is the liquid viscosity,  $C_{pl}$  is the liquid specific heat,  $h_{lat}$  is the latent heat,  $Pr_l$  is the liquid Prandtl number,  $\rho_{l(v)}$  is the liquid (vapor) density,  $T_{w(sat)}$  is the wall (saturation) temperature,  $\sigma$  is the surface tension,  $g$  is the gravity acceleration,  $n_p$  is the Prandtl number exponent and  $C_{qw}$  is a constant dependent on the liquid/surface combination. The vapor mass generation rate is given by

$$\dot{m}_{ew} = \frac{C_{ew} q_{bw}}{h_{lat}} \quad (2)$$

where  $C_{ew}$  is the heat flux fraction used to create vapor bubbles. The rate of evaporation and condensation is calculated using the formula

$$\dot{m}_{ec} = \frac{C_{HTC \times Area} \cdot (T - T_{sat})}{h_{lat}} \quad (3)$$

where  $C_{HTC \times Area}$  ( $\text{W}/\text{m}^3 \text{K}$ ) is the HTC between a bubble and the surrounding liquid times the contact area per unit volume, and  $T$  is the temperature of the mixture.

A VOF approach is used to track the liquid vapor interface in the film boiling regime. Switching between nucleate and film boiling is tuned by a critical value of the vapor fraction, called  $\alpha_{fb}$ .



**Table 1**  
Values adopted for the free parameters in the STAR-CCM+ boiling model.

$C_{qw}$	$C_{ew}$	$CHFC_{Area}$	$\alpha_{fb}$	$n_p$	$S_{ct}$
0.01	0.01	$5 \times 10^6$	0.3	1	0.5

An additional tunable parameter is the turbulent Schmidt number  $S_{ct}$ , the ratio of eddy viscosity to eddy mass diffusivity [14]. Overall, there are six user provided input parameters. Here we use the values suggested in [6,7], see Table 1, determined best-fitting the experimental database.

3.2. FLUENT/BR model

Bergles and Rohsenow [9] suggest that subcooled boiling heat transfer may be described by:

$$q_{total} = (q_{FC}^2 + (q_{FDB} - q_0)^2)^{1/2} \tag{4}$$

where  $q_{FC}$  and  $q_{FDB}$  are the forced convection and fully developed boiling heat flux, and  $q_0$  is the flux at the onset of nucleate boiling. The boiling curve predicted by (4) merges smoothly with the forced convection curve for  $q_{FDB} - q_0$ , and approximates accurately the fully developed curve for  $q_{FDB} \gg q_{FC}$ ,  $q_0$ , see Fig. 4.  $q_{FC}$  is given by the single-phase wall heat transfer model built in FLUENT. A series of tests showed that its value can be estimated by the classical Dittus–Boelter equation within 15% accuracy.  $q_{FDB}$  is given by

$$q_{FDB} = \left( \frac{T_w - T_{sat}}{C_s} \right)^3 \tag{5}$$

where  $C_s$  is a free parameter. In principle, also the exponent in Eq. (5) must be input by the user. However, the value 3 is strongly recommended [9], and we kept it frozen. A discussion of  $q_0$  can be found in [5].

FLUENT adopts a law-of-the-wall for the near wall temperature profile  $y^*$  (Eq. (6))

$$T^* = \frac{(T_w - T_p) \rho_c \mu_p^{1/2}}{\dot{q}} = \begin{cases} Pr y^* + \frac{1}{2} Pr \frac{C_\mu^{1/4} k_p^{1/2}}{\dot{q}} U_p^2 & (y^* < y_T^*) \\ Pr_t \left[ \frac{1}{\kappa} \ln(Ey^*) + P \right] & (y^* > y_T^*) \end{cases} \tag{6}$$

where the subscript “p” means that the corresponding quantity is evaluated at the center of the near-wall cell.  $U$  is the flow velocity,  $\kappa$  is the von Karman constant ( $\kappa = 0.4187$ ),  $E$  is an empirical constant ( $E = 9.793$ ) and  $P$  is defined in [13]. The dimensionless distance  $y^*$

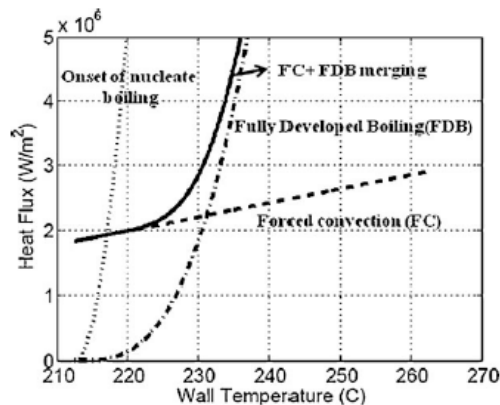


**Fig. 4.** Forced convection (dashed), onset of nucleate boiling (dotted), fully developed boiling (dash-dotted) heat fluxes, together with the BR merging (solid). Data are for the operating pressure of 20 bar.

**Table 2**  
Free parameters in the FLUENT/BR model.

	Value	Sensitivity
$Pr_t$	0.1	0.80
$C_s$	$8.4e-3$	0.96

is defined in [15]. It serves the purpose of extending the wall function applicability to non-equilibrium boundary layers. In the case of slowly varying flow properties, as the one we are interested in, we have  $y^* = y^+$ . The critical value  $y_T^*$  corresponds to the intersection of the linear and logarithmic layers.

$Pr_t$  is the energy Prandtl number, which we used to tune the model as follows:  $Pr_t$  was first optimized to match the flat-channel experimental data for a reference case ( $V_{in} = 2$  m/s,  $Q = 1$  MW/m<sup>2</sup>), and later  $C_s$  was tuned for  $V_{in} = 2$  m/s,  $Q = 2$  MW/m<sup>2</sup>. This left the remaining part of the available experimental database free to validate the choice using fully independent information.

Table 2 summarizes the values of the free parameters used in our FLUENT/BR modeling, together with the sensitivity to their variation. The latter is defined as

$$S = \frac{(\Delta e/e)}{(\Delta x/x)} \tag{7}$$

where  $e$  is the average error produced by the model with respect to the temperature measured by the thermocouples and  $x$  the quantity against which the sensitivity is checked (either  $Pr_t$  or  $C_s$ ). The high sensitivity to  $Pr_t$  is characteristic of turbulent flows at large  $Re$ , while the strong effect of  $C_s$  is due to its third power influence on  $q_{FDB}$  in (5).

4. Results and discussion

4.1. Flat channel

We analyze a subset of the experimental runs [10], see Table 3.

Figs. 5–7 compare the temperatures computed at the thermocouples location with the measured values. Far from CHF, the average error (over all thermocouples) of the Rohsenow model for the case  $V_{in} = 1$  m/s is 4–5 °C (~5% of the bulk fluid subcooling), and 3–4 °C (~4%) at higher  $Q$ ; for the BR model it is 5–8 °C (~8%) far from CHF and 11–12 °C (~14%) approaching CHF (~4 MW/m<sup>2</sup>). For higher  $V_{in}$  the error shows a similar behavior, with the two models having comparable accuracy for low-to-moderate heat flux and the Rohsenow approach performing better near CHF.

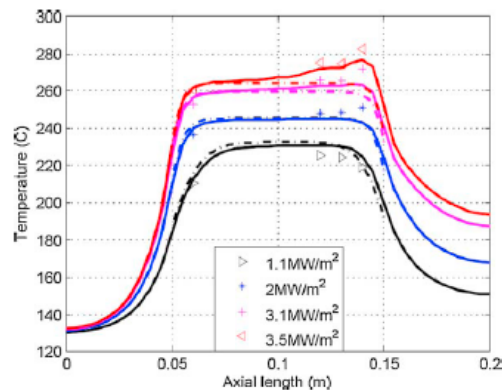


**Fig. 5.** Flat channel. Comparison of temperatures computed with the Rohsenow (solid line) and the BR (dash-dot line) models, with the thermocouple data (symbols) for  $V_{in} = 1$  m/s and at different  $Q$  levels.

**Table 3**  
Experimental test matrix for the flat-channel geometry.

$V_m$ (m/s)	1	2	4
$Q$ (MW/m <sup>2</sup> )	1, 1.2, 3.1, 3.5 and 4 (CHF)	1, 2, 3, 4, 4.5 and 5 (CHF)	1, 2, 3, 4, 5, 6, 6.5 and 7 (CHF)

Underlined: simulations performed.

The error values found with the BR model are of the same order of those reported in [5], where the BR model was adopted in conjunction with the SC\TETRA code. The better behavior of the Rohsenow model approaching CHF reflects the inclusion of more detailed physics (two-phase flow), but also the larger number of free parameters which can be used to tune the model against the experimental database.

Figs. 5–7 also show that the Rohsenow model reproduces the shape of the peak in the temperature profiles at the end of the heated region for high heat fluxes (except for  $V_{in} = 4$  m/s, suggesting that the code overestimates the drag force applied to the vapor bubbles at large flow velocities), while the BR does not. In fact, at higher heat fluxes vapor accumulates near the end of the heated region, producing a localized thermal resistance which cannot be seen by the (single phase) BR model.

Fig. 8 shows that the average vapor volume fraction (over the upper fluid–solid interface), computed using the Rohsenow model, is extremely sensitive to  $V_{in}$ , for any given  $Q$ .

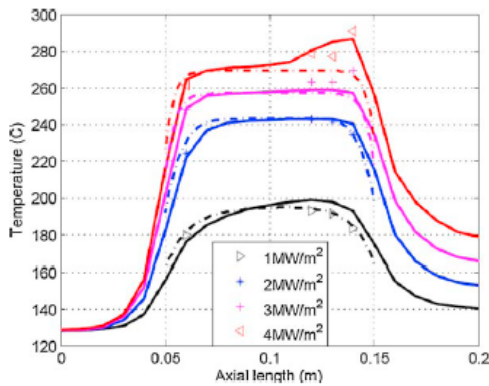


**Fig. 6.** Flat channel. Comparison of temperatures computed with the Rohsenow model, the BR model, and the experimental data for  $V_{in} = 2$  m/s.

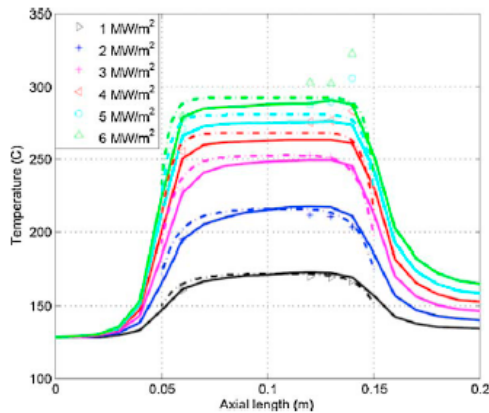


**Fig. 7.** Flat channel. Comparison of temperatures computed with the Rohsenow model, the BR model, and the experimental data for  $V_{in} = 4$  m/s.

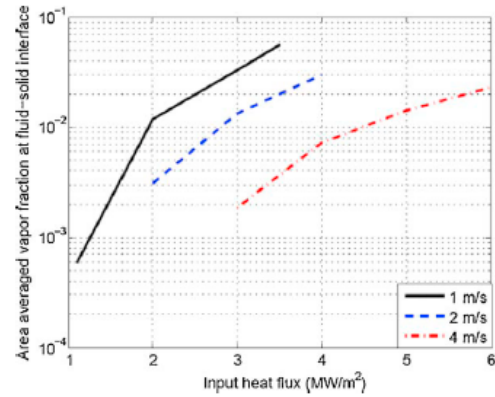


**Fig. 8.** Flat channel. Vapor volume fraction, averaged over the fluid–solid interface on the heated side of the flat-channel, as a function of the input heat flux.  $V_{in} = 1, 2,$  and  $4$  m/s are considered.

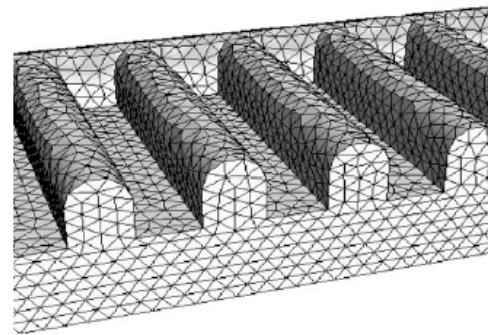


**Fig. 9.** Detail of the surface grid used for the hypervapotron geometry. A few teeth and the side-channel behind them are visible.

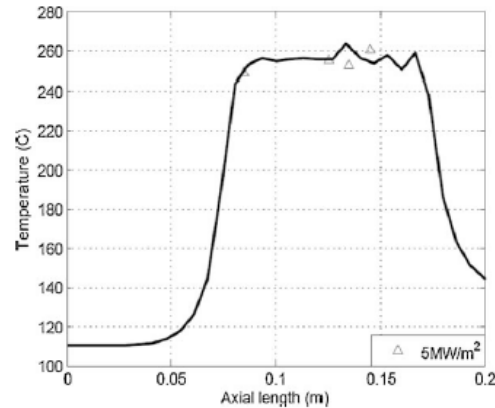


**Fig. 10.** Hypervapotron. Comparison of temperature profile computed by Rohsenow model with experimental data for  $Q = 5$  MW/m<sup>2</sup>,  $V_{in} = 2$  m/s.

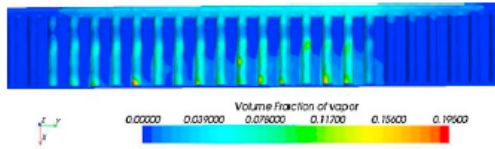


Fig. 11. Computed vapor volume fraction at the teeth top surface.  $Q=5\text{ MW/m}^2$ ,  $V_{in}=2\text{ m/s}$ .

#### 4.2. Hypervapotron

Fig. 9 shows a detail of the fluid region including a few teeth and the side channel, together with the computational (tetrahedral) mesh used for the hypervapotron. Detailed mesh-independence analysis using also other grid topologies (e.g. polyhedral) is ongoing.

Fig. 10 shows the comparison of the temperature computed by the Rohsenow model with the experimental data for the only case we tested so far, namely  $V_{in}=2\text{ m/s}$  and  $Q=5\text{ MW/m}^2$  (the measured CHF for this  $V_{in}$  was  $\sim 9\text{ MW/m}^2$ ). The average error is  $\sim 5^\circ\text{C}$  ( $\sim 5\%$  of the subcooling in the bulk fluid). Fig. 11 shows the vapor volume fraction at the fingers top-surface. The accumulation of the vapor in the portion of the teeth cavities further away from the side channel is clearly visible.

#### 5. Conclusions and perspective

We analyzed the heat transfer in highly subcooled conditions relevant for the ITER FW, in a flat-channel mock-up, comparing the Rohsenow and the BR models.

The Rohsenow model (implemented in the STAR-CCM+ code, with VOF transition for large vapor fractions) shows good agreement with the measured temperatures at all the tested input power/inlet velocity combinations, with an average error of at most  $7^\circ\text{C}$  ( $\sim 8\%$  of the subcooling of the bulk fluid). The BR model behaves comparably at low-to-moderate heat fluxes, but its performance worsens approaching the CHF, due to lack of proper representation of vapor phase; the maximum average error increases to  $12^\circ\text{C}$  ( $\sim 14\%$  of the subcooling).

This suggests that, notwithstanding its less detailed physics, the BR model may be a good engineering choice for first approximation analysis. In cases where more accurate information on the thermal behavior is required, or if the details of the flow field are considered a valuable output of the analysis, the Rohsenow model with transitions to VOF for film boiling should be preferred, provided

a suitable experimental database is available to tune its relatively larger number of free parameters.

While the preliminary results presented here for the hypervapotron geometry suggest that the Rohsenow model can capture also in that case, as for the flat channel, the main features of the fluid flow and heat transfer phenomena, the analysis of a more extended experimental database, which is already available, will be required in the future to confirm this trend.

#### Acknowledgments

We thank Dr. M. Merola for reading a first draft of the paper and providing helpful suggestions, Dr. D.L. Youchison for several discussions and for kindly providing preprints of his papers, Dr. E. Baglietto for advice on the STAR-CCM+ boiling model and Dr. D. Marchisio for providing access to the computational facilities used for the present study.

#### References

- [1] M. Merola, et al., ITER plasma-facing components, *Fusion Engineering and Design* 10–12 (2010) 2312–2322.
- [2] A. Loarte, et al., Transient heat loads in current fusion experiments, extrapolation to ITER and consequences for its operation, *Physica Scripta T128* (2007) 222–228.
- [3] Y. Bournonville, et al., Numerical simulation of swirl-tube cooling concept, application to the ITER project, *Fusion Engineering and Design* 2–6 (2009) 501–504.
- [4] S. Pascal-Ribot, et al., 3D numerical simulations of hypervapotron cooling concept, *Fusion Engineering and Design* 15–24 (2007) 1781–1785.
- [5] A. Ying, et al., A subcooled boiling heat transfer predictive model for ITER EHF FW designs, *Fusion Engineering and Design* 6–8 (2011) 667–670.
- [6] D.L. Youchison, et al., A comparison of two-phase computational fluid dynamics codes applied to the ITER first wall hypervapotron, *IEEE Transactions on Plasma Science* 387 (2010) 1704–1708.
- [7] D.L. Youchison, et al., Prediction of critical heat flux in water-cooled plasma facing components using Computational Fluid Dynamics, *Fusion Science and Technology* 60 (2011) 177–184.
- [8] W.M. Rohsenow, A method of correlation heat transfer data for surface boiling of liquid, *Transactions of ASME* 74 (1952) 969–976.
- [9] A.E. Bergles, W.M. Rohsenow, The determination of forced convection surface boiling heat transfer, *Journal of Heat Transfer* 86 (1964) 365–372.
- [10] I. Mazul, Russian development of enhanced heat flux technologies for ITER first wall, this conference.
- [11] D.C. Wilcox, *Turbulence Modeling for CFD*, DCW Industries Inc., California, 1993.
- [12] S.V. Patankar, *Numerical Heat Transfer and Fluid Flow*, Hemisphere, Washington, DC, 1980.
- [13] C.L.V. Jayatilaka, The influence of Prandtl number and surface roughness on the resistance of the laminar sublayer to momentum and heat transfer, *Progress in Heat and Mass Transfer* 1 (1969) 193–329.
- [14] STAR-CCM+ Version 6.02.008 User's Guide, CD-apdapco Inc., 2011.
- [15] ANSYS-FLUENT-13.0, User's Guide, ANSYS Inc., 2010.